Two-dimensional early transition metal carbides as supports for platinum catalysts

by

Zhe Li

A dissertation submitted to the graduate faculty

in partial fulfillment of the requirements for the degree of

DOCTOR OF PHILOSOPHY

Major: Chemical Engineering

Program of Study Committee:
Yue Wu, Major Professor
Wenyu Huang
Xinwei Wang
Matthew G. Panthani
Zengyi Shao

The student author, whose presentation of the scholarship herein was approved by the program of study committee, is solely responsible for the content of this dissertation. The Graduate College will ensure this dissertation is globally accessible and will not permit alterations after a degree is conferred.

Iowa State University

Ames, Iowa

2019

DEDICATION

To my parents, for their loving support and encouragement

TABLE OF CONTENTS

ACKNOWLEDGMENTS

First and foremost, I would like to deliver my sincerest appreciation to my advisor, Prof. Yue Wu, for his trust, support and encouragement. I am grateful to Yue who consistently convinced me that I can achieve much more than what I originally set out to become. His unwavering support opens new avenues for my career and life. Additionally, I would like to sincerely thank Prof. Wenyu Huang, Prof. Xinwei Wang, Prof. Matthew G. Panthani, and Prof. Zengyi Shao for their insightful comments and indispensable guidance during my Ph.D. study.

Next, I am indebted to numerous collaborators whose expertise and experience considerably contributed to several studies included in this dissertation. I thank Dr. Zhenwei Wu and Prof. Jeffrey T. Miller for their assistance in X-ray absorption spectroscopy, Dr. Yanran Cui; Dr. Yang Xiao, Prof. Fabio H. Ribeiro and Prof. Arvind Varma for their profound knowledge in kinetics tests. Prof. W. Nicholas Delgass deserves special thanks for his invaluable comments on my work. He defines what a good researcher is and serves as a model that I will follow if I can become a scientist. I would also like to thank Dr. Cory Milligan for his help in X-ray photoelectron spectroscopy; Dr. Lin Zhou and Dr. Tao Ma for their tutelage on microscopy; Dr. Zhiyuan Qi and Prof. Wenyu Huang for their guidance in electrochemical reactions; Prof. Liang Yu, Siwen Wang and Prof. Hongliang Xin for their help in density functional theory calculations.

I would also like to express my gratitude to my friends inside and outside of the lab who made my Ph.D. experience memorable. I thank Dr. Biao Xu, Dr. Enzheng Shi, and Dr. Fei Liu for their miscellaneous helps in my research. I feel lucky that I can reunite with my high school friends Zijian Zhao, Weijia Su and Jiayan Huo at Ames. Hsi-Hsin Lin, Liyang Sheng, Huan Qin, Xinyu Li, Dr. Zheyu Jiang, Dr. Russell Mahmood, Dr. Tianyu Wang, and Chengyang Wu have always been good friends and tolerated my occasional ‘‘nonsense’’, which I appreciate very much.

Finally, and most importantly, I reserve my deepest gratitude to my parents who throughout my life have provided me with family stability and unconditional support. Your selfless love has shaped me into the man that I am today.

爸爸妈妈，谢谢你们二十几年来对我的无私奉献，你们的爱我无以回报。

ABSTRACT

Tuning catalytic active sites through metal-support interactions (MSIs) has emerged as an effective strategy to design supported metal catalysts. The development and selection of supports are paramount for achieving the desired catalytic performance, which are however, great challenges. This dissertation involves elucidating the MSIs between platinum and two-dimensional early transition metal carbides (MXenes) and harnessing the MSIs for several industrial catalytic processes and electrocatalytic reactions.

This work discovered the reactive metal support interactions (RMSI) in MXenes supported Pt catalysts. RMSI refers to a chemical reaction between a metal and the support that induces the formation of bimetallic structures. By utilizing atomic resolution microscopy, *in situ* spectroscopy and density functional theory calculations (DFT), we confirmed the formation of intermetallic compounds (IMCs) nanoparticles in Pt/MXenes catalysts after reducing a Pt precursor with MXene supports at elevated temperatures. Moreover, we proposed that Pt undergoes a three-stage transformation from single atoms to IMCs on the surface of MXenes, which shed light on the mechanism of the RMSI. Last, we designed MXene supported Pt catalysts for a wide range of catalytic processes such as water-gas shit reaction, light alkane dehydrogenation and electrochemical hydrogen evolution reaction.

CHAPTER 1. GENERAL INTRODUCTION

1.1 Background

Two-dimensional (2D) materials are substances with high aspect ratio and thickness of a few layers of atoms. Hitherto, the most extensively studied 2D material is graphene,[1] and its rapid pace of development has stimulated tremendous research interest for other 2D materials. The family of 2D material is constantly expanding, other typical representatives include transition-metal dichalcogenides (TMDs),[2] hexagonal boron nitride (h-BN)[3] and phosphorene[4]. These 2D materials offer various compositions with unusual electronic, chemical and optical properties, which make them promising stages for a wide range of applications.[5]

The use of 2D materials in catalysis has grown in importance over the past decade. They have been used as supports for accommodating active sites or as metal-free catalysts.[6] For instance, graphene is well known for its unprecedented properties such as high specific area (> 2600 m^2g^{-1}), tunable electronic structure and high thermal stability,[7] which allow the rational design of graphene-based materials for a broad spectrum of catalytic reactions from hydrogenations[8] to carbon dioxide electrochemical reduction.[9] TMDs with optimized edge sites are efficient catalysts for hydrogen evolution reaction (HER), which emerge as replacements for costly platinum.[10] H-BN, an inorganic analogy of graphene, has recently shown high selectivity (>90%) to olefin in oxidative dehydrogenation of propane, a reaction in renewed interest due to the global boom of shale gas.[11] In light of these intriguing catalytic applications, it is anticipated that 2D materials and their hybrids will play a crucial role in catalysis although the research is still at the infant stage.

In 2011, the family of 2D materials welcomed its new member, i.e., an emerging class of 2D transition metal carbides, nitrides and carbonitrides (MXenes).[12] MXenes have a general

formula of $M_{n+1}X_nT_x$, where M represents an early transition metal (such as Ti, Nb, V and so on), X is carbon and/or nitrogen, T stands for surface functional groups and n varies from 1 to 3, which determines the number of atomic layers in the unit cell.[13] MXenes have typical structures of M_2XT_x, $M_3X_2T_x$, and $M_4X_3T_x$ with n layers of X elements covered by n+1 layers of M. In addition, double-M MXenes that are in solid solution or ordered phases are also prepared by experiments.[14] In the solid solution phase (second row in scheme 1), two kinds of M metals are randomly distributed in the MXenes. For the ordered phases (third row in scheme 1), layers of one M metal are sandwiched by those of the second M metal. Since the discovery of the first MXene, i.e., $Ti_3C_2T_x$ by the pioneer work of Naguib et. al, over 20 kinds of MXenes have been successfully synthesized.[14] Initially, MXenes have been extensively studied for energy storage devices such as lithium-ion batteries and supercapacitors due to their layered structures and outstanding electrical conductivity.[13] In addition, the rich compositions and surface chemistry, tunable structures and thermal stability hint that MXenes can be promising candidates for catalytic applications (Table 1.1). In this introduction, the important advances about the exploitation of MXene in catalysis, including electrocatalysis, photocatalysis and traditional heterogeneous catalysis are summarized.

Table 1.1 Summary of MXene and MXene-related hybrids for catalysis

Catalytic reactions	Catalysts	Performance and activity origin
HER	$MoS_2/Ti_3C_2@C$[15]	Overpotential of 135 mV @ 10 mA cm^{-2} in acid solution. The 2D structure and surface terminations of Ti_3C_2 facilitate the coupling of few-layered Mo_2S nanoplates that provide edge active sites for HER.
	Mo_2CT_x[16]	Mo_2CT_x delivers 10 mA cm^{-2} at an overpotential of 283 mV in 0.5 M H_2SO_4. Mo_2CT_x in delaminated form shows improved HER activity, together with the theoretical calculations indicating that the basal planes are catalytically active.
Oxygen evolution reaction (OER)	Co-P/3D Ti_3C_2 MXene[17]	An overpotential of 298 mV @ 10 mA cm^{-2} with a Tafel slope of 51 mV dec^{-1} was acheived by the CoP/3D Ti_3C_2 MXene in alkaline electrolyte. CoP converts to high valence cobalt compounds as active sites.
	$Ni_{0.7}Fe_{0.3}PS_3@Ti_3C_2T_x$ [18]	an overpotential of 282 mV @ 10 mA cm^{-2} with a Tafel slope of 36.5 mV dec^{-1} in 1 M KOH was achieved. Fe cations lead to ionic metal center that improves the carrier concentration and electrical conductivity.
Oxygen reduction reaction (ORR)	iron phthalocyanine (FePc)/$Ti_3C_2T_x$[19]	Twofold and fivefold enhancement of ORR activity was achieved compared to FePc and Pt/C, respectively. FeN_4 moiety on MXene induces redistribution of the local electron density, altering O_2 adsorption and reduction.
	$Ti_3C_2T_x$-$Ag_{0.9}Ti_{0.1}$ Nanowires[20]	MXene/NW-$Ag_{0.9}Ti_{0.1}$ shows the best ORR activity with an initial E_P of 0.564 V versus RHE. The bimetallic nanowires offer more sites for adsorbed oxygen and boost the conductivity in ORR reaction.
N_2 Fixation	$Ti_3C_2T_x$[21]	A maximum faradic efficiency of 4.62% and a NH_3 yield rate of 4.72 $\mu g h^{-1} cm^{-2}$ was achieved on $Ti_3C_2T_x$/SSM . The middle Ti at the edge sites are considered as the active sites for nitrogen reduction reaction (NRR).

Table 1.1 Continued

Catalytic reactions	Catalysts	Performance and activity origin
Photocatalysts for CO_2 reduction	TiO_2/Ti_3C_2[22]	0.22μmol h^{-1} for CH_4 production, 3.7 times higher than that of TiO_2. Ti_3C_2 MXene suppresses the electron-hole recombination and the rice curst-like morphology increases the density of active sites.
	Ti_3C_2/Bi_2WO_6[23]	CO_2 conversion of the 2 wt% Ti_3C_2/Bi_2WO_6 nanosheets is 4 times higher than that of the pristine Bi_2WO_6. The 2D/2D heterojunction increases the specific area and facilitates the charge separation.
Photocatalytic H_2 production	$CdS/Ti_3C_2T_x$ (nanoparticles)[24]	14342 μmol h^{-1} g^{-1} of H_2 with an apparent quantum efficiency of 40.1% at 420 nm. -F groups on the surface of $Ti_3C_2T_x$ are replaced with -O/-OH terminations which account for the rapid H_2 evolution.
	$Cu/TiO_2@Ti_3C_2T_x$[25]	A hydrogen production of 860 μmol h^{-1} g^{-1} are achieved. MXene traps the photoinduced holes of TiO_2 to accumulate the photoinduced electrons at the TiO_2/Cu_2O interfaces, leading to electron tunneling that reduces Cu_2O into Cu for enhanced catalytic activity.
Ethylbenzene dehydrogenation	$Ti_3C_2T_x$[26]	Enhanced rates for ethylbenzene dehydrogenation compared to graphene and nanodimonds. C−Ti−O is proposed to be the active sites.
Water-gas shift	Pt/Nb_2CT_x[27]	0.016 mol H_2 $(molPt)^{-1}$ s^{-1} at 300 °C. Pt-Nb surface alloy was formed due to the highly reducible surface of Nb_2CT_x.
Light alkane dehydrogenation	$Pt/Ti_3C_2T_x$ and Pt/Nb_2CT_x[28]	$Pt/Ti_3C_2T_x$ and Pt/Nb_2CT_x showed >90% olefin selectivity in propane and butane dehydrogenation. Complete Pt_3Ti and surface Pt_3Nb intermetallic compounds are formed due to reactive metal-support interaction (RMSI). which modify the electronic structures of the active sites.

1.2 MXene-Based Catalysts for Electrocatalysis

1.2.1 Hydrogen Evolution Reaction (HER)

Renewable energy has garnered tremendous attention due to the heighten demand for energy and the increasing consumption of non-renewable fossil energy. H_2, a zero-emission fuel with high gravimetric energy density, has been considered as one of the most promising alternatives for fossil energy. Electrocatalysis of water stands for a renewable and clean method for producing H_2. Recent progress has demonstrated both theoretically and experimentally that MXene-based catalysts have a bright future in HER. Gao et. al. investigated MXenes as catalysts for HER by calculating the Gibbs free energy (ΔG_{H*}) of H_2 adsorption under different coverages.[29] The ΔG_{H*} was -0.04 eV for Ti_2CO_2 with a hydrogen coverage of 1/8, indicating high activity for HER. Similarly, low H coverages (1/8 and 2/8) also benefited the HER catalytic activity for Nb_2CO_2 and $Nb_4C_3O_2$. On the contrary, $Ti_3C_2O_2$ showed the best HER activity when the H coverage was 4/8, as indicated by the nearly perfect ΔG_{H*} (~ 0 eV). These calculations implied that the surface terminated oxygens on the MXenes were the active sites for HER and that MXenes could be developed as efficient noble metal-free catalysts by modifying their surface chemistry.

Seh et. al. conducted experimental study of pristine MXenes as catalysts for HER.[16] Mo_2CT_x MXene catalyst required a 283 mV overpotential to reach a current density of 10 mA cm^{-2}. Although the Mo_2CT_x catalyst exhibited higher activity than Ti_2CT_x, its performance was not entirely satisfactory, especially when working as the replacement for noble metal catalysts such as Pt/C. Unlike the widely studied Mo_2S where only the edge sites are active, it was proposed that the basal plane of Mo_2CT_x served as the active sites toward HER. It should be noted that the surface of MXene is thermodynamically metastable and is prone to oxidation at ambient temperature, resulting in irreversible loss of electronic properties and surface activity. Therefore, MXene-based nanohybrids are designed to stabilize the basal planes of MXene and improve the performance of

HER. Wu et. al. reported that Ti_3C_2 MXene was coupled with Mo_2S and stabilized by carbon nanoplating.[15] Glucose molecules was adsorbed on the surface of Ti_3C_2 MXene with a subsequent hydrothermal treatment for carbonization. The MoS_2/Ti_3C_2@C catalyst showed an overpotential of 135 mV (@10 mA cm^{-2}) with a Tafel slope of 45 mV $decade^{-1}$, which was superior to MoS_2/rGO@C and MoS_2/oxidized MXene. Furthermore, 3D architecture of $Ti_3C_2T_x$ MXene could be achieved by a capillary-forced assembling strategy as described in.[17] The 3D structure significantly increased the specific area of $Ti_3C_2T_x$ MXene to 165.3 m^2 g^{-1}. By synergistically coupling the 3D MXene with CoP, the CoP@3D Ti_3C_2 catalysts achieved an overpotential of 168 mV at 10 mA cm^{-2} in alkaline electrolyte, which was comparable to that of Pt/C. Owing to the tunable structures that allow smooth charge transfer, the MXene materials have been developed as platforms for hybridization with active phases, which may pave a new avenue for the rational design of cost-effective alternatives to Pt-based catalysts toward HER.

1.2.2 Oxygen Evolution and Reduction Reactions (OER and ORR)

Clean energy systems such as electrochemical water splitting, rechargeable metal-air batteries and fuel cells are becoming of great significance due to the emission and climate change caused by excessive burning of fossil fuels. OER and ORR are essential to renewable-energy technologies, but suffer from intrinsic sluggish kinetics.[30] A variety of MXene-based catalysts have been studied for boosting OER/ORR. Ma et.al. reported a freestanding flexible film prepared by overlapping g-C_3N_4 and Ti_3C_2 MXene nanosheets as efficient catalysts for OER reaction in alkaline solution.[31] The film displayed an $E_{j=10}$ value of 1.65 V with a Tafel slop of 74.6 mV $decade^{-1}$, which outperformed IrO_2/C and RuO_2. It was proposed that interfacial Ti-N_x were the active sites for OER, and the hydrophilic characteristics of the MXene as well as the hierarchical pores in the thin film facilitated the charge transfer. Additionally, a 2D metal organic frameworks

(MOF), i.e., cobalt 1,4-benzenedicarboxylate (CoBDC) was hybridized with $Ti_3C_2T_x$ via an interdiffusion reaction for catalyzing OER.[32] The metallic $Ti_3C_2T_x$ promoted the charge transfer kinetics of the MXene-MOF coupling catalysts, and the specific area reached 199.1 m^2 g^{-1} resulting from porous structures created by the interdiffusion reaction. As a result, the $Ti_3C_2T_x$-CoBDC catalysts exhibited an onset potential of 1.51 V versus RHE. The catalyst delivered a potential of 1.64 V versus RHE at a current density of 10 mA cm^{-2} in 0.1 M KOH, which was better than the benchmark IrO_2 catalysts. Guo and co-workers reported a Ti_3CT_x MXene supported iron phthalocyanine (FePc) catalyst for enhanced activity of ORR.[19] With the addition of $Ti_3C_2T_x$, the half-wave potential ($E_{1/2}$) shifted to ~0.88V. It was hypothesized that the surface terminations of Ti_3CT_x MXene interacted with FeN_4 moiety, leading to Fe 3d electron delocalization and spin state transition of Fe (II) ions that benefited the adsorption and reduction of oxygen species. The turn over frequency (TOF) of FePc/Ti_3CT_x catalyst at 0.8V versus RHE was normalized to be 15.1 e s^{-1} $site^{-1}$, which was fourfold higher than that of the unsupported FePc. The above works demonstrate the emerging role of MXenes as supports/substrates in hybridizing with other nanomaterials for promoted electrochemical activity. So far, the development and application of MXene-based electrocatalysts toward superior OER and ORR activity is still in an infant stage as only $Ti_3C_2T_x$ is extensively studied. The attractive properties of $Ti_3C_2T_x$ are not unique in the family of MXene, and we envision that the extended research of other MXenes such as Nb_2CT_x and V_2CT_x will enrich the MXene-based catalysts as a new group of affordable and efficient catalysts for OER and ORR.

1.2.3 Nitrogen Reduction Reaction (NRR)

Ammonium (NH_3), one of the most highly demanded feed stocks in the world, is broadly used in chemical industry such as fertilizer and pharmaceutical productions.[33] Currently, Haber-Bosch process is the major strategy for producing industrial NH_3 from N_2 and H_2 using iron-based

catalysts under harsh conditions (350-550 °C and 150-350 atm). In fact, Haber-Bosch process annually consumes 1-2% of the global energy supply, and the process also generates > 1% of the globe CO_2 emission.[34] Alternatively, electrochemical N_2 conversion stands for a eco-friendly approach for producing NH_3 under mild condition. However, the development of NRR is significantly impeded by the lack of efficient electrocatalysts. Efforts are being made to overcome the extremely sluggish kinetics and low selectivity of NRR.

Recently, density functional theory (DFT) predicted that MXenes could be promising catalysts for NH_3 electrosynthesis.[35] V_3C_2 and Nb_3C_2 were found as the two most outstanding candidates in the family of MXenes with the reaction energies of 0.32 and 0.39 eV (vs standard hydrogen electrode), respectively. Kinetically, V_3C_2 required lower activation energy barriers (0.64 eV) for the first step of hydrogenation of N_2 (from N_2 to N-NH*) compared to that of Nb_3C_2 (0.85 eV), and its reaction profile was smooth with lower energy barriers for other hydrogenation steps. The NRR activity of MXene materials was not justified experimentally until Luo et. al. reported the direct application of vertically aligned Ti_3C_2 MXene nanosheets for electrocatalytic N_2 fixation.[21] DFT calculation suggested that the middle Ti atoms exhibited the highest adsorption of N_2 (-1.34 eV) compared to other sites such as O, C, and lateral Ti. A maximum faradic efficiency of 4.62% (-0.1 V versus RHE) with a NH_3 yield rate of 4.72 μg $h^{-1}cm^{-2}$ was achieved by Ti_3C_2 supported by stainless steel mesh (SSM). By preparing Ti_3C_2 MXene nanosheets with different sizes and changing the host (FeOOH nanosheet) for vertical alignment, the faradic efficiency of Mxene/FeOOH reached 5.78%, which was 1.25 times higher than that of the MXene/SSM. It was proposed that the middle Ti atoms on the edge sites and the sluggish nature of the host material (FeOOH) toward HER were responsible for the enhancement. Although challenges such as high energy barrier for the cleavage of N≡N bond still remain unsolved, the

pioneer work opens a new pathway for converting atmospheric N_2 to NH_3 under ambient conditions using pristine MXene. It is envisioned that MXene-based nanocomposites may function as feasible catalysts for NRR, and both experimental and theoretical studies of this direction may be spurred in the near future.

1.2.4 CO_2 Electroreduction Reaction (CRR)

The anthropogenic CO_2 emission caused by the excessive depletion of fossil fuels has disrupted nature's carbon balance, leading to environmental issues such as global warming, rising of sea level and extinction of species. These issues are intricate without a single solution, yet the recent advances in CO_2 conversion and utilization enable us to see the light at the end of the tunnel.[36] For an example, CRR represents a controllable and eco-friendly approach for converting CO_2 into value-added chemicals and fuels. 2D nanomaterials are considered encouraging candidates for electrocatalysis owing to their tunable surface structures, unique electronic states and programmable mechanical properties.[37] As an emerging member in the family of 2D materials, MXenes have been studied for CRR by computer-aided screening.[38] The low-coordinated metals on the surface of MXenes (three-coordinated terminal metals) were considered to be the active sites toward CO_2 chemisorption. Cr_3C_2 and M_3C_2 were the two best candidates for converting CO_2 to CH_4 among the group IV, V, and VI MXenes with a formula of M_3C_2. In the limiting step, i.e., the first hydrogenation step, the formation of chemisorbed OCHO• and HOCO• radical species exhibited spontaneous thermodynamics. With the addition of surface terminations such as -O and -OH, the energy input for CRR over $Cr_3C_2T_x$ and $M_3C_2T_x$ could be further reduced compared to the bare MXenes, indicating the favorable conversion of CO_2 to CH_4 on functionalized MXenes. However, it is noteworthy that the CRR over MXene-based catalysts is still at a nascent stage compared to other 2D nanomaterials. Experimental studies are indispensable to understand the nature of active sites on the surface of MXenes as well as the catalytic mechanism.

Despite the unknown challenges, some pioneer experimental efforts in photocatalytic CO_2 conversion have been made, we summarize them in subdivision 2.2.

1.3 MXene-Based Catalysts for Photocatalysis

Photocatalysis, an advanced catalysis technology that has been widely studied for environmental cleaning[39] and chemical synthesis,[40] has play crucial roles in addressing the global energy and environmental challenges in a sustainable manner. Over the past decade, significant progress has been achieved in the development of 2D materials such as graphene and TMDs as efficient catalysts for photocatalytic H_2 production,[39] water splitting,[41] and CO_2 reduction.[42] Since the advent of MXenes in 2011, they have been predicted as promising co-catalysts for photocatalysis because: (i) The surface of the MXenes are terminated by functional groups (-OH, -O and -F) that enable their intimate coupling with other semiconductors for heterostructures. (ii) MXenes possess conductive metal cores, assuring the excellent metallic conductivity and charge carrier transfer. (iii) the band-gap structures of MXenes can be modulated by tuning the surface chemistry.[43] Due to the above outstanding properties, MXenes have been extensively explored for photocatalytic processes, as summarized below.

1.3.1 Photocatalytic H_2 Production

Qiao et. al developed CdS/Ti_3C_2 composites for photocatalytic production of H_2.[24] DFT suggested that the $Ti_3C_2T_x$ terminated by -O groups showed a ΔG_{H^*} close to zero (-0.00238 eV), indicating the remarkable HER activity of $Ti_3C_2T_x$ after the modification of its surface chemistry. CdS was selected to hybridize with the MXene as its conduct band (CB) potential (-0.7 V) was much more negative than the E_f of the O-terminated $Ti_3C_2T_x$ (1.88 V). The surface -F groups of the pristine $Ti_3C_2T_x$ were replaced by -O/-OH after hybridizing with CdS using the hydrothermal treatments. Due to the separation of photoinduced electron-hole pairs, the CdS/Ti_3C_2 catalysts exhibited an outstanding photocatalytic H_2 production activity of 14342 μmol $h^{-1}g^{-1}$ with high

quantum efficiency of 40.1%. MXenes were also applied as co-catalysts for improving the photocatalytic activity of TiO_2 for hydrogen production.[44] 5% of $Ti_3C_2T_x/TiO_2$ delivered a fourfold enhancement in photocatalytic HER compared to pure TiO_2. Further improvement was also achieved by coupling Nb_2CT_x MXene with the TiO_2. The superior activity in MXene/TiO_2 was unraveled by Schottky barrier formed by the accumulation of negative charges (photoinduced electrons from CB of TiO_2) in the MXenes. The 2D carbides served as electron sinks in the photocatalytic reaction, which provided a general path for the rational design of MXene-based nanocomposites toward photocatalysis.

1.3.2 Photocatalytic CO_2 Reduction

Another important application of MXene-based materials for photocatalysis is CO_2 reduction. Low et. al. prepared TiO_2/Ti_3C_2 hybrids by simply calcining the Ti_3C_2 MXene at different temperatures.[22] The *in situ* growth of TiO_2 created a unique rice-curst like structure that enlarged the specific area of the catalysts. The heterojunction also benefited the electron transfer such as the migration of photoinduced electrons from TiO_2 to the MXene. As a result, the coupled catalysts achieved a photocatalytic CH_4 production rate of 0.22 μmol h^{-1}, which was 3.7 times higher than that of commercial TiO_2. This work serves as an example that heterointerfaces can be generated by directly using MXenes as the precursor, which provides a new protocol for constructing composites of MXene for attaining satisfied quantum efficiency and carrier separation in photocatalysis.

Recently the same group also reported the preparation of ultrathin Ti_3C_2/Bi_2WO_6 nanosheets for CO_2 photocatalytic conversion.[23] The 2D/2D heterojunction was synthesized by *in situ* growth of Bi_2WO_6 on the surface of Ti_3C_2 via hydrothermal treatments. With an optimized Ti_3C_2 loading of 2%, the product yields of CH_4 and CH_3OH were 1.78 μmol h^{-1} g^{-1} and 0.44 μmol h^{-1} g^{-1}, respectively. The total conversion of CO_2 over the Ti_3C_2/Bi_2WO_6 catalysts was 4.6 times

higher than that of the pristine Bi_2WO_6. The higher photocatalytic activity could be attributed to the intimate contact between the Ti_3C_2 and Bi_2WO_6 ultrathin nanosheets, leading to the short charge transport distance and large interface contact area. In additional to the 2D/2D heterojunction, MXenes-based heterostructures with reduced dimensional were also developed for efficient CO_2 conversion. Zeng et. al. reported the 0D MXene quantum dots (QDs) derived from 2D Ti_3C_2 MXene and their coupling with 1D Cu_2O nanowires (NWs) for the 0D/1D heterostructures.[45] The Ti_3C_2 QDs/Cu_2O NWs/Cu delivered a CH_3OH yield of 153.38 ppm cm^{-2}, which was 2.15 times of that from Ti_3C_2 sheets/Cu_2O NWs/Cu and 8.25 times of that from Cu_2O NWs/Cu. As the CB of Cu_2O is more negative than the E_F of Ti_3C_2, the photoinduced electrons tended to transfer to the 0D MXene QDs for the reduction of CO_2. With the tunable dimensionality of the MXene materials, this research illuminates new possibilities for designing MXene-based nanocomposites with mixed low-dimensional heterostructures.

1.4 MXene-Based Catalysts for Conventional Heterogeneous Catalysis.

The advent of MXenes has triggered the enthusiasm in the state-of-the art research on designing the 2D carbides or their nanocomposites for (photo)electrocatalysis. However, the catalytic properties of MXenes are scarcely investigated in conventional heterogeneous catalysis. On account of the tunable surface chemistry, various compositions and thermal stability, intuition informs us that MXenes or MXenes-based materials demonstrate vast potential applications in thermal catalysis. For an example, Liu et. al. developed $Ti_3C_2T_x$ as catalyst for dehydrogenation of Ethylbenzene (EB).[26] The conversion rate of EB over $Ti_3C_2T_x$ MXene was 92 μmol m^{-2} h^{-1}, which was the highest compared to graphene, nanodiamond and TiC-derived carbon. Moreover, the catalyst was stable under the test conditions for 40 hours, achieving a maximum styrene selectivity of 97.5% at a conversion around 21%. It was proposed that C-Ti-O dominating the surface was the active sites, which activated the C-H in EB.

Another representative work was developing MXenes as supports for noble metal catalysts. Although metal-support interactions (MSIs) have been known to play substantial roles in the catalytic active sites, effect of MXenes as supports for metal nanoparticles (NPs) catalysts remained unclear. Our previous work reported reactive metal-support interaction (RMSI) in Nb_2CT_x MXene supported platinum catalysts.[27] RMSI refers to a chemical reaction occurs at the interface between the supported NPs and their supports, often leading to the formation of bimetallic structures. The water-gas shift (WGS) reaction was selected as a model reaction to understand effects of RMSI on adsorbates and metal-support interfaces. Kinetics revealed that the RMSI stabilized the NPs in the Pt/Nb_2CT_x catalysts and created alloy-MXene interfaces with higher H_2O activation ability compared to a non-reducible support or a bulk niobium carbide. Electron energy-loss spectroscopy (EELS) confirmed that a Pt-Nb alloy was formed owing to the reducible surface of the MXene evidenced by XPS results. The RMSI found in 2D carbide supported catalysts allows the facile design of bimetallic structures by simply reducing metal precursors with MXene supports. It is noteworthy that the applications of MXenes-based materials for conventional heterogeneous catalysis still await research attention, we envisage that the reported RMSIs will lay an early foundation for exploring the catalytic properties of MXene supported NPs catalysts.

1.5 Summary and Outlook

In this introduction, we have outlined the general applications of MXenes in the field of catalysts including electrocatalysis, photocatalysis and conventional heterogeneous catalysis. The intriguing properties of MXenes such as tunable morphology and band-gap structure, metallic conductivity, thermal stability and rich surface chemistry inspire the rational design of MXene-based catalysts. For instance, the surface metal sites and surface functional groups have been proposed to be the active sites of MXene catalysts. It is anticipated that manipulating the surface chemistry by reduction, oxidization and surface terminations replacement can be effective routes

for tuning the catalytic performance of MXenes. Another common strategy for designing MXene-based catalysts is constructing heterojunction nanocomposites for optimized bandgap structure and enhanced charge transfer. The two-dimensionality and unique surface terminations of MXenes enable the construction of 2D/2D heterojunctions or even low-dimensional heterostructures such as 0D/2D and 1D/2D heterojunctions for improved photocatalytic activity.

The recent discovery of RMSI in MXene supported catalysts provides a facile route for designing bimetallic NPs catalyst. Generally, oxide supports are regarded as candidates for RMSIs. However, due to the thermodynamic stability of oxide supports, high temperatures (>550 °C) are often required for inducing the bimetallic structures, leading to the particle agglomeration and difficulty in controlling the particle size. The reducible surface of MXene allows the RMSI to occur at moderate temperature, and the MXene supported catalysts serve as examples that RSMI can be extended to non-oxide supports. Although progress has been made in catalysis based on MXene materials, the current research is still at nascent stage. Identification of the catalytic nature and elucidating the catalytic mechanism in MXene-based catalysts are still challenging. Moreover, MXenes other than $Ti_3C_2T_x$ are yet to be extensively studied, which merit further in-depth studies. Understanding the nature of active sites by the collaboration between experimentalists and theorists will lay solid foundation for catalytic applications of MXenes. We believed that by taking the advanced characterizations such as *in situ* spectroscopies and microscopies in conjunction with theoretical simulations, it will not be long before establishing the general principles for the rational design of MXene-based catalysts.

1.6 References

[1] K. S. Novoselov, A. K. Geim, S. V. Morozov, D. Jiang, Y. Zhang, S. V. Dubonos, I. V. Grigorieva, A. A. Firsov, *Science* **2004**, *306*, 666.

[2] M. Chhowalla, H. S. Shin, G. Eda, L.-J. Li, K. P. Loh, H. Zhang, *Nat. Chem.* **2013**, *5*, 263.

[3] L. Song, L. Ci, H. Lu, P. B. Sorokin, C. Jin, J. Ni, A. G. Kvashnin, D. G. Kvashnin, J. Lou, B. I. Yakobson, P. M. Ajayan, *Nano Lett.* **2010**, *10*, 3209.

[4] H. Liu, A. T. Neal, Z. Zhu, Z. Luo, X. Xu, D. Tománek, P. D. Ye, *ACS Nano* **2014**, *8*, 4033.

[5] A. J. Mannix, B. Kiraly, M. C. Hersam, N. P. Guisinger, *Nat. Rev. Chem.* **2017**, *1*, 0014.

[6] D. Deng, K. Novoselov, Q. Fu, N. Zheng, Z. Tian, X. Bao, *Nat. Nanotech.* **2016**, *11*, 218.

[7] X. Huang, X. Qi, F. Boey, H. Zhang, *Chem. Soc. Rev.* **2012**, *41*, 666.

[8] H. Yan, H. Cheng, H. Yi, Y. Lin, T. Yao, C. Wang, J. Li, S. Wei, J. Lu, *J. Am. Chem. Soc.* **2015**, *137*, 10484.

[9] F. Lei, W. Liu, Y. Sun, J. Xu, K. Liu, L. Liang, T. Yao, B. Pan, S. Wei, Y. Xie, *Nat. Commun.* **2016**, *7*, 12697.

[10] C. Tan, H. Zhang, *Chem. Soc. Rev.* **2015**, *44*, 2713.

[11] J. T. Grant, C. A. Carrero, F. Goeltl, J. Venegas, P. Mueller, S. P. Burt, S. E. Specht, W. P. McDermott, A. Chieregato, I. Hermans, *Science* **2016**, *354*, 1570.

[12] M. Naguib, M. Kurtoglu, V. Presser, J. Lu, J. Niu, M. Heon, L. Hultman, Y. Gogotsi, M. W. Barsoum, *Adv. Mater.* **2011**, *23*, 4248.

[13] M. Naguib, V. N. Mochalin, M. W. Barsoum, Y. Gogotsi, *Adv. Mater.* **2014**, *26*, 992.

[14] B. Anasori, M. R. Lukatskaya, Y. Gogotsi, *Nat. Rev. Mater.* **2017**, *2*, 16098.

[15] X. Wu, Z. Wang, M. Yu, L. Xiu, J. Qiu, *Adv. Mater.* **2017**, *29*, 1607017.

[16] Z. W. Seh, K. D. Fredrickson, B. Anasori, J. Kibsgaard, A. L. Strickler, M. R. Lukatskaya, Y. Gogotsi, T. F. Jaramillo, A. Vojvodic, *ACS Energy Lett.* **2016**, *1*, 589.

[17] L. Xiu, Z. Wang, M. Yu, X. Wu, J. Qiu, *ACS Nano* **2018**, *12*, 8017.

[18] C. F. Du, K. N. Dinh, Q. Liang, Y. Zheng, Y. Luo, J. Zhang, Q. Yan, *Adv. Energy Mater.* **2018**, *8*, 1801127.

[19] Z. Li, Z. Zhuang, F. Lv, H. Zhu, L. Zhou, M. Luo, J. Zhu, Z. Lang, S. Feng, W. Chen, L. Mai, S. Guo, *Adv. Mater.* **2018**, *30*, 1803220.

[20] Z. Zhang, H. Li, G. Zou, C. Fernandez, B. Liu, Q. Zhang, J. Hu, Q. Peng, *ACS Sustain. Chem. & Eng.* **2016**, *4*, 6763.

[21] Y. Luo, G.-F. Chen, L. Ding, X. Chen, L.-X. Ding, H. Wang, *Joule*, DOI: 10.1016/j.joule.2018.09.011.

[22] J. Low, L. Zhang, T. Tong, B. Shen, J. Yu, *J. Catal.* **2018**, *361*, 255.

[23] S. Cao, B. Shen, T. Tong, J. Fu, J. Yu, *Adv. Funct. Mater.* **2018**, *28*, 1800136.

[24] J. Ran, G. Gao, F.-T. Li, T.-Y. Ma, A. Du, S.-Z. Qiao, *Nat. Commun.* **2017**, *8*, 13907.

[25] C. Peng, P. Wei, X. Li, Y. Liu, Y. Cao, H. Wang, H. Yu, F. Peng, L. Zhang, B. Zhang, *Nano Energy* **2018**, *53*, 97.

[26] J. Diao, M. Hu, Z. Lian, Z. Li, H. Zhang, F. Huang, B. Li, X. Wang, D. Su, H. Liu, *ACS Catal.* **2018**, *8*, 10051.

[27] Z. Li, Y. Cui, Z. Wu, C. Milligan, L. Zhou, G. Mitchell, B. Xu, E. Shi, J. T. Miller, F. H. Ribeiro, Y. Wu, *Nat. Catal.* **2018**, *1*, 349.

[28] Z. Li, L. Yu, C. Milligan, T. Ma, L. Zhou, Y. Cui, Z. Qi, N. Libretto, B. Xu, J. Luo, E. Shi, Z. Wu, H. Xin, W. N. Delgass, J. T. Miller, Y. Wu, *Nat. Commun.* **2018**, *9*, 5258.

[29] G. Gao, A. P. O'Mullane, A. Du, *ACS Catal.* **2016**, *7*, 494.

[30] F. Cheng, J. Chen, *Nat. Chem.* **2012**, *4*, 962.

[31] T. Y. Ma, J. L. Cao, M. Jaroniec, S. Z. Qiao, *Angew. Chem. Int. Ed.* **2016**, *55*, 1138.

[32] L. Zhao, B. Dong, S. Li, L. Zhou, L. Lai, Z. Wang, S. Zhao, M. Han, K. Gao, M. Lu, X. Xie, B. Chen, Z. Liu, X. Wang, H. Zhang, H. Li, J. Liu, H. Zhang, X. Huang, W. Huang, *ACS Nano* **2017**, *11*, 5800.

[33] J. W. Erisman, M. A. Sutton, J. Galloway, Z. Klimont, W. Winiwarter, *Nat. Geosci.* **2008**, *1*, 636.

[34] V. Smil, *Enriching the earth: Fritz Haber, Carl Bosch, and the transformation of world food production*, MIT press, Cambridge, MA, USA **2004**.

[35] L. M. Azofra, N. Li, D. R. MacFarlane, C. Sun, *Energy & Environ. Sci.* **2016**, *9*, 2545.

[36] J. Ran, M. Jaroniec, S. Z. Qiao, *Adv. Mater.* **2018**, *30*, 1704649.

[37] H. Jin, C. Guo, X. Liu, J. Liu, A. Vasileff, Y. Jiao, Y. Zheng, S.-Z. Qiao, *Chem. Rev.* **2018**, *118*, 6337.

[38] N. Li, X. Chen, W.-J. Ong, D. R. MacFarlane, X. Zhao, A. K. Cheetham, C. Sun, *ACS Nano* **2017**, *11*, 10825.

[39] X. Liu, J. Iocozzia, Y. Wang, X. Cui, Y. Chen, S. Zhao, Z. Li, Z. Lin, *Energy & Environ. Sci.* **2017**, *10*, 402.

[40] J. M. Narayanam, C. R. Stephenson, *Chem. Soc. Rev.* **2011**, *40*, 102.

[41] A. Kudo, Y. Miseki, *Chem. Soc. Rev.* **2009**, *38*, 253.

[42] J. Liu, C. Guo, A. Vasileff, S. Qiao, *Small Methods* **2017**, *1*, 1600006.

[43] M. Khazaei, M. Arai, T. Sasaki, C. Y. Chung, N. S. Venkataramanan, M. Estili, Y. Sakka, Y. Kawazoe, *Adv. Funct. Mater.* **2013**, *23*, 2185.

[44] H. Wang, R. Peng, Z. D. Hood, M. Naguib, S. P. Adhikari, Z. Wu, *ChemSusChem* **2016**, *9*, 1490.

[45] Z. Zeng, Y. Yan, J. Chen, P. Zan, Q. Tian, P. Chen, *Adv. Funct. Mater.*, DOI: 10.1002/adfm.201806500.

CHAPTER 2. REACTIVE-METAL SUPPORT INTERACTIONS AT MODERATE TEMPERATURE IN TWO-DIMENSIONAL NIOBIUM CARBIDE SUPPORTED PLATINUM CATALYSTS

Zhe Li[1], Yanran Cui[2], Zhenwei Wu[2], Cory Milligan[2], Lin Zhou[3], Garrett Mitchell[2], Biao Xu[1], Enzheng Shi[1], Jeffrey T. Miller[2], Fabio H. Ribeiro[2], Yue Wu[1]*

[1]Department of Chemical and Biological Engineering, Iowa State University, Ames, IA 50011, USA.

[2]Charles D. Davidson School of Chemical Engineering, Purdue University, West Lafayette, IN 47907, USA.

[3]Ames Laboratory, Department of Energy, Ames, IA 50011, USA.

Modified from a manuscript published in Nature Catalysis

2.1 Abstract

The reactive metal-support interaction (RMSI) offers electronic, geometric and compositional effects that can be used to tune catalytic active sites. Generally, supports other than oxides are disregarded as candidates for RMSI. Here, we report an example of non-oxide based RMSI between Pt and Nb_2CT_x MXene, a recently developed, two-dimensional (2D) metal carbide. The surface functional groups of the 2D carbide can be reduced, and a Pt-Nb surface alloy is formed at a moderate temperature (350 °C). Such an alloy exhibits weaker CO adsorption than monometallic Pt. Water-gas shift (WGS) reaction kinetics reveal that the RMSI stabilizes the nanoparticles and creates alloy-MXene interfaces with higher H_2O activation ability compared to a non-reducible support or a bulk niobium carbide. This RMSI between Pt and the niobium MXene support can be extended to other members of the MXene family and opens new avenues for the facile design and manipulation of functional bimetallic catalysts.

2.2 Introduction

Supported bimetallic nanoparticles represent a wide range of catalysts with tunable compositions and electronic properties[1,2]. Common strategies for preparing bimetallic catalysts include impregnation, reductive deposition precipitation, and atomic layer deposition[1,3]. Recently, a so-called reactive metal-support interaction (RMSI) has been shown to provide a facile route for preparing bimetallic alloys[4]. RMSI refers to a chemical reaction between a metal and the support that induces the formation of bimetallic structures that may not be easy to obtain by other synthetic methods. The reducibility of the support plays a crucial role in its RMSI activity. For instance, materials with RMSI involving reducible oxides, such as TiO_2 and CeO_2, can be prepared at lower temperatures than those involving hard-to-reduce oxides (such as SiO_2 and Al_2O_3)[5]. Hitherto, only oxide supports have been considered as candidates for RMSI, but high-temperature reductions (>550 °C) are often needed, which limits the compositional variety of catalysts available and may lead to particle agglomeration and difficulty in controlling the size of the nanoparticles[6,7]. More reactive or reducible supports, such as carbides, represent an alternative that could be involved in RMSI at a lower temperature and be prepared with well-dispersed active sites. Nonetheless, interactions between metals and supports other than oxides are not well understood even though they are key to establishing general rules for rational catalyst design via RMSI.

MXenes, a new family of two-dimensional (2D) metal carbides, nitrides or carbonitrides, are usually produced by selective extraction of the "A" layers from layered ternary transition metal carbides called MAX phases[8]. This synthetic procedure results in the surface termination groups of MXenes including -OH, -O and -F. Thus, MXenes have a general formula of $M_{n+1}X_nT_x$, where M represents an early transition metal, X is C or N, n varies from 1 to 3, and T stands for the surface functional groups[9]. To date, MXenes have been extensively developed as electrodes for batteries and supercapacitors due to their good electrical conductivities[10]. Recently, MXenes have

started to gain attention in photo/electrochemical applications due to their unique surface functional groups[11,12]. Functional groups on the surface of supports have been known to facilitate the adsorption of metal precursors by electrostatic interactions and thus serve as anchors for active sites[13-15]. Additionally, the surface functional groups, such as -OH and -F on Ti_2CT_x MXene can be removed by reactions with hydrogen at low temperature (227 °C)[16]. Removal of the terminal groups on the surface of the MXenes also exposes new terminal metal sites (for example, Nb, Ti and V) that are redox active[12]. For MXenes-supported catalysts, these sites can also form admetal-support interfaces that are catalytically active. Moreover, highly reducible and reactive surface make MXenes promising candidates for involvement in RMSI with metal nanoparticles. Considering the reducibility of the 2D carbides, RMSI may occur at lower temperatures (<550 °C) for MXene-supported catalysts.

Here, we report a Pt nanoparticle catalyst supported on Nb_2CT_x MXene exhibiting an RMSI after reduction in H_2 at moderate temperature (350 °C). Quasi *in situ* X-ray photoelectron spectroscopy (XPS) indicates that the surface of the Nb_2CT_x MXene is reducible based on the removal of the surface -O and -OH terminations and enrichment of Nb_2O_5 on the reduced MXene surface upon subsequent air exposure. Electron energy loss spectroscopy (EELS) and *in situ* X-ray absorption spectroscopy (XAS) show that a Pt-Nb surface alloy is formed as a result of the H_2 reduction. The water-gas shift (WGS) reaction was selected as a model reaction to understand effects of RMSI on adsorbates and metal-support interfaces. WGS kinetics at 300 °C suggests CO has a lower relative surface coverage on the Pt/Nb_2CT_x, and the alloy nanoparticles form active interfaces for H_2O activation with the reduced Nb_2CT_x MXene surface, which exhibits enhanced H_2O dissociation activity compared to Pt/Al_2O_3. In contrast to Pt/Nb_2CT_x, Pt supported by conventional bulk NbC was inert in the WGS reaction. The catalyst underwent significant particle

agglomeration, and no alloy formation was observed. This work demonstrates that RMSI can be achieved on supports other than oxides, and 2D Nb_2CT_x MXene allows the catalyst to become involved in RMSI at 350 °C while retaining control of the particle size.

2.3 Results and Discussion

2.3.1 Preparation and Characterizations of the Nb_2CT_x Support

The preparation of few-layer niobium MXene (Nb_2CT_x) via HF treatment is summarized in the Methods section. The X-ray diffraction (XRD) pattern of the prepared Nb_2CT_x support (Figure S2.1) shows that the (002) peak of the HF-treated Nb_2AlC powder shifts to 2θ of 9.3°, which corresponds to a c lattice parameter (c-LP) of 19 Å compared to the c-LP of 13.9 Å observed in the initial MAX (Nb_2AlC) phase. XAS was performed to confirm the structure of the niobium carbide MXene. The results of Nb K-edge X-ray absorption near edge structure (XANES) analysis are presented in Figure 2.1a and show that the shape of the XANES spectrum of Nb_2CT_x is similar to that of commercial NbC but different from those of Nb_2AlC and Nb_2O_5. The edge energy of the MXene (19000.7 eV) is close to that of NbC (19000.2 eV) but distinct from those of Nb_2AlC (18998.7 eV) and Nb_2O_5 (19003.3 eV), which confirms the removal of Al from the parent MAX phase. The edge energy of Nb_2CT_x is slightly higher than that of NbC, suggesting that the Nb_2CT_x is partially oxidized due to the terminal groups or Nb_2O_5 on its surface[17]. X-ray absorption fine structure (EXAFS) spectra (Figure 2.1b) were also used to confirm the 2D structure of the material since Nb_2CT_x shows first-shell (Nb-C) scattering similar to that of NbC but second-shell (Nb-C-Nb) scattering much lower than that of NbC due to the reduced dimensionality. Moreover, the typical lamellar structure of Nb_2AlC (Figure S2.2a) is converted to an accordion-like structure (Figure 2.1c), which confirms the exposure of individual grains along the basal planes. After mildly sonicating the Nb_2CT_x MXene multilayers in deaerated ethanol, few-layered electron transparent nanosheets could be obtained as shown in the TEM image (Figure 2.1d).

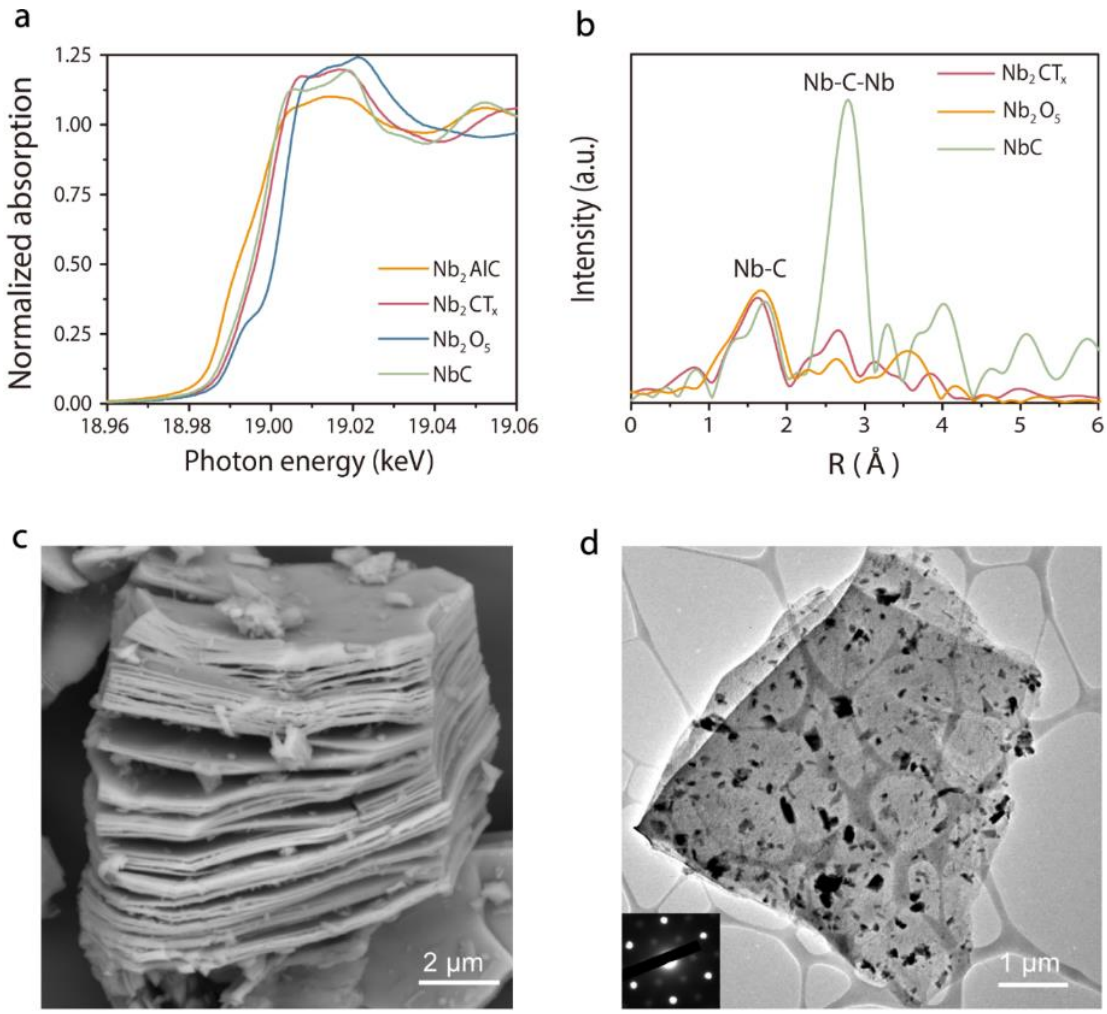

Figure 2.1 Characterization of Nb_2CT_x MXene support. (a) Nb K-edge XANES of Nb_2AlC, Nb_2CT_x MXene, NbC and Nb_2O_5. (b) Fourier transforms of the k^2 EXAFS of Nb_2CT_x compared to the references (NbC and Nb_2O_5). (c) SEM micrograph of Nb_2CT_x MXene (d) TEM image of Nb_2CT_x nanosheets. Inset represents the selected area electron diffraction (SAED) pattern showing hexagonal basal plane symmetry.

2.3.2 Kinetics of the WGS Reaction

Pt was loaded onto the Nb_2CT_x support via incipient-wetness impregnation (IWI) as reported in a previous work[18]. The Pt loading was estimated to be 1% by atomic absorption spectroscopy (AAS). The 1% Pt/Nb_2CT_x catalyst was then tested for activity in the WGS reaction under standard condition (see Methods section). As shown in Figure 2.2a, the catalyst is stable under the conditions used for the WGS reaction kinetic tests. The WGS reaction rate per mole of

Pt in 1% Pt/Nb_2CT_x measured at 300°C is 0.016 mol H_2 (mol Pt)$^{-1}$ s^{-1}, and the apparent activation energy is 70 ± 3 kJ mol^{-1} (Figure S2.3). The spent 1% Pt/Nb_2CT_x catalyst has an average particle size of approximately 2.6 ± 0.6 nm based on high-angle annular dark field scanning transmission electron microscopy (HAADF-STEM) (Figure 2.5a, Figure S2.4), which shows that the MXene support stabilizes small Pt nanoparticles. We selected the 1.5% Pt/Al_2O_3 catalyst (Table 2.1) from our previous work[19] as the reference catalyst because the particle size (estimated by Pt dispersion) is comparable to that of the 1% Pt/Nb_2CT_x catalyst. Moreover, Al_2O_3 is considered a non-reducible oxide at the moderate reduction temperature (350 °C) in contrast to the reducible Nb_2CT_x support. Although, according to CO chemisorption, 35% of the Pt was exposed on the surface of the 1.5% Pt/Al_2O_3 catalyst, we did not observe any measurable CO uptake at ambient temperature or at -30 °C for the fresh 1% Pt/Nb_2CT_x catalyst after it was reduced *in situ* at 350 °C (Supplementary Methods). The suppressed CO chemisorption is not due to particle agglomeration, and the average particle size of 1% Pt/Nb_2CT_x should correspond to an estimated dispersion of 38%. This large discrepancy can be attributed to surface alloy formation due to the reducible surface of the niobium MXene-supported catalyst, which will be discussed later. No measurable WGS conversion was observed for Pt supported by commercial NbC (bulk) under the same WGS test conditions. We found that the Pt particles had sintered significantly (average particle size ~13.8 ± 9.6 nm) in the Pt/NbC (bulk) catalyst (Figure S2.5). The agglomeration of nanoparticles substantially reduces the number of metal-support interface sites, which presumably leads to the observed loss in WGS activity.

The apparent reaction orders are shown in Figure 2.2b and Table 2.1. As the log derivative analysis of the Langmuir-Hinshelwood mechanism (Supplementary methods) shows, the apparent reaction order may be related to the relative surface coverage of the corresponding adsorbates. The

lower apparent reaction orders with respect to certain reactants imply higher relative coverage of the adsorbed species[18]. Compared to the Pt/Al_2O_3 catalyst, Pt/Nb_2CT_x shows a higher apparent reaction order with respect to CO, which suggests that CO adsorption is weaker on the MXene-supported catalyst. At the same time, Pt/Nb_2CT_x has a lower apparent reaction order with respect to H_2O, indicating that the MXene support has a stronger H_2O adsorption affinity than that of Al_2O_3. Previous studies have also reported that the support surface plays a significant role in the activation of H_2O during the WGS reaction, and the most active site of WGS is at the metal-support interface[20]. Here, Nb_2CT_x outperforms Al_2O_3 as a support for WGS catalysis due to its stronger interactions with H_2O or hydroxyl groups. The apparent reaction order for CO_2 is slightly negative and approaches zero for both catalysts, which can be attributed to the weak interaction between the surface of the Pt and CO_2. The apparent reaction order with respect to H_2 is -0.47 for Pt/Nb_2CT_x, which is indicative of H_2 inhibition of the forward WGS reaction. The inhibition indicates that H_2 competes with CO for the limited number of active sites.

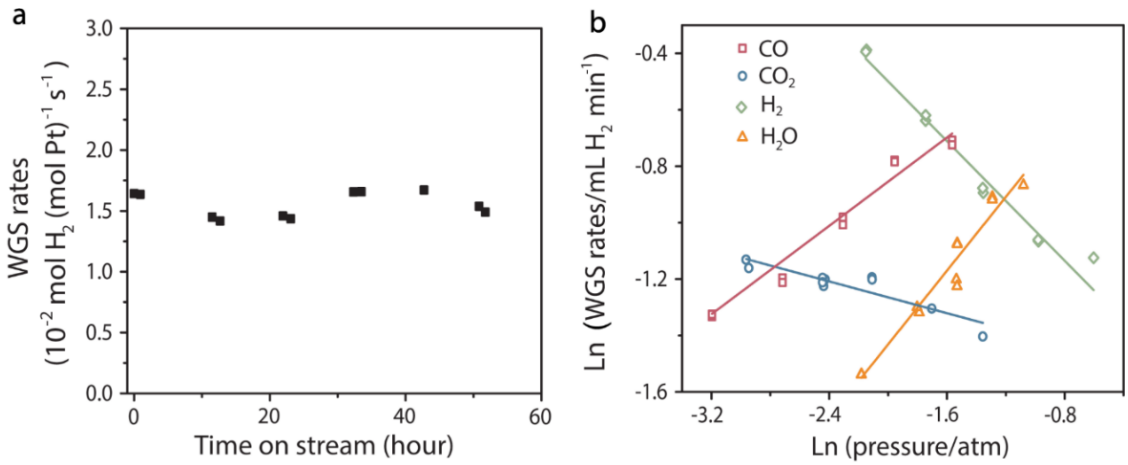

Figure 2.2 Kinetics of the WGS reaction over the 1% Pt/Nb_2CT_x MXene catalyst. (a) WGS rates normalized by amount of Pt in the 1% Pt/Nb_2CT_x catalyst. The rates were measured at 300 °C with a feed composition of 6.8% CO, 21.9% H_2O, 8.5% CO_2, and 37.4% H_2 balanced by Ar (standard conditions). (b) Apparent reaction orders for CO, CO_2, H_2, and H_2O for 1% Pt/Nb_2CT_x. Reaction orders were determined at standard conditions with each component varying in the range of 4–21% for CO, 5–25% for CO_2, 11–34% for H_2O, and 14–55% for H_2.

Table 2.1 WGS kinetics of Pt/Nb_2CT_x and Pt/Al_2O_3

Catalysts	WGS Rates per mole of Pt at 300°C / 10^{-2} mol H_2 (mol metal)$^{-1}$ s^{-1}	TOR at 300°C / 10^{-2} mol H_2 (mol surface metal)$^{-1}$ s^{-1}	Ea/ kJ(mol)$^{-1}$ (±3)	Reaction Orders (±0.03)				Percentage of exposed Pt (%)
				H_2O	CO_2	CO	H_2	
1% Pt/Nb_2CT_x MXene	1.6	-	71	0.65	0.09	0.39	-0.47	-
1.5% Pt/Al_2O_3[19]	1.4	4	96	0.9	-0.1	0.1	-0.5	35

2.3.3 Reducibility of the Pt/Nb_2CT_x Catalysts

To understand the change in the Nb_2CT_x MXene support after H_2 reduction, a series of quasi *in situ* XPS measurements were carried out (Supplementary methods). In the Nb 3d spectrum of a fresh Pt/Nb_2CT_x sample (top spectrum in Figure 2.3a), the three pairs of peaks at 204.1/206.8 eV, 205.5/208.3 eV and 207.4/210.1 eV were identified as the $3d_{5/2}/3d_{3/2}$ doublets of Nb-C, $NbC_xO_yF_z$ and Nb_2O_5, respectively[17]. The presence of surface terminations (-OH, -O and -F associated with the $NbC_xO_yF_z$ species) on the fresh Pt/Nb_2CT_x catalyst was also confirmed by high resolution spectra in the O 1s and F 1s regions (bottom spectra in Figures 2.3b, c). The fresh Pt/Nb_2CT_x catalyst was then reduced at 350 °C or 550 °C (designated as R350 °C and R550 °C, respectively), and the samples were submitted to XPS analysis under ultrahigh vacuum (UHV) conditions without exposure to air. Figure 2.3a shows the XPS spectra of the Nb 3d regions of the samples reduced at 350 °C and 550 °C and the sample reduced at 350 °C and then exposed to air. The negligible change in the peaks corresponding to Nb-C (204.1 eV) indicates that the structure of the Nb_2CT_x MXene was preserved after reduction at both 350 °C and 550 °C. However, after exposing the reduced sample to air, the intensity of the carbide peak decreases dramatically, and

the Nb(V) oxide peak becomes better resolved (Figure 2.3a), which implies the oxide species (Nb_2O_5) is enriched on the surface of the material and the surface Nb-C partly decomposes. Moreover, after reduction at 350 °C (Figures 2.3b, c), the peaks for the adsorbed O and the terminal OH/O groups that were present on the fresh Pt/Nb_2CT_x surface disappear, indicating that these surface OH/O terminations can be effectively removed. Following H_2 temperature-programmed reduction (TPR) of Nb_2CT_x MXene, a peak indicative of H_2O at 340 °C appears (Figure S2.6a), which is likely due to the removal of the O and OH functional groups. The atomic concentration of F terminations, as estimated by XPS analysis, decreased from 4% to 1.8% after reduction at 350 °C but were completely removed in the higher temperature reduction (550 °C) (Figure 2.3c). The higher temperature required to remove the F moieties indicates the F groups bind more strongly than the OH/O groups to the surface of the MXene. The results of the quasi *in situ* XPS analysis suggest that the surface of the catalyst is reduced under the moderate-temperature (350 °C). It is plausible that with the removal of surface functional groups from the MXene, the coordinatively unsaturated surface is prone to oxidation in air, which suggests the reduced surface is highly redox active.

Pt/Nb_2CT_x samples with different treatments (fresh, 350 °C reduced and post WGS) were also investigated by Nb K-edge XAS analysis (Figures 2.3d, e). In the spent Pt/Nb_2CT_x catalyst and the fresh Pt/Nb_2CT_x sample reduced by H_2 at 350 °C, the supports maintain the same carbide structure matrix as was present in the fresh Pt/Nb_2CT_x based on the minimal changes observed in the XANES spectra. The scattering intensity in the EXAFS decreased slightly, which likely corresponds to the decrease in the number of ligands on surface of the Nb_2CT_x. The spent catalyst still showed the typical accordion-like structure of MXene (Figure S2.2b) and the characteristic diffraction features of carbide (Figure S2.8), suggesting that the MXene support did not collapse

during the WGS reaction. Therefore, our results indicate that the main structure of Nb_2CT_x remains intact during the reduction and WGS reaction, but the surface of Nb_2CT_x can be reduced at the moderate temperature (350 °C). The reducibility of the Nb_2CT_x support suggests that it can be used to introduce significant metal-support interactions to the catalyst.

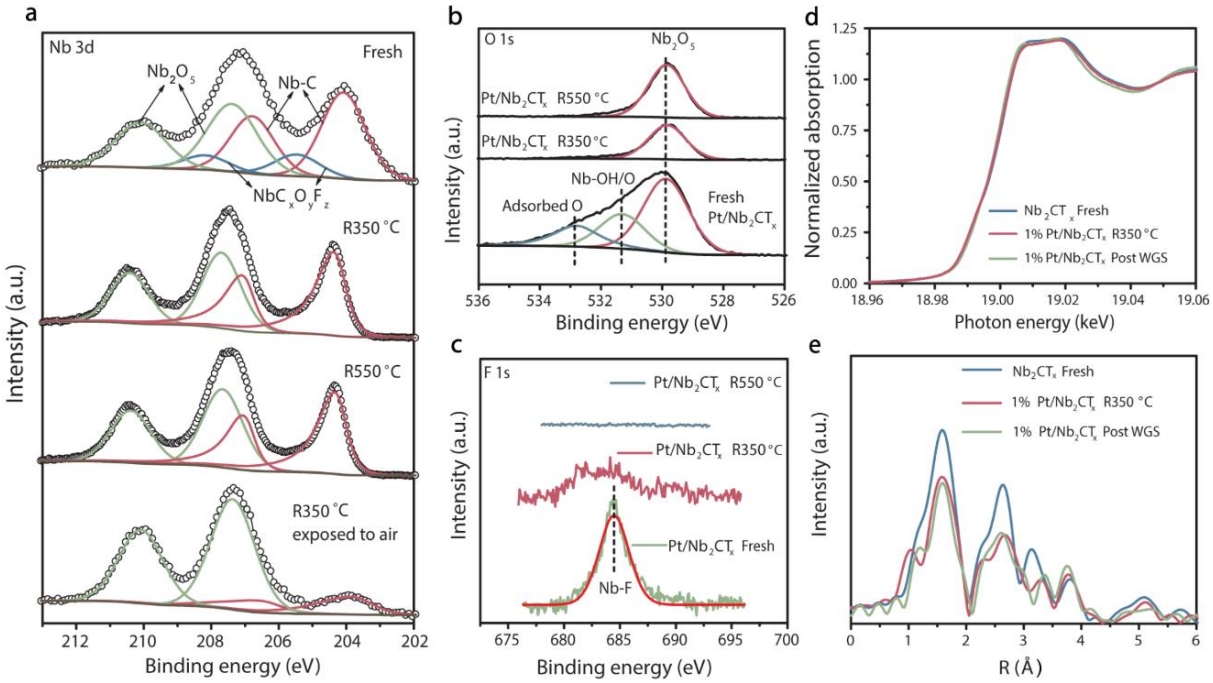

Figure 2.3 Nb 3d XPS measurements and Nb edge XAS of Pt/Nb_2CT_x catalysts. (a) The Nb 3*d* region of *ex situ* XPS of a fresh 1% Pt/Nb_2CT_x sample and quasi *in situ* XPS of 1% Pt/Nb_2CT_x reduced at 350 °C and 550 °C, and *ex situ* XPS of 1% Pt/Nb_2CT_x reduced at 350 °C and exposed to air before analysis. (b) Quasi *in situ* XPS of the O 1*s* region of 1% Pt/Nb_2CT_x reduced at 350 °C and 550 °C. (c) Quasi *in situ* XPS of the F 1*s* region of 1% Pt/Nb_2CT_x reduced at 350 °C and 550 °C. (d) XANES spectra of the Nb K-edge of fresh Nb_2CT_x scanned in air, and *in situ* XANES spectra of fresh 1% Pt/Nb_2CT_x treated with 3% H_2/He at 350 °C, and XANES spectra of post-WGS reaction 1% Pt/Nb_2CT_x catalyst scanned in air. (e) Fourier transform magnitude of the k^2 EXAFS of fresh Nb_2CT_x, reduced fresh 1% Pt/Nb_2CT_x and post-WGS reaction 1% Pt/Nb_2CT_x catalyst; all treatments were the same as those used to collect the XANES spectra.

2.3.4 Reactive Metal-Support Interaction (RMSI)

The interaction between the Pt and the Nb_2CT_x support and the corresponding changes in the nanoparticles were further investigated by *in situ* Pt L_{III} edge XAS as well as Pt region XPS. For the Pt L_{III} edge XANES (Figure 2.4a), the whiteline of the 1% Pt/Nb_2CT_x catalyst reduced at

350 °C is more intense and narrower in shape than that of 2% Pt/Al_2O_3, which indicates the presence of non-Pt neighbors surrounding the Pt atoms. The change in the nanoparticle structure is also reflected by the altered EXAFS (Figure 2.4b) of the Pt/Nb_2CT_x catalyst compared to that of monometallic Pt on Al_2O_3. The relative intensities of the peaks are different in the metal-metal distance region, suggesting that Pt-Nb interferes with Pt-Pt scattering, i.e., through the formation of a bimetallic structure. Our fitting results of Pt/Nb_2CT_x reduced at 350 °C (7.4 Pt-Pt bond at 2.75 Å and 0.9 Pt-Nb bond at 2.76 Å) imply that a Pt-rich bimetallic surface alloy is formed at this moderate temperature, which indicates that RMSI occurs between the Pt nanoparticles and the Nb_2CT_x support.

Quasi *in situ* XPS analysis was also conducted to investigate the potential electronic effect of the formation of the bimetallic surface alloy. We used Pt/SiO_2 as a reference instead of Pt/Al_2O_3 because the Al 2p region overlaps with the Pt 4f region, and SiO_2 is a non-reducible oxide similar to Al_2O_3. In previous works on Pt-M alloy systems (M = Sn, Co, Ru and Ti), the binding energies of Pt were reported to shift to higher values with respect to pure Pt[21-23]. In our XPS spectra (Figure 2.4c), the Pt $4f_{7/2}$ binding energy exhibited a positive shift (~0.5 eV) for Pt/Nb_2CT_x compared with Pt/SiO_2, which is consistent with the literature and is indicative of the formation of a Pt-Nb bimetallic structure. When the reduction temperature is increased to 550 °C, similar changes of a greater magnitude were observed in the XPS analysis as well as XAS and correspond to a higher degree alloy formation. We discuss this in more detail in Figure S2.9. Previous DFT studies suggested that the formation of alloys with transition metals modified the electronic structure of Pt atoms and lead to shifts in the d-band centers, which could weaken CO adsorption[22,24,25]. This electronic effect resulting from the formation of the Pt-Nb surface alloy explains the suppressed CO chemisorption as well as the altered relative coverage of CO on the Pt/Nb_2CT_x catalyst.

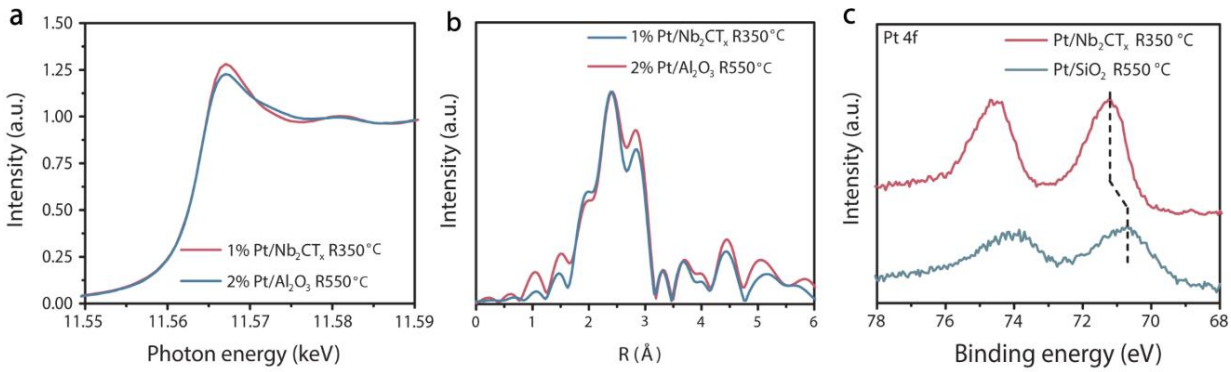

Figure 2.4 *In situ* XAS and quasi *in situ* XPS of the 1% Pt/Nb_2CT_x catalysts. (a) *in situ* XANES spectra of Pt L_{III} edge of the 2% Pt/Al_2O_3 sample treated at 550 °C and fresh 1% Pt/Nb_2CT_x treated at 350 °C in 3% H_2/He. (b) Fourier transform magnitude of the k^2 EXAFS of the 2% Pt/Al_2O_3 sample treated at 550 °C and fresh 1% Pt/Nb_2CT_x treated at 350 °C in 3% H_2/He. (c) Quasi *in situ* XPS spectra of Pt 4*f* of Pt/SiO_2 reduced at 550 °C and 1% Pt/Nb_2CT_x reduced at 350 °C.

Although the *in situ* XAS and energy-dispersive spectroscopy (EDS) results (Figure S2.10) suggest a uniform bulk alloy was not formed after reduction at the moderate temperature (350 °C), EELS in an aberration-corrected STEM was employed to provide a more-direct characterization of the near-surface region of the Pt-Nb nanoparticles. Figure 2.5a shows typical Nb_2CT_x MXene-supported nanoparticles with an average particle size of approximately 2.6 nm. The two-dimensionality of the MXene facilitates the STEM characterization of supported nanoparticles relative to conventional bulk carbide, so a twinned nanoparticle 3 nm in diameter can be atomically resolved (Figure 2.5b). Figures 2.5c and 2.5d show Z-contrast STEM images of typical Pt-Nb alloy nanoparticles approximately 3 nm in diameter. The particles are only partially attached to the Nb_2CT_x MXene to avoid signals from the support. Energy loss spectra were taken with the electron beam scattering through several different points around the surface edge of the particles. The spectra from the edge of the nanoparticles provided electronic information primarily on near-surface atoms and exhibited a distinct 205 eV onset absorption band for Nb $M_{4,5}$ (Figure 2.5e), which indicates that Nb atoms are present on the surface of the particles. In comparison, we did not observe Pt-Nb alloy formation in the Pt/NbC (bulk) catalysts that were tested under the same

conditions (Figure S2.11). This finding is consistent with previous work showing that Pt did not form an alloy with bulk carbide at moderate temperature, including Mo_2C that had been reduced at 450 °C[26], and those findings emphasizes the significant role that the reducibility of MXenes plays in the RMSI.

Figure 2.5f shows nanoparticles supported by three-atom-thick Nb_2CT_x MXene layers. The MXene layers that are close to the nanoparticles decomposed (discontinued), and sacrificial layers were formed directly beneath the Pt-Nb particles. Taking the *in situ* XAS results in conjunction with the XPS results, this sacrificial layer may be the result of RMSI occurring at the interface between MXene and the nanoparticles. In addition, with the removal of surface terminations such as -OH, -O and -F, exposed terminal Nb sites are generated on the surface of the Nb_2CT_x MXene support. These exposed Nb metal terminals are in contact with the Pt-Nb surface alloy and form interfaces that have strong affinities for H_2O or OH, as indicated by the WGS kinetics. The RMSI stabilizes and disperses the nanoparticles (~2.6 nm), which creates more interfaces than Pt/NbC (bulk) catalysts. Since the active sites of the WGS reaction are often thought to be the metal-support interfaces that are responsible for H_2O dissociation[27], those newly generated interfaces (with higher H_2O coverage than the Pt/Al_2O_3) are presumed to make Pt/Nb_2CT_x an active WGS catalyst. Thus, the Pt/Nb_2CT_x catalyst becomes involved in RMSI after reduction at the moderate temperature (350 °C), which likely tunes the catalytic properties through alloy formation as well as modifying the admetal-support interface. Neither of these effects can be achieved using conventional bulk metal carbides.

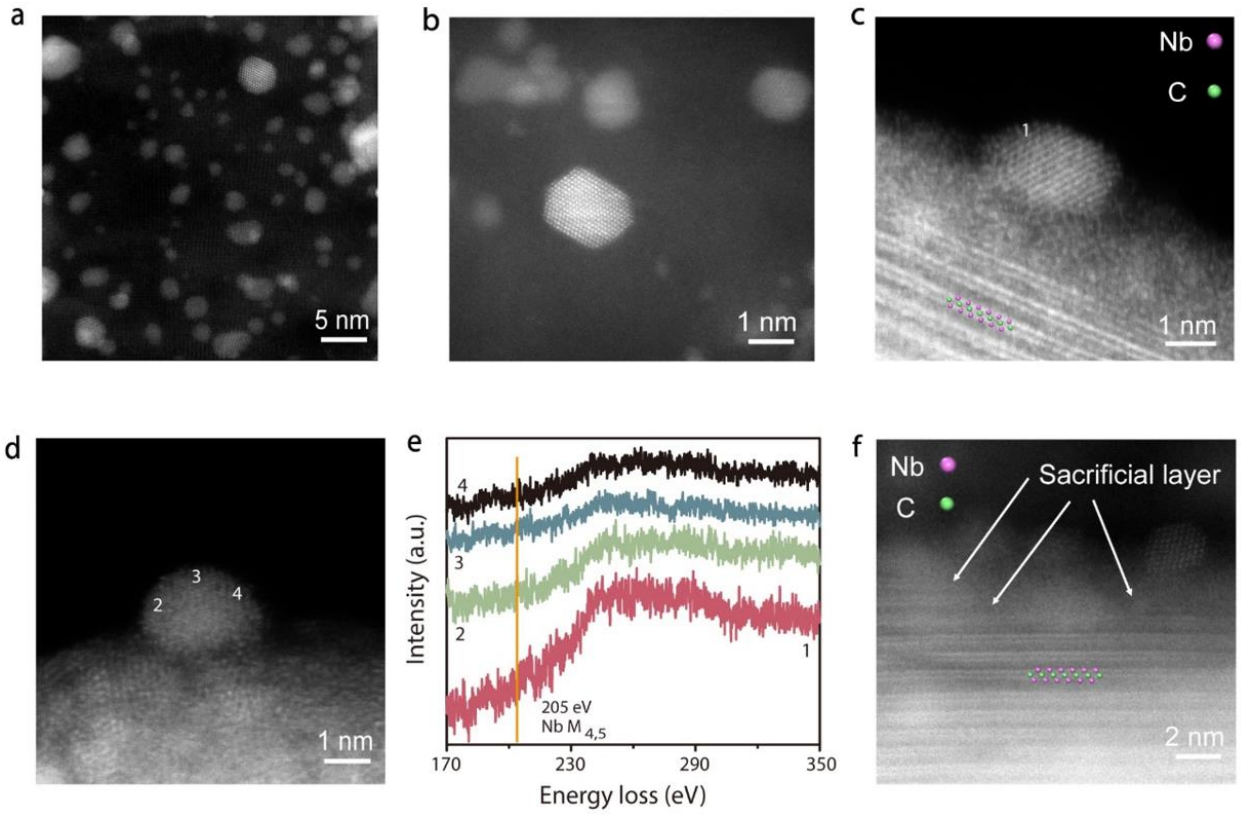

Figure 2.5 Electron microscopy and spectroscopy of spent 1% Pt/Nb_2CT_x catalyst. (a,b) HAADF-STEM images of the post-WGS 1%Pt/Nb_2CT_x catalyst. (c,d) HAADF-STEM images of typical nanoparticles supported by Nb_2CT_x MXene. The majority of each particle is hanging over the vacuum to avoid Nb interference from the support. (e), Electron energy loss spectra acquired at several points on the particle surface. (f) HAADF-STEM image showing discontinuous Nb_2CT_x MXene layers.

Previous studies have shown that surface functional groups are not unique to Nb_2CT_x[9]. Considering the shared characteristics such as reducible surface terminations and 2D structures of the MXene family (prepared by etching)[10], it is anticipated that the RMSI between Pt and Nb_2CT_x MXene also applies to other MXene materials. We further investigated $Ti_3C_2T_x$, another important member in the MXene family, as the support for platinum. EDS elemental mapping was acquired in an area where nanoparticles were partially attached to the $Ti_3C_2T_x$ support to avoid the Ti signals from the MXene. The distribution of Pt and Ti overlapped through the nanoparticles, indicating the formation of Pt-Ti bimetallic structures. This result suggests that the RMSI can be extended to

members in the MXenes family other than Nb_2CT_x, which represents the generality of using MXenes as supports for preparing bimetallic catalysts.

2.4 Conclusion

In summary, we have demonstrated that 2D Nb_2CT_x MXene can be utilized as support for Pt and become involved in RMSI after reduction at a moderate temperature (350 °C). The RMSI induces the formation of a bimetallic surface alloy and admetal-Nb_2CT_x interfaces on the surface of the material that impacts CO adsorption, H_2O activation and ultimately the kinetics of the WGS reaction. The highly reducible surface of Nb_2CT_x is vital to the introduction of RMSI. The RMSI can be further extended to Pt/$Ti_3C_2T_x$ system with the formation of Pt-Ti bimetallic nanoparticles. Together, our results establish that the RMSI between Pt and 2D carbides is likely a general phenomenon for members of the MXene family, which will open new avenues for designing bimetallic catalysts.

2.5 Methods

2.5.1 Synthesis of Nb_2AlC Phase

The Nb_2AlC powder is synthesized by spark plasma sintering (SPS) of Nb/Al/graphite mixtures. Commercial powders of niobium (99.8%, 325-mesh), graphite (99%, 7-11 μm) and aluminum (99.5%, 325 mesh) were mixed in a molar ratio of Nb:Al:C = 2:1.4:0.9 in a graphite die coated with boron nitride (BN). Excess Al and less than a full equivalent of graphite were added because Al will be lost during high-temperature processing, and carbon deficiencies exist in most Al-containing MAX phases[28,29]. Then, the material was loaded in a Fuji-211lx SPS system and sintered at 1500 °C under 30 MPa for one hour. The resulting Nb_2AlC was then pulverized and sieved through a 325-mesh screen.

2.5.2 Preparation of Nb_2CT_x MXene

Approximately 1 g of the prepared Nb_2AlC powder was immersed in 10 mL of 50%

aqueous hydrofluoric acid (HF) solution for approximately 3 days at 55 °C. The resulting MXene suspension was repeatedly washed with deionized water (DI) and centrifuged at 8900 rpm until the pH reached ~ 5. The final MXene was dried under vacuum at room temperature and stored in a glove box until usage.

2.5.3 Preparation of the Pt/Nb_2CT_x Catalysts

Tetraamine platinum nitrate (Sigma-Aldrich, 99.995%) was loaded on the Nb_2CT_x MXene and bulk NbC (Sigma-Aldrich, 99%) supports by IWI. Specifically, a certain amount of Pt precursor was dissolved in deionized water to generate a solution with a concentration of 0.02 g Pt/mL. The solution was then added dropwise to the support until incipient-wetness (approximately 0.5 mL per gram of support). The mixture was then dried under vacuum at room temperature. The procedure was repeated once so the final catalyst (referred to as Pt/Nb_2CT_x fresh) had an empirical Pt loading of approximately 1-2%.

2.5.4 Determination of the WGS Reaction Kinetics

The WGS reaction was monitored in a parallel plug flow reactor, which was described previously[30]. The WGS reaction rates were measured under differential conditions, namely, the conversion was maintained below 10%, and the products of the WGS reaction (CO_2 and H_2) were also co-fed into the reaction system. The WGS rate can be expressed by the power rate law given below:

$$r = Aexp\left(-\frac{E_{app}}{RT}\right)[CO]^a[CO_2]^b[H_2]^c[H_2O]^d(1-\beta) \qquad (1)$$

where r is the overall rate, A and E_{app} are the apparent pre-exponential factor and activation energy for the forward rate, respectively, a, b, c and d are the forward reaction orders, $\beta = ([CO_2][H_2])/(K_{eq}[CO][H_2O])$ is the approach to equilibrium, which measures the deviance from the equilibrium conditions and K_{eq} is the equilibrium constant for the WGS reaction. Under the

WGS conditions tested here, $\beta \ll 1$, implying the reaction is far from equilibrium.

For each measurement, approximately 300 mg of the as-prepared Pt/Nb_2CT_x catalyst was loaded into the reactor. The catalyst was pretreated by reduction in 25% H_2/Ar at 350 °C for 2 hours (the total flow rate was 50 mL min^{-1}, and the temperature ramping rate was 5 °C min^{-1}). After pretreatment, the temperature was decreased to 300 °C, and the catalysts were exposed to the WGS reaction mixture (standard conditions, 6.8% CO, 21.9% H_2O, 8.5% CO_2, 37.4% H_2, and balance Ar) at a flow rate of 75.4 mL min^{-1}. The catalyst was stabilized at 300 °C for a period of approximately 20 hours to reach initial stabilization. The apparent reaction orders were measured over the stabilized catalyst by varying the partial pressures of one component at a time over the range of 4-21% for CO, 5-25% for CO_2, 11-34% for H_2O, and 14-55% for H_2. The WGS reaction rate under standard conditions was determined after evaluation of each apparent reaction order to measure the deactivation if there was any. For this catalyst, after the initial stabilization period, no significant deactivation was observed during the full test period (approximately 50 hours). The apparent activation energy was measured under standard condition by varying the temperature between 290 °C and 320 °C. The WGS rate was normalized by the total Pt loading or by the number of surface Pt atoms as determined by CO chemisorption. After all measurements had been taken, the catalysts were passivated at room temperature in 30 mL min^{-1} 2% O_2/Ar gas flow for 4 hours before they were removed from the reactors.

2.6 Acknowledgments

Y. Wu appreciates the support from the Herbert L. Stiles Professorship and the ACRI Center Initiative at Iowa State University. F. Ribeiro thanks the support provided by the U.S. Department of Energy, Office of Basic Energy Sciences, through Catalysis Science Grant No. DE-FG02-03ER15466.

2.7 Author Contributions

Z.L. conceived the research and performed the synthesis and material characterizations. Y.C. and F.R. carried out the CO chemisorption and WGS kinetics measurements. Z.W. and J.M carried out the XAS measurements. L.Z, G.M., B.X and E. Shi conducted the TEM and HAADF-EDS analyses. C. M performed the XPS experiments. Y. W supervised and led the project. Z.L., Y.C. and Z.W. contributed equally to this work.

2.8 References

1 Yu, W., Porosoff, M. D. & Chen, J. G. Review of Pt-based bimetallic catalysis: from model surfaces to supported catalysts. *Chem. rev.* **112**, 5780-5817 (2012).

2 Sankar, M. *et al.* Designing bimetallic catalysts for a green and sustainable future. *Chem. Soc. rev.* **41**, 8099-8139 (2012).

3 Wang, H., Wang, C., Yan, H., Yi, H. & Lu, J. Precisely-controlled synthesis of Au@Pd core–shell bimetallic catalyst via atomic layer deposition for selective oxidation of benzyl alcohol. *J Catal.* **324**, 59-68 (2015).

4 Armbrüster, M. Intermetallic Compounds in Catalysis, Encyclopedia of Catalysis, Wiley-VCH, Weinheim, 2011.

5 Penner, S. & Armbrüster, M. Formation of intermetallic compounds by reactive metal–support interaction: a frequently encountered phenomenon in catalysis. *ChemCatChem* **7**, 374-392 (2015).

6 Wang, D. *et al.* Silicide formation on a Pt/SiO_2 model catalyst studied by TEM, EELS, and EDXS. *J. Catal.* **219**, 434-441 (2003).

7 Penner, S. *et al.* Platinum nanocrystals supported by silica, alumina and ceria: metal–support interaction due to high-temperature reduction in hydrogen. *Surf. Sci.* **532**, 276-280 (2003).

8 Lukatskaya, M. R. *et al.* Cation intercalation and high volumetric capacitance of two-dimensional titanium carbide. *Science* **341**, 1502-1505 (2013).

9 Naguib, M., Mochalin, V. N., Barsoum, M. W. & Gogotsi, Y. 25th anniversary article: MXenes: a new family of two-dimensional materials. *Adv. Mater.* **26**, 992-1005 (2014).

10 Anasori, B., Lukatskaya, M. R. & Gogotsi, Y. 2D metal carbides and nitrides (MXenes) for energy storage. *Nat. Rev. Mater.* **2**, 16098 (2017).

11 Ma, T. Y., Cao, J. L., Jaroniec, M. & Qiao, S. Z. Interacting Carbon Nitride and Titanium Carbide Nanosheets for Hig-Performance Oxygen Evolution. *Angew. Chem. Int. Ed.* **55**, 1138-1142 (2016).

12 Ran, J. *et al.* Ti_3C_2 MXene co-catalyst on metal sulfide photo-absorbers for enhanced visible-light photocatalytic hydrogen production. *Nat. Commun.* **8**, 13907 (2017).

13 Schreier, M. & Regalbuto, J. R. A fundamental study of Pt tetraammine impregnation of silica: 1. The electrostatic nature of platinum adsorption. *J. Catal.* **225**, 190-202 (2004).

14 Lambert, S. *et al.* Synthesis of very highly dispersed platinum catalysts supported on carbon xerogels by the strong electrostatic adsorption method. *J. Catal* .**261**, 23-33 (2009).

15 Lu, J., Zhang, X., Bravo-Suarez, J. J., Fujitani, T. & Oyama, S. T. Effect of composition and promoters in Au/TS-1 catalysts for direct propylene epoxidation using H_2 and O_2. *Catal. Today* **147**, 186-195 (2009).

16 Rakhi, R., Ahmed, B., Hedhili, M. N., Anjum, D. H. & Alshareef, H. N. Effect of postetch annealing gas composition on the structural and electrochemical properties of Ti_2CT_x MXene electrodes for supercapacitor applications. *Chem. Mater.***27**, 5314-5323 (2015).

17 Naguib, M. *et al.* New two-dimensional niobium and vanadium carbides as promising materials for Li-ion batteries. *J. Am. Chem. Soc.***135**, 15966-15969 (2013).

18 Sabnis, K. D. *et al.* Water–gas shift catalysis over transition metals supported on molybdenum carbide. *J. Catal.* **331**, 162-171 (2015).

19 Shekhar, M. Water-gas shift catalysis over supported gold and platinum nanoparticles. (2012).

20 Sabnis, K. D. *et al.* Probing the active sites for water–gas shift over Pt/molybdenum carbide using multi-walled carbon nanotubes. *J. Catal.* **330**, 442-451 (2015).

21 Balakrishnan, K. & Schwank, J. A chemisorption and XPS study of bimetallic Pt-Sn/Al_2O_3 catalysts. *J. Catal.***127**, 287-306 (1991).

22 Wakisaka, M. *et al.* Electronic structures of Pt-Co and Pt-Ru alloys for CO-tolerant anode catalysts in polymer electrolyte fuel cells studied by EC-XPS. *J. Phys. Chem. B* **110**, 23489-23496 (2006).

23 Beard, B. C. & Ross, P. N. Platinum-titanium alloy formation from high-temperature reduction of a titania-impregnated platinum catalyst: implications for strong metal-support interaction. *J. Phys. Chem.* **90**, 6811-6817 (1986).

24 Hammer, B., Morikawa, Y. & Nørskov, J. K. CO chemisorption at metal surfaces and overlayers. *Phys. Rev. Lett.* **76**, 2141 (1996).

25 Gauthier, Y. *et al.* Adsorption sites and ligand effect for CO on an alloy surface: a direct view. *Phys. Rev. Lett.* **87**, 036103 (2001).

26 Schaidle, J. A., Schweitzer, N. M., Ajenifujah, O. T. & Thompson, L. T. On the preparation of molybdenum carbide-supported metal catalysts. *J. Catal.* **289**, 210-217 (2012).

27 Cui, Y. *et al.* Participation of interfacial hydroxyl groups in the water-gas shift reaction over Au/MgO catalysts. *Catal. Sci. & Technol.* (2017).

28 Hu, C. *et al.* In situ reaction synthesis, electrical and thermal, and mechanical properties of Nb_4AlC_3. *J. Am. Ceram. Soc.* **91**, 2258-2263 (2008).

29 Wang, X. & Zhou, Y. Microstructure and properties of Ti_3AlC_2 prepared by the solid–liquid reaction synthesis and simultaneous in-situ hot pressing process. *Acta. Mater.* **50**, 3143-3151 (2002).

30 Bollmann, L. *et al.* Effect of Zn addition on the water-gas shift reaction over supported palladium catalysts. *J. Catal.* **257**, 43-54 (2008).

2.9 Supplementary Methods

Powder X-ray diffraction (XRD) was carried out on a Rigaku Ultima U4 diffractometer, with Cu Kα radiation (λ = 1.5418 Å), at 40 kV and 44 mA. Scanning electron microscopy (SEM) was acquired on a FEI Quanta 250. Aberration-corrected high angle annular dark field scanning transmission electron microscopy (HAADF-STEM) images and electron energy loss spectroscopy (EELS) were acquired on a Titan Themis 300 probe corrected TEM equipped with a Super-X EDX detector at Sensitive Instrument Facility (SIF) of Ames Lab.

Pt loading of the catalysts was determined by atomic absorption spectroscopy (AAS). Specifically, the catalyst was digested by aqua regia in a Nalgene® amber polyethylene bottle for 3 days, and the solution was then diluted to desired concentration for the AAS measurement.

H_2 temperature programmed reduction (TPR) experiment was performed with an Autochem 2000 unit. About 70 mg of the Nb_2CT_x support was loaded in the unit and dried in 50 sccm He at 200 ^oC overnight. Then the catalyst was cooled to room temperature and purged with

pure H_2. The temperature was ramped from room temperature to 900 °C under 50 sccm pure H_2. The products were analyzed by a mass spectroscopy.

CO chemisorption was measured with an ASAP 2020 unit. About 100 mg of the fresh Pt/ Nb_2CT_x catalyst was loaded and reduced at 350 °C in pure H_2 before measuring for CO chemisorption. CO/Pt stoichiometry factor of 1 was used to calculate the Pt dispersion.

Due to the low CO adsorption quantity on the catalyst, sub-ambient temperature CO pulse chemisorption was performed on a Micromeritics Autochem 2920 unit. Typically, about 100 mg of the fresh catalyst was loaded and reduced at 350 °C for 1 hour in 10% H_2/Ar with a total flow of 30 mL/min. Then the system was flushed with He and the sample was cooled to –30 °C. After reaching the stable temperature, CO pulse was introduced and the accumulated adsorption quantity was calculated.

XPS data were obtained using a Kratos Axis Ultra DLD spectrometer with monochromic Al Kα radiation (1486.6 eV) at pass energy of 20 and 160 eV for high-resolution and survey spectra, respectively. A commercial Kratos charge neutralizer was used to avoid non-homogeneous electric charge of non-conducting powder and to achieve better resolution. The resolution measured as full width at half maximum of the curve fitted C 1s peak was approximately 1 eV. Binding energy (BE) values refer to the Fermi edge and the energy scale was calibrated using Au $4f_{7/2}$ at 84.0 eV and Cu $2p_{3/2}$ at 932.67 eV. XPS data were analyzed with CasaXPS. Curve-fitting was performed following a linear or Shirley background subtraction using Gaussian/Lorentzian peak shapes (GL and LF). The atomic concentrations of the elements in the near-surface region were estimated considering the corresponding Scofield atomic sensitivity factors and inelastic mean free path (IMFP) of photoelectrons using standard procedures in the CasaXPS software. For the quasi *in situ* XPS measurements, sample treatments were performed in

a reaction cell ($\approx$30 cm^3) connected to the XPS spectrometer and all samples were reduced in 5% H_2 at least for 30 minutes. Then the samples were moved between the reaction cell and the analysis chamber under ultrahigh vacuum (UHV) conditions without the exposure to air (considered as reduced samples).

X-ray absorption measurements were acquired at the Nb K edge (18.9856 keV) and Pt L_{III} edge (11.5640 keV) on the bending magnet beam line of the Materials Research Collaborative Access Team (MRCAT) at the Sector 10 in the Advanced Photon Source, Argonne National Laboratory. Measurements were made in transmission step-scan mode. The ionization chambers were optimized for the maximum current with linear response with 10% absorption in the incident ion chamber and 70% absorption in the transmission detector. A third detector in series simultaneously collected a Nb or Pt metal foil reference spectrum with each measurement for energy calibration. Solid samples were pressed into a cylindrical sample holder consisting of six wells, forming a self-supporting wafer. The sample holder was placed in a quartz reactor tube sealed with Kapton windows by two ultra-torr fittings through which gas could be flowed. Nb_2CT_x materials, parent Nb_2AlC and reference compounds Nb_2O_5, NbO_2, NbC (Sigma-Aldrich) were scanned in air. Fresh Pt on Nb_2CT_x catalyst were reduced in 3% H_2/He with a flow rate of 50 cm^3/min at 350 or 550 ^oC for at least 30 min, then cooled to room temperature and flushed with He before they were scanned. The 1% Pt/Nb_2CT_x catalysts after water-gas-shift reaction were scanned in air.

The fits of the Extended X-ray Absorption Fine Structure (EXAFS) were evaluated using Artemis software[1]. The EXAFS coordination parameters were obtained by a least-squares fit in R-space of k^2-weighted Fourier transform data together. The data range is from 3.0 to 12.0 $Å^{-1}$ in k space. For R space, the data was fitted from 1.0 to 3.0 Å in R space at the Nb edge and 1.6 to 3.2

Å at the Pt edge. The S_0^2 value was obtained at Nb edge by fitting the NbC standard and at Pt edge by fitting Pt foil. The bond distances were adjusted based on initial inputs from standard crystal structure information files of Nb_2AlC and Pt_3Nb for the fits of Nb edge and Pt edge, respectively[2,3].

2.10 Langmuir-Hinshelwood Mechanism

The detailed derivation of the Langmuir-Hinshelwood mechanism can be found in the book[4] Concepts of Modern Catalysis and Kinetics by I. Chorkendorff and J. W. Niemantsverdriet. Generally, for a mixture of reactant A and B:

$$A + B \rightarrow C$$

$$\theta_A = \frac{K_A p_A}{1 + K_A p_A + K_B p_B + K_C^{-1} p_C}$$

$$\theta_B = \frac{K_B p_B}{1 + K_A p_A + K_B p_B + K_C^{-1} p_C}$$

Where θ_A and θ_B are the fraction of the available surface sites covered by species A or B at equilibrium, K_i is the adsorption equilibrium constant for species i and p_i is the partial pressure of species i. The dependence of K_i on temperature makes θ_i temperature dependent. θ_i also depends on the heat of adsorption of species A and B. In turn, the apparent reaction orders with respect to such species involved in the reaction depend not only on the gas phase concentration but also on the reaction temperature. It is therefore necessary to measure the kinetic data over different catalysts at same temperature for objective comparison of relative surface concentrations of reactive species. If we assume the quasi-equilibrium assumption, which means only one elementary step determines the rate and all the other steps are in quasi-equilibrium state, then the apparent reaction orders can be derived as $n_A = 1 - 2\theta_A$ and $n_B = 1 - 2\theta_B$, where n_A and n_B are the apparent reaction orders with respect to A and B. Although it is a simplified estimation

compared with our complex catalyst system here, it provides a quantitative picture about the relationship between the apparent reaction orders and the relative surface concentrations. The apparent reaction orders with respect to the reactants are thus negatively correlated with the corresponding relative surface coverage.

2.11 Supplementary Figures

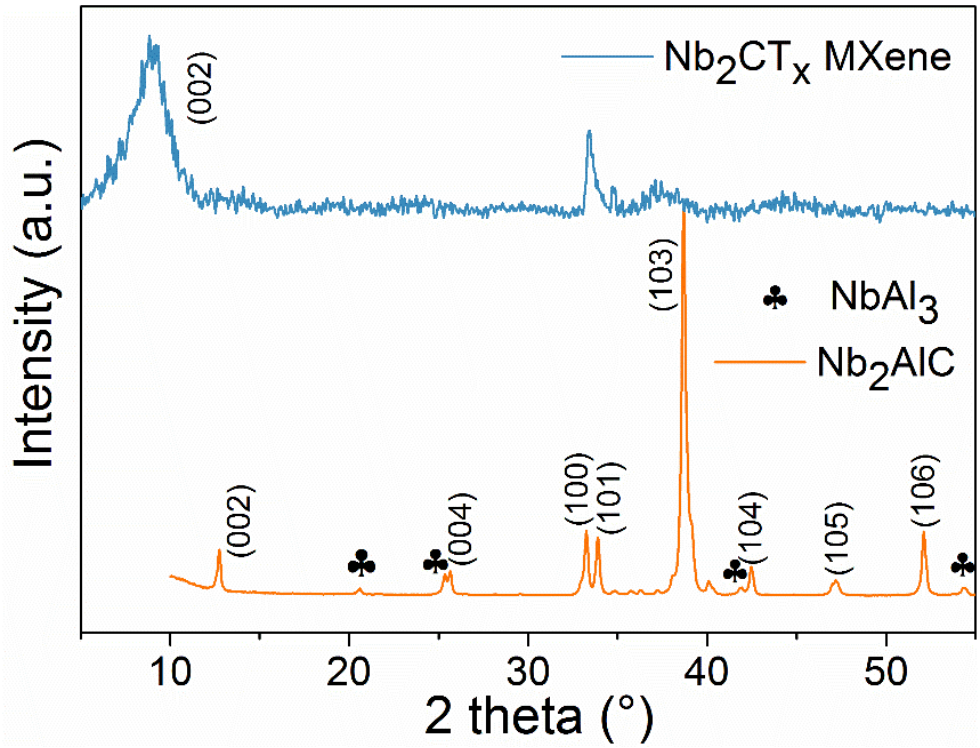

Figure S2.1 XRD patterns of Nb_2AlC MAX (Orange) phase and Nb_2CT_x MXene (Blue).

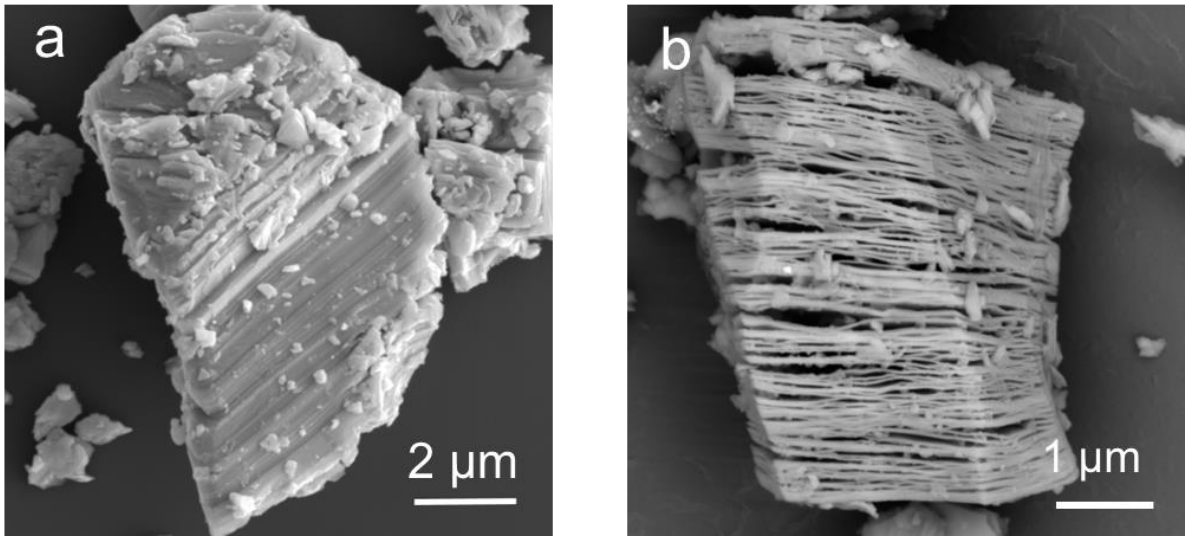

Figure S2.2 (a) SEM image of Nb_2AlC MAX. The as-synthesized Nb_2AlC shows the typical lamellar structure. (b) SEM image of 1% Pt/Nb_2CT_x after WGS reaction showing the Pt/Nb_2CT_x maintains the typical layered structure of MXene.

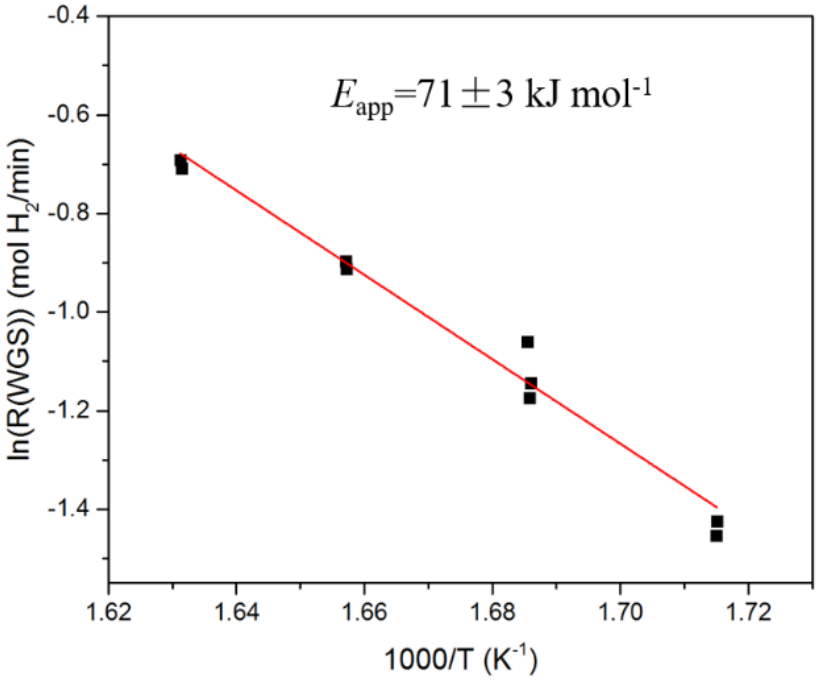

Figure S2.3 Arrhenius plots for WGS over 1% Pt/Nb_2CT_x-MXene catalyst. The WGS rates were measured in presence of 7% CO, 22% H_2O, 8.5% CO_2, 37% H_2, and balance Ar.

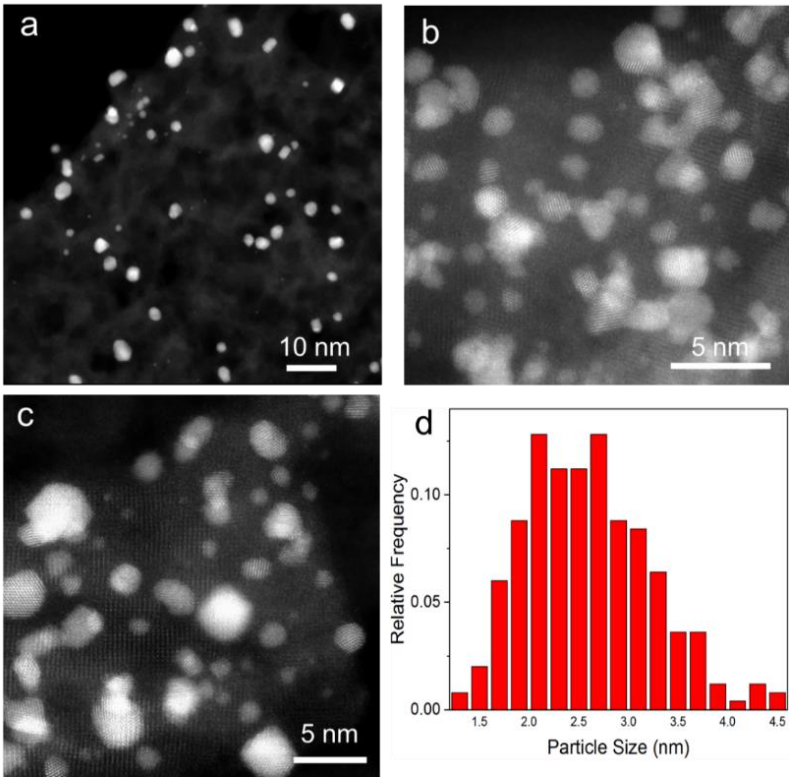

Figure S2.4 (a-c) HAADF-STEM images of 1% Pt/Nb_2CT_x after WGS reaction. (d) Particle size distribution statistics of used 1% Pt/Nb_2CT_x catalyst, and the average particle size is determined to be 2.6 ± 0.6 nm.

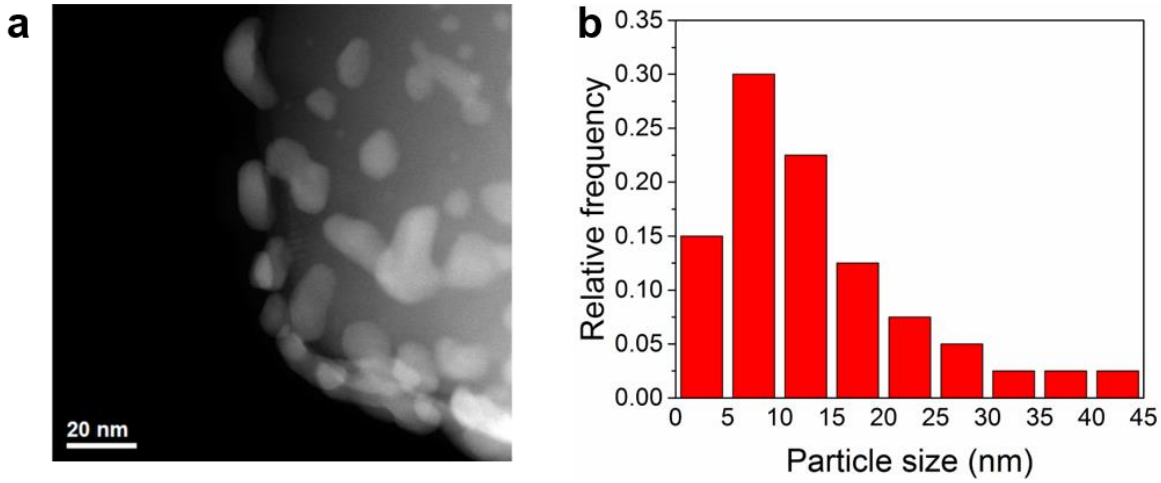

Figure S2.5 (a) HAADF-STEM image of 1% Pt/NbC (bulk) after WGS reaction. (b) Particle size distribution statistics of used 1% Pt/NbC (bulk), and the average particle size is determined to be 13.8 ± 9.6 nm.

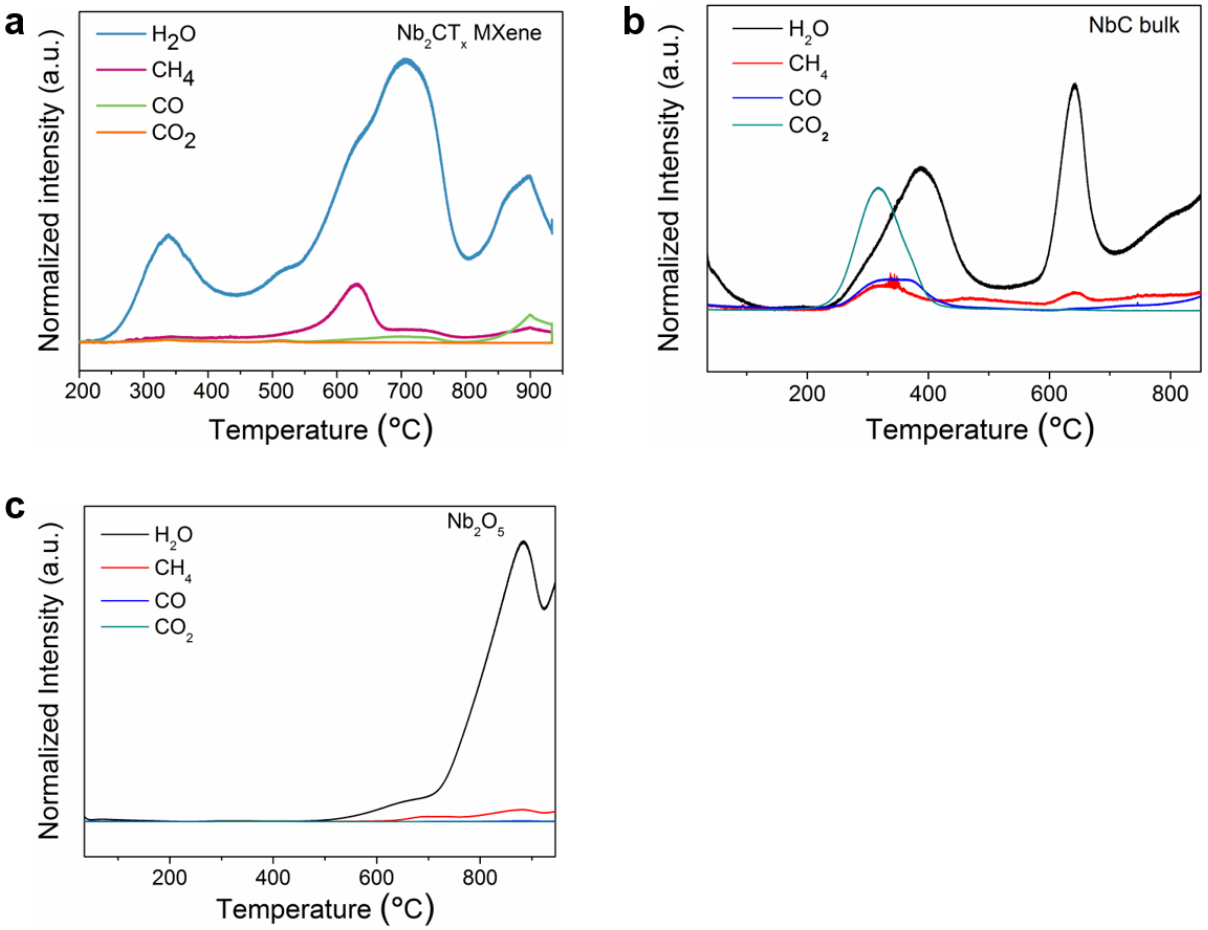

Figure S2.6 (a) Temperature programmed reduction (TPR) profile of Nb_2CT_x MXene. The H_2O peak around 340°C can be attributed to the reduction of O and OH terminations on the surface of Nb_2CT_x MXene, which is consistent with the results of the quasi *in situ* XPS. Comparing with the TPR profile of Nb_2O_5, the additional H_2O peaks located above 600 °C can be assigned to the reduction of residual Nb_2O_5 after HF etching[5]. The residue oxygen on the surface also desorbs as CO and CO_2[6] (b) TPR profile of commercial bulk NbC. The H_2O peaks at around 400 °C and 650 °C are likely due to the removal of the surface residue oxygen[7]. (c) TPR profile of commercial bulk Nb_2O_5. The peak between 800 °C and 900 °C is due to the reduction of Nb_2O_5 to NbO_2[8].

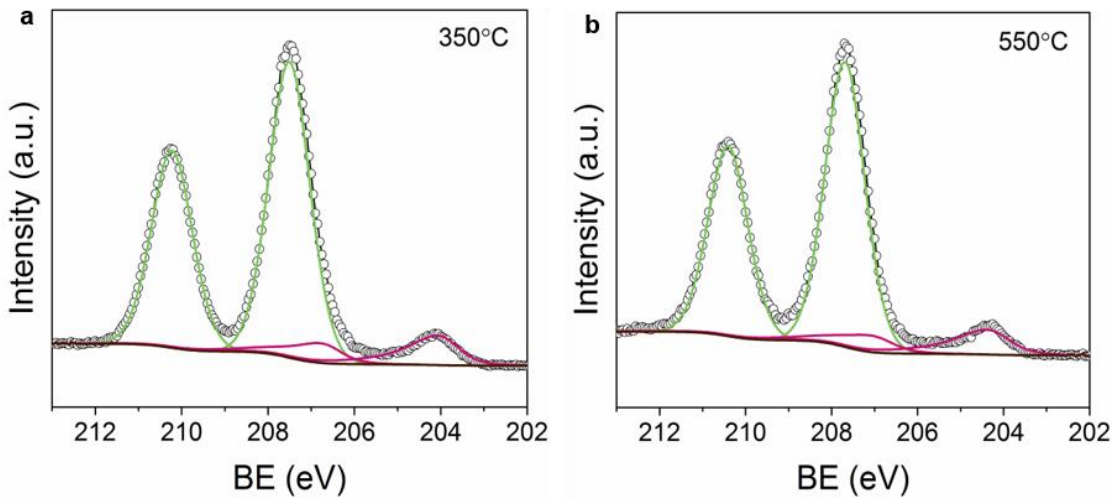

Figure S2.7 Quasi *in situ* XPS spectra of Nb 3d of pre-reduced 1% Pt/Nb_2CT_x sample (the fresh sample was reduced at 350 °C by H_2 and then exposed to air before the quasi *in-situ* XPS measurement) reduced at 350 °C and 550 °C again. These results indicate the enriched Nb_2O_5 induced by subsequent air exposure is not reducible by H_2 at 550 °C.

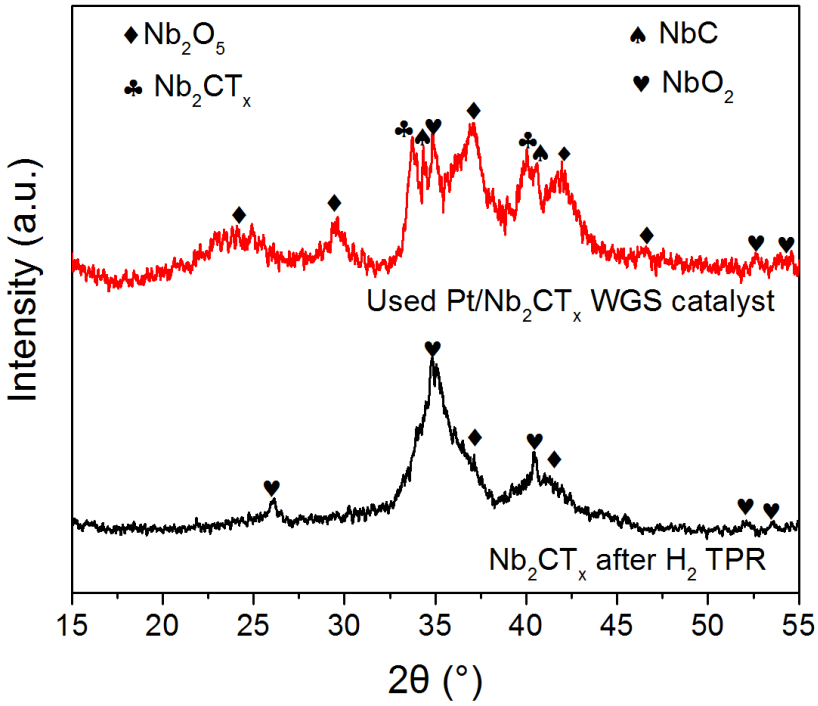

Figure S2.8 XRD patterns of spent 1% Pt/Nb_2CT_x catalyst after WGS reaction (red line) and Nb_2CT_x MXene after TPR treatment (black line).

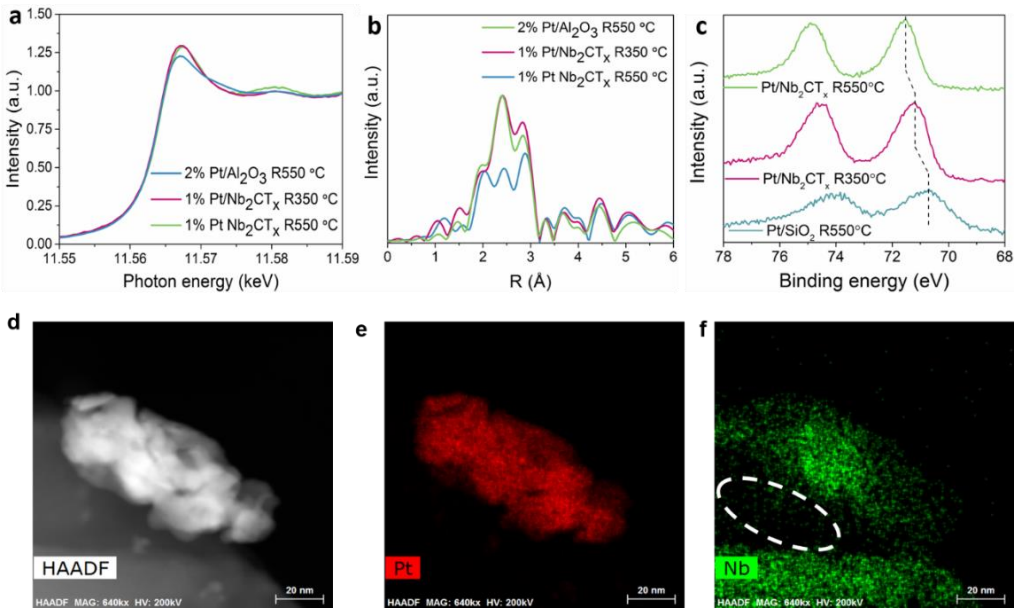

Figure S2.9 (a) *in situ* XANES spectra of Pt L_{III} edge of 2% Pt/Al_2O_3 sample treated at 550 °C and fresh 1% Pt/Nb_2CT_x treated at 350 °C and 550 °C in 3 % H_2/He. (b) Fourier transform magnitude of the k^2 EXAFS of 2% Pt/Al_2O_3 sample treated at 550 °C and fresh 1% Pt/Nb_2CT_x treated at 350 °C and 550 °C in 3 % H_2/He. (c) Quasi *in situ* XPS spectra of Pt $4f_{7/2}$ of Pt/SiO_2 reduced at 550 °C and Pt/Nb_2CT_x sample reduced at 350 °C and 550 °C. (d) HAADF-STEM image of fresh 1% Pt/Nb_2CT_x catalyst reduced in H_2 at 550 °C. Particle agglomerates after the high temperature (550 °C) reduction. (e) Elemental mapping of Pt. (f) Elemental mapping of Nb. A Nb deficient area is circled by the white dash line.

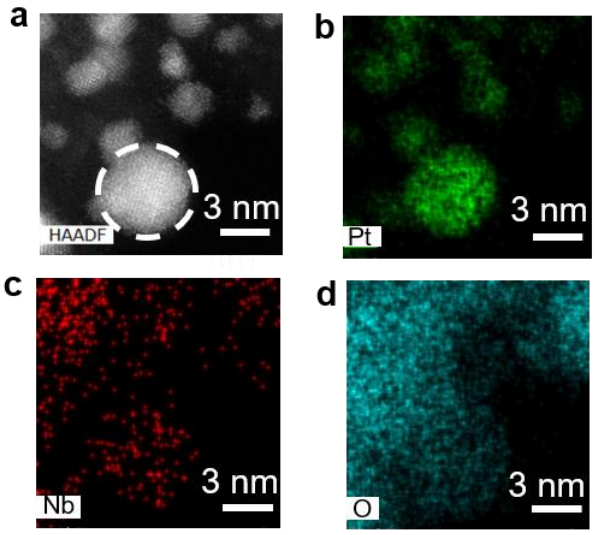

Figure S2.10 (a) HAADF-STEM image of used 1% Pt/Nb_2CT_x WGS catalyst. (b) Elemental mapping of Pt (c) Elemental mapping of Nb, (d) Elemental mapping of O. The area of interest is a nanoparticle which is hanging over vacuum to avoid Nb signal from the Nb_2CT_x support. The EDS result suggests that uniform bulk Pt-Nb alloy is not formed.

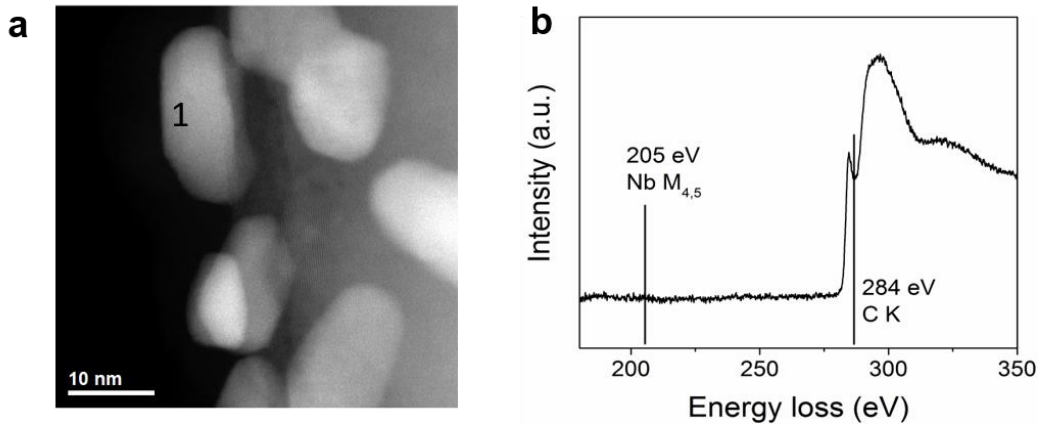

Figure S2.11 (a) HAADF-STEM image of used 1% Pt/NbC bulk catalyst. (b) Spectrum of electron-energy loss acquired at a point (marked as ''1'') on the particle surface. The absence of Nb $M_{4,5}$ absorption edge with onset at 205 eV indicates no Pt-Nb surface alloy is formed for Pt supported by bulk NbC. The signal of C can be caused by carbon lacey of the TEM grid or carbon contamination of the catalysts. Note the catalyst was synthesized and treated using the same procedure with 1% Pt/Nb_2CT_x WGS catalyst.

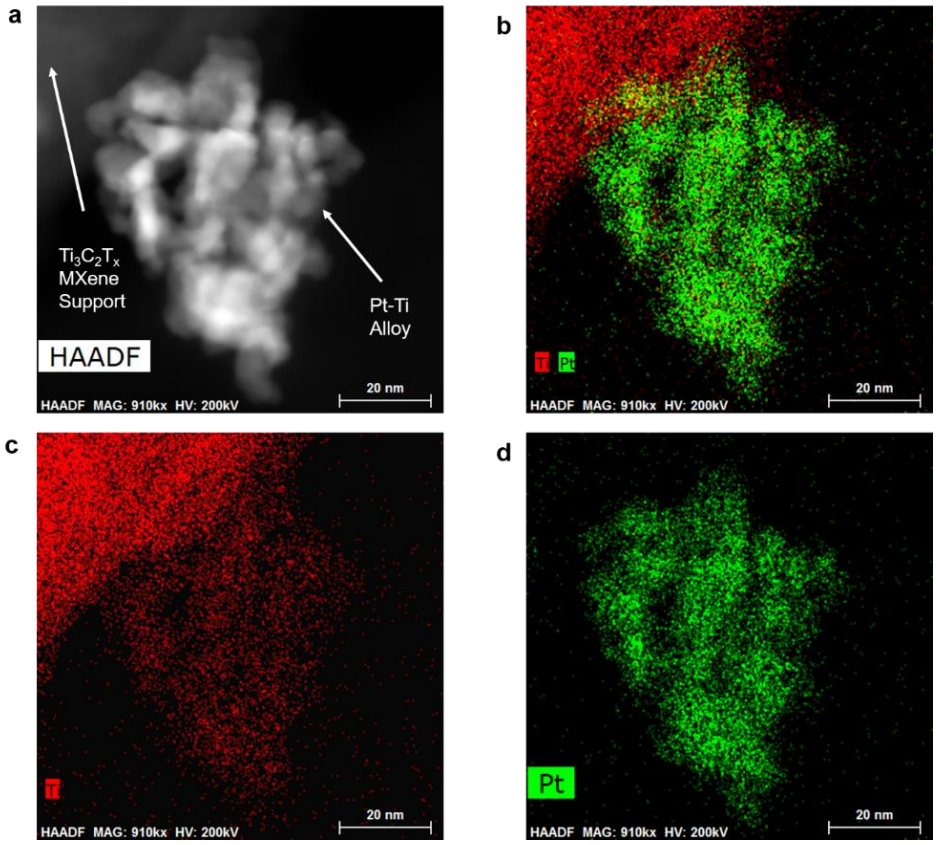

Figure S2.12 (a) HAADF-STEM image of fresh 1% Pt/$Ti_3C_2T_x$ catalyst reduced in H_2 at 550 °C. Particles agglomerated after the high temperature (550 °C) reduction. (b) Elemental mapping of Pt and Ti. (c) Elemental mapping of Ti, (d) Elemental mapping of Pt.

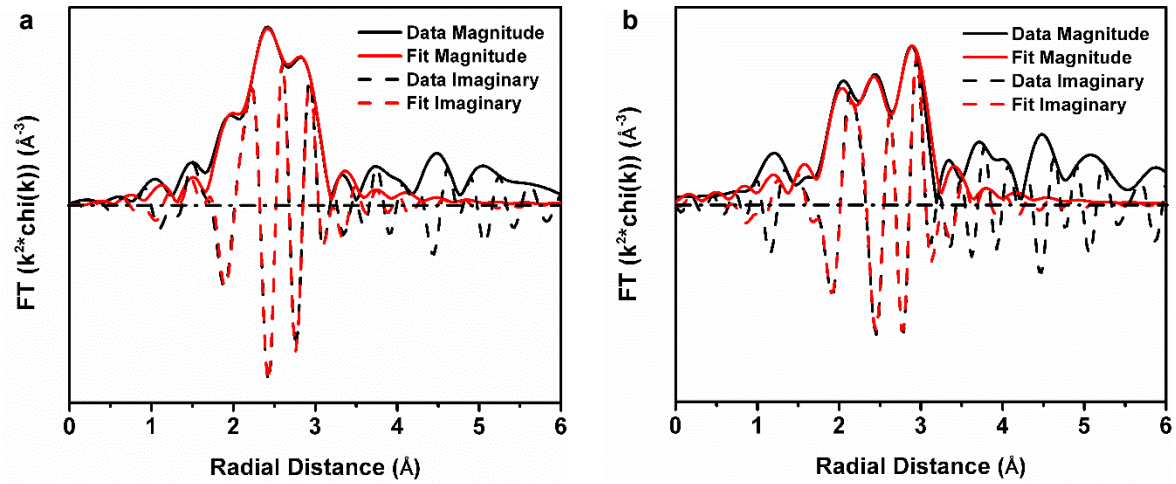

Figure S2.13 The magnitude and imaginary part of the Fourier Transform of the k^2 weighted EXAFS plot and corresponding first shell fit for Pt/Nb_2CT_x catalyst reduced at a) 350 °C and b) 550 °C. The fitting ranges are Δk = 2.7-11.7 $Å^{-1}$ and ΔR = 1.6-3.2 Å. Corresponding fitting results are as below.

Table S2.1 Quantitative evaluation of the EXAFS fit (Artemis Software)

Sample	Scattering Pair	S_0^2 *	CN *	Bond Length (Å) *	ΔE_0 (eV) *	σ^2 (Å ^{2}) *
Pt/Nb_2CT_x Reduced at 350 °C	Pt-Pt	0.8	7.4	2.75	4.2	0.005
	Pt-Nb		0.9	2.76		0.010
Pt/Nb_2CT_x Reduced at 550 °C	Pt-Pt	0.8	6.7	2.77	5.5	0.005
	Pt-Nb		1.8	2.75		0.008

* The S_0^2 is fixed at the value obtained by fitting a Pt foil reference. The errors of all the fitted parameters are very close. The average error in CN (coordination number) is 0.5, in bond length is 0.02 Å, in ΔE_0 is 0.8 eV and in σ^2 is 0.002 $Å^2$.

2.12 Supplementary Discussion

To test our hypothesis that only Pt-Nb surface alloy was formed for the 1% Pt/Nb_2CT_x catalyst reduced at 350 °C, we further increased reduction temperature to 550 °C. Stronger evidence is observed from EXAFS of Pt/Nb_2CT_x sample reduced at higher temperature (550 °C), which is substantially different from that of Pt/Nb_2CT_x reduced at 350 °C because of the incorporation of larger amount of Nb in the nanoparticles. Fitting the spectra gives CN=6.7 for Pt-Pt bonds (2.77 Å) and CN=1.8 for Pt-Nb bonds (2.75 Å). Quasi *in situ* XPS spectra show Pt $4f_{7/2}$ components have binding energies equal to 70.7 eV, 71.2 eV and 71.6 eV for Pt/SiO_2 sample reduced at 550 °C and Pt/Nb_2CT_x sample reduced at 350 °C and 550 °C, respectively. Pt-Nb alloy with higher degree is presumably formed, as indicated by the further binding energy shift for Pt/Nb_2CT_x reduced at higher temperature (550 °C vs 350 °C). The alloy formation is further confirmed by HAADF-STEM with X-ray spectroscopy (EDS) elemental mapping. Interestingly, a niobium deficient area is right beneath the alloy nanoparticle, which may imply diffusion of reduced Nb species.

Note the fitting results of XAS represent average numbers of the sample. The homogeneity and order of the alloys formed at 550 °C merit detailed study in the future.

2.13 Supplementary References

1 Athena, A. HEPHAESTUS: data analysis for X-ray absorption spectroscopy using IFEFFIT. *J. synchrotron rad.* **12**, 537-541 (2005).

2 Jeitschko, W., Nowotny, H. & Benesovsky, F. Kohlenstoffhaltige ternäre Verbindungen (H-phase). *Monatshefte für Chemie und verwandte Teile anderer Wissenschaften* **94**, 672-676 (1963).

3 Zhao, J., Gelato, L. & Parthé, E. Structure refinement of monoclinic 12-layer $TaNi_3$ with β-$NbPt_3$ type. New crystallographic descriptions of this type and of the Nb_3Rh_5 type based on smaller unit cells. *Acta Crystallogr., Sect. C: Cryst. Struct. Commun.* **47**, 479-483 (1991).

4 Chorkendorff, I. & Niemantsverdriet, J. W. *Concepts of modern catalysis and kinetics*. (John Wiley & Sons, 2017).

5 Nowak, I. & Jaroniec, M. "Hard" vs."Soft" Templating Synthesis of Mesoporous Nb_2O_5 Catalysts for Oxidation Reactions. *Top. Catal.* **49**, 193-203 (2008).

6 Ribeiro, F., Dalla Betta, R., Guskey, G. & Boudart, M. Preparation and surface composition of tungsten carbide powders with high specific surface area. *Chem. Mater.* **3**, 805-812 (1991).

7 Oyama, S. T., Schlatter, J. C., Metcalfe III, J. E. & Lambert Jr, J. M. Preparation and characterization of early transition metal carbides and nitrides. *Ind. Eng. Chem. Res.* **27**, 1639-1648 (1988).

8 Da Silva, V. T., Schmal, M. & Oyama, S. Niobium carbide synthesis from niobium oxide: study of the synthesis conditions, kinetics, and solid-state transformation mechanism. *J. Solid State Chem.* **123**, 168-182 (1996).

CHAPTER 3. TWO-DIMENSIONAL TRANSITION METAL CARBIDES (MXENES) AS SUPPORTS FOR TUNING THE CHEMISTRY OF CATALYTIC NANOPARTICLES

Zhe Li[1], Liang Yu[2], Cory Milligan[3], Tao Ma[4], Lin Zhou[4], Yanran Cui[3], Zhiyuan Qi[5], Nicole Libretto[3], Biao Xu[1], Junwei Luo[2], Enzheng Shi[1], Zhenwei Wu[3], Hongliang Xin[2], W. Nicholas Delgass[3], Jeffrey T. Miller[3], Yue Wu[1]

[1] Department of Chemical and Biological Engineering, Iowa State University, Ames, IA 50011, USA.

[2]Department of Chemical Engineering, Virginia Polytechnic Institute and State University, Blacksburg, Virginia 24061, USA.

[3] Davison School of Chemical Engineering, Purdue University, West Lafayette, IN 47907, USA.

[4] Ames Laboratory, Department of Energy, Ames, IA 50011, USA.

[5] Department of Chemistry, Iowa State University, Ames, IA 50011, USA.

Modified from a manuscript published in Nature Communications

3.1 Abstract

Supported nanoparticles are broadly employed in industrial catalytic processes, where the active sites can be tuned by metal-support interactions (MSIs). Although it is well accepted that supports can modify the chemistry of metal nanoparticles, systematic utilization of MSIs for achieving desired catalytic performance is still challenging. The developments of supports with appropriate chemical properties and identification of the resulting active sites are the main barriers. Here, we develop two-dimensional transition metal carbides (MXenes) supported platinum as efficient catalysts for light alkane dehydrogenations. Ordered Pt_3Ti and surface Pt_3Nb intermetallic compound nanoparticles are formed via reactive metal-support interactions on $Pt/Ti_3C_2T_x$ and

Pt/Nb_2CT_x catalysts, respectively. MXene supports modulate the nature of the active sites, making them highly selective toward C-H activation. Such exploitation of the MSIs makes MXenes promising platforms with versatile chemical reactivity and tunability for facile design of supported intermetallic nanoparticles over a wide range of compositions and structures.

3.2 Introduction

Metal nanoparticles (NPs) are widely used as heterogeneous catalysts and in electrochemical applications[1-3]. The performance of the supported metal NPs, including the rate, selectivity and stability, can be tailored by controlling their interactions with the supports[4-7]. These metal-support interactions (MSIs) have been found to modify the geometric and electronic structures of active sites[8,9], and, not surprisingly, the chemical properties of the supports are crucial to the modifications[10]. Nonetheless, rational design of supported catalysts through MSIs is often arduous, especially when the supports undergo structural changes under reaction conditions[11]. A classic example is the encapsulation of metal active sites by reducible oxide-support overlayers, which was designated by Tauster *et al*. as the strong-metal support interaction (SMSI) in 1978[12]. In the SMSI state the active metal sites on the NPs are covered due to the migration of suboxide species, which renders the loss of adsorption capability of the NPs[12,13]. Supports with ideal chemical tunability and reactivity are clearly a key to harnessing the potential promotional effects of MSIs on supported metal NP catalysts, but their development remains a grand challenge.

Two-dimensional (2D) early transition metal carbides, i.e., MXenes, is a burgeoning class of materials with well-defined structures and widely tunable compositions[14]. They have a formula of $M_{n+1}X_nT_x$, where M is an early transition metal, X refers to carbon and/or nitrogen, and T stands for surface functional groups[15]. We have recently shown that MXenes are promising supports for nanoparticle (NPs) catalysts and that the presence of noble metal NPs promotes both the removal of surface functional groups and reduction of the M component of the MXene[16]. Reduction of

these catalyst supports can lead to targeted delivery of the metal components in the supports to the NPs that contact the support surface. As a result, formation of ordered intermetallic compounds (IMCs) through reactive metal-support interactions (RMSIs) is possible[17]. RMSI refers to a chemical reaction between a metal and the support that induces the formation of bimetallic structures, which is differentiated from the more general SMSI because it is driven by the high thermodynamic stability of the resulting IMCs. MXenes can facilitate this process by having 2D structures with metal carbon bonds (M-C) that are weaker compared to the metal oxygen bonds (M-O) in typical oxide supports. This enhanced chemical reactivity can allow RMSIs to occur at lower temperature and, thus, favor the control of particle size, in contrast to the high temperature reduction required for early transition metal oxides or bulk carbides[18-20]. On MXenes intermetallic compounds may be formed that are not possible on traditional oxide and carbide supports and their properties controlled through *in situ* reduction at moderate temperature.

Here, we report two examples of thermally stable intermetallic NP catalysts prepared via RMSI between platinum and MXenes. A complete, full Pt_3Ti IMC with Cu_3Au type structure is formed in $Pt/Ti_3C_2T_x$ catalysts. For Pt/Nb_2CT_x catalysts, NPs with a surface Pt_3Nb IMC in the same structure are formed, presumably via a process kinetically controlled by the diffusion of Nb species. These intermetallic structures have not been previously reported for Pt NPs catalysts supported by oxides and bulk carbides of Ti and Nb. The strong intermetallic bonds in these structures offer compositional and electronic modification of the actives sites. The result, in this case is that the catalysts become highly selective for light alkane dehydrogenation (LADH), a reaction in renewed interest due to shale gas boom[21]. Such reactive interaction is generally applicable between platinum NPs and MXene families. The Pt-M (M refers to early transition metals) IMCs are famous for their thermal stability with high enthalpy of formation, but their

preparation through co-reduction is challenging as early transition metals are oxyphilic[22,23]. Thus, MXenes pave an avenue for facile design of Pt-M NPs with a broad range of compositions and structures that are intractable to synthesize by traditional methods.

3.3 Results

3.3.1Two-Dimensionality of the MXene Supports

The two MXene supports, $Ti_3C_2T_x$ and Nb_2CT_x, were prepared by a chemical exfoliation process reported by the literature[14,24]. Briefly, Ti_3AlC_2 and Nb_2AlC compounds (MAX) were treated with HF to extract the aluminum layers and exfoliate the 2D early transition metal carbides (Figure 3.1a). In the X-ray diffraction (XRD) patterns (Figures S3.1a, b), the shift of (002) peaks and the disappearance of the most intense nonbasal plane diffraction peaks of the MAX phases at $2\theta \approx 39°$ indicate that the MAX phases are converted to MXenes with increased c lattice parameters after the HF exfoliation. The scanning electron microscopy (SEM) images (Figure 3.1b, Figure S3.1c) display the typical accordion-like morphology of MXenes that suggests the exfoliation of individual grains along the basal planes. Dimethyl sulfoxide (DMSO) and tetrapropylammonium hydroxide (TPAOH) were employed as intercalants to delaminate Ti_3AlC_2 and Nb_2CT_x MXenes, respectively[25,26]. With the help of sonication, thin layers of MXenes nanosheets that are electron transparent can be obtained (Figure 3.1c, Figure S3.1d).

The chemical nature of the MXenes was investigated by X-ray absorption spectroscopy (XAS). Figure 3.1d shows that the Ti K edge X-ray absorption near edge spectroscopy (XANES) spectrum of $Ti_3C_2T_x$ has similar shape compared to that of bulk TiC rather than that of Ti foil or TiO_2. The edge energy of $Ti_3C_2T_x$ (4967.2 eV) is close to that of TiC (4967.1 eV), which is between the energies of Ti foil (4966.4 eV) and TiO_2 (4968.6 eV), indicating its carbide nature. The extended X-ray absorption fine structure (EXAFS) spectra (Figure 3.1e) compare the local coordination of the Ti atoms in the $Ti_3C_2T_x$ MXene to its bulk counterpart (TiC). $Ti_3C_2T_x$ shows

first-shell scattering (Ti-C/O/F) similar to that of TiC but with second-shell scattering (Ti-C-Ti) lower than that of TiC, consistent with the reduced dimensionality of the $Ti_3C_2T_x$ MXene and corresponding high portion of surface Ti atoms. Similar results were obtained for Nb_2CT_x by Nb K edge XAS in our previous work[16].

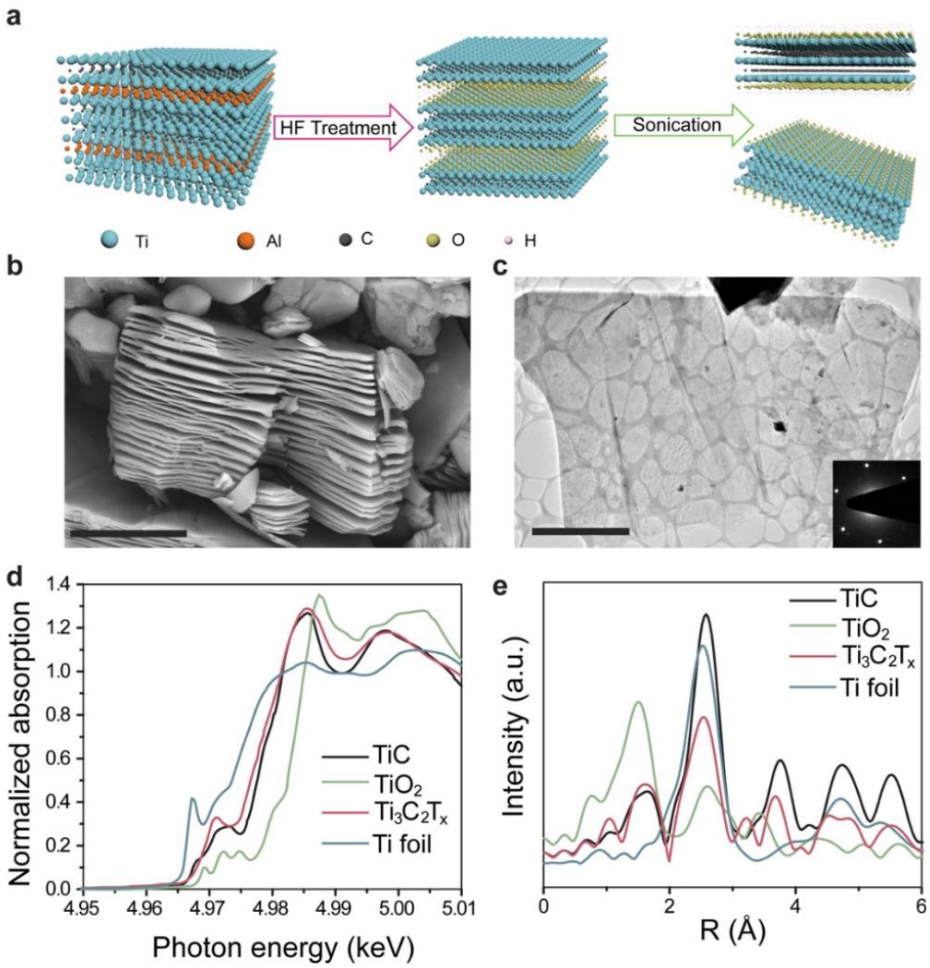

Figure 3.1 Characterization of $Ti_3C_2T_x$ MXene support. (a) Schematic of $Ti_3C_2T_x$ MXene preparation. (b) SEM image of $Ti_3C_2T_x$ MXene, the scale bar corresponds to 3 µm. (c) TEM image of $Ti_3C_2T_x$ MXene nanosheets. Inset represents the selected area electron diffraction (SAED) pattern showing hexagonal basal plane symmetry of $Ti_3C_2T_x$ MXene. The scale bar corresponds to 2 µm. (d) XANES spectra of the $Ti_3C_2T_x$ compared to references including Ti foil, TiO_2 and TiC. (e) Magnitude of the Fourier transform of the k^2 weighted EXAFS of the $Ti_3C_2T_x$ compared to TiC.

3.3.2 Characterizations of MXenes Supported Nanoparticles

Pt was loaded on the two MXene supports via incipient-wetness impregnation (IWI) as reported previously[16]. The Pt/MXene catalysts were further reduced with 5% H_2/N_2 at 550 °C, which is within the typical temperature range of LADH reactions[27]. High angle annular dark field scanning transmission electron microscopy (HAADF-STEM) shows that small NPs formed on both catalysts. The average particle diameters are about 6 ± 3.2 nm and 2.6 ± 0.7 nm for Pt/$Ti_3C_2T_x$ and Pt/Nb_2CT_x catalysts, respectively. The MXene supports enable dispersion of NPs without apparent agglomeration (Figures S3.2, S3.3).

The compositions of the NPs were first investigated by energy dispersive spectroscopy (EDS) elemental mapping. The signals of Pt and Ti or Nb overlap over all the NPs (Figures S3.4, S3.5), suggesting migrations of M to the Pt NPs. Aberration-corrected HAADF-STEM was utilized to further characterize the structures of Pt-Ti and Pt-Nb NPs. Figure 3.2a shows an image representative of the NPs supported by $Ti_3C_2T_x$ MXene. The NP in the center of the figure is viewed along the [111] zone axis, whereas another NP in the upper left corner is viewed along the [001] zone axis. Two different types of atoms can be clearly differentiated due to the Z-contrast in high angle annular dark field (HAADF) imaging. The bright dots are characteristic of heavier Pt atoms, while the dimmer ones correspond to Ti. Along the [111] axis of a NP, the projected unit cells are composed of periodic hexagonal arrays of Pt atoms that surround Ti atoms at the center of the hexagons (Figure 3.2b), which indicates a specific $L1_2$ type symmetry and is consistent with formation of the Cu_3Au type Pt_3Ti IMC (Figure 3.2c)[22]. The experimental HAADF-STEM image shows good agreement with the simulated (111) surface of $L1_2$ ordered Pt_3Ti nanostructures (inset of Figure 3.2b). The Pt/Ti ratio was estimated by EDS elemental mapping on a NP hanging over the vacuum to avoid the Ti signals from the $Ti_3C_2T_x$ MXene support and give a value of the molar

ratio of Pt to Ti equal to 3.55 (Figure S3.6), which is close to the theoretical ratio of Pt_3Ti alloy within error.

The ordered intermetallic structure of Pt-Nb NPs can also be directly observed (circled with dash lines) despite the small particle sizes (2.6 ± 0.7nm) (Figure 3.2d). The fcc structure is identified by two NPs viewed along [111] and [001] axis, respectively (Figure 3.2e, Figure S3.7). The inset of Figure 3.2e shows the fast Fourier transform (FFT) pattern of the NP viewed along [111] zone, where the signals of $(1\bar{1}0)$ and $(10\bar{1})$ supper-lattice are present. Since the unique super periods are present only in the structurally ordered intermetallic phase and are absent in the disordered alloy phase, ordering in the NP is confirmed. Moreover, the enlarged image of the NP (inset of Figure 3.2f) shows a dimmer Nb atom surrounded by six Pt atoms in a hexagonal pattern, again implying a local $L1_2$ ordering. The intermetallic phase, however, does not form over the whole NP. The distribution of the Pt-Nb intermetallic order in the NP is demonstrated by the contrast variation of the inverse fast Fourier transform (IFFT) image in Figure 3.2f. The IFFT pattern shows that the ordered Pt-Nb phase preferentially populates the edge of the NP versus the inner core. This is consistent with previous studies reporting that the diffusion of the second metallic species into the noble metal lattice (from the NP surface) played a pivotal role in the formations of intermetallic NPs[28-30].

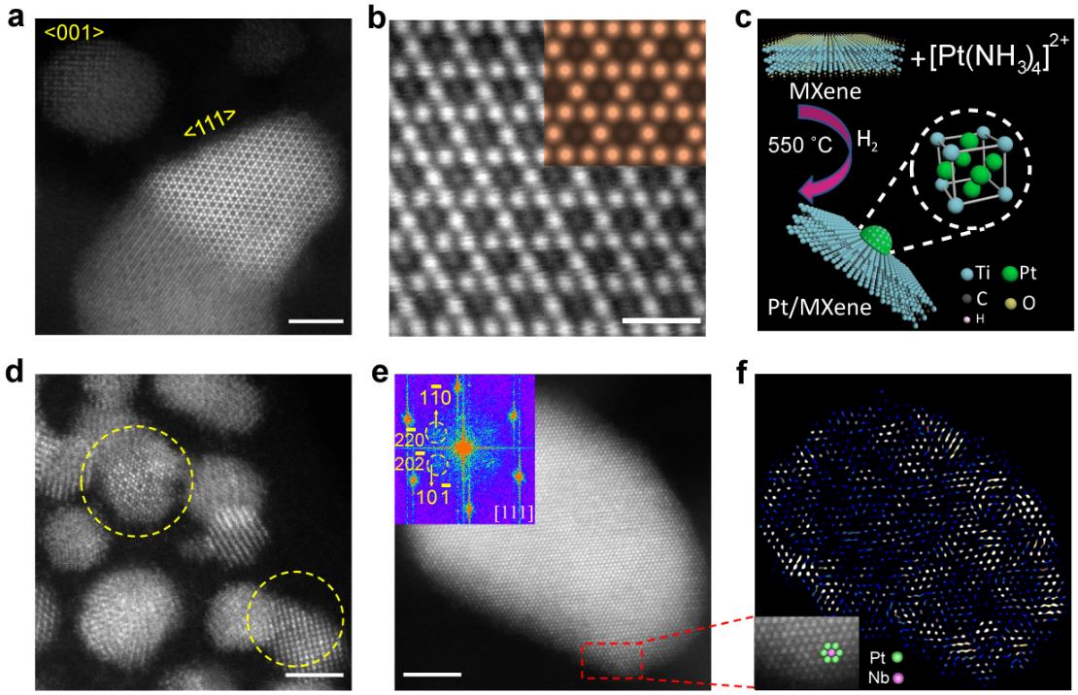

Figure 3.2 Microscopy characterizations of 1% Pt/MXene catalysts. (a) Representative HAADF-STEM image of 1% Pt/$Ti_3C_2T_x$ catalyst. (b) (111) surface of Pt_3Ti NP. Inset is a simulated STEM image of Pt_3Ti (111) surface. The simulated image is in good agreement with the experimental result. **(c)** Schematic illustration of RMSI in Pt/MXene catalysts and the structure of $L1_2$-ordered intermetallic Pt_3Ti. (d) Representative HAADF-STEM image of 1% Pt/Nb_2CT_x catalyst. (e) A Pt-Nb NP viewed along [111], inset is the FFT pattern of the NP. (f) IFFT pattern of the NP in Figure 3.2e, inset is an enlarged image showing the super lattice of the NP. Scale bars: **a, d, e** 2 nm, and **b** 500 pm.

To investigate the altered Pt chemical environment resulting from the RMSI between Pt and MXenes, the Pt/MXene catalysts were studied by *in situ* X-ray absorption spectroscopy (XAS). A Pt/SiO_2 catalyst with an average particle size of 1.8 ± 0.6 nm was also prepared as a reference (Figure S3.8). The EXAFS spectra of both *in situ* reduced catalysts (Figure 3.3a) show metal-metal scattering significantly different from the typical three-peak pattern characteristic of monometallic Pt NPs on SiO_2. For Pt/$Ti_3C_2T_x$, the central peak of the magnitude of Fourier transform EXAFS has a higher intensity due to the in-phase constructive interference between Pt-Ti and Pt-Pt scattering, while the opposite is observed on Pt/Nb_2CT_x because Pt-Nb and Pt-Pt are out-of-phase. Quantitative fitting (Figure S3.9, Table S3.1) of the EXAFS gives the following

average coordination numbers (CNs) and bond distances: 6.6 Pt-Pt bond and 3.4 Pt-Ti bond both at 2.75 Å for the Pt/$Ti_3C_2T_x$ catalyst and 6.7 Pt-Pt bond at 2.77 Å and 1.8 Pt-Nb bond at 2.75 Å for the Pt/Nb_2CT_x catalyst. The EXAFS of both catalysts confirms the presence of bimetallic NPs. For an ideal bulk $L1_2$ type Pt_3M intermetallic structure, the bond distances are the same for the Pt-Pt and Pt-M paths and the ratio of Pt-Pt CN over Pt-M CN is 2. Thus, the XAS results for Pt/$Ti_3C_2T_x$ indicate the formation of $L1_2$ type Pt_3M structures, which is concordant with those of STEM. For the Pt/Nb_2CT_x, the Pt-Pt/Pt-Nb CN ratio is much greater than 2 and their bond distances are slightly different, consistent with formation of partial/surface $L1_2$ ordering in the Pt-Nb NPs as observed by STEM. Together the HAADF-STEM and EXAFS indicate that RMSI occurs in these two MXene supported catalysts, leading to formations of IMCs with tunable compositions and structures. We note for comparison that Pt added similarly to bulk titanium carbide or niobium carbide surfaces did not produce IMCs (Figures S3.10, S3.11).

3.3.3 Electronic Structures of Pt/MXene Catalysts

In situ XANES at Pt L_{III} edge was conducted on the reduced catalysts to examine the energy of the unoccupied *d* states (Figure 3.3b). The XANES energies of the Pt/$Ti_3C_2T_x$ and Pt/Nb_2CT_x catalysts are 11564.6 eV and 11564.3 eV, respectively, both higher compared to that of monometallic Pt (11564.0 eV). The whitelines are slightly taller and narrower compared to that of Pt/SiO_2, corresponding to a change in the energy distribution of the 5*d* unoccupied states. Shifts in electronic band energy level were also detected by XPS (*In situ* reduced samples). In Figure 3.3c, the Pt $4f_{7/2}$ binding energies of Pt/$Ti_3C_2T_x$ and Pt/Nb_2CT_x are 71.3 eV and 71.6 eV respectively, which shift to higher values with respect to that of monometallic Pt (70.8 eV). These spectroscopic studies of fully reduced samples indicate that the formation of Pt_3M intermetallic NPs leads to

altered electronic structure of the Pt atoms and that the 5d states are shifted to higher energy in Pt/MXenes compared to Pt/SiO_2.

To better understand the modulated electronic structures of the Pt/MXene catalysts owing to the formations of IMCs, we carried out density functional theory (DFT) calculations of the projected density of states (DOS). Out of the two Pt/MXene catalysts, the Pt/$Ti_3C_2T_x$ catalyst contains full (instead of partial) IMC NPs with the exposure of representative (111) surface planes resolved by aberration-corrected STEM. Therefore, we employed slab models of Pt_3Ti(111) and Pt(111) surfaces for comparison. As shown in Figure 3.3d, the *d* band center of Pt(111) is located at -1.97 eV relative to the Fermi level, whereas that of Pt_3Ti(111) downshifts to -2.37 eV due to a strong Pt-Ti d-d orbital coupling. Similar shifts of d band center to a lower level were also reported in other Pt-M systems, where M is Co, Fe, Ni, Ce[31]. Additionally, ~ 1 eV above the Fermi level, the DOS calculation also shows an increased intensity for Pt_3Ti(111) (Figure 3.3d) compared to Pt(111), which is consistent with the *in situ* XANES results showing higher energy and intensity of the whiteline of the Pt/$Ti_3C_2T_x$ catalyst compared to Pt/SiO_2. A recent study combining DFT calculations and an emerging technique, *in situ* resonant inelastic X-ray Scattering (RIXS), reported that formation of IMCs leads to a downward shift of the *d* band center as well as an upward shift of the energy of the unoccupied 5*d* states[32], which agrees with our results.

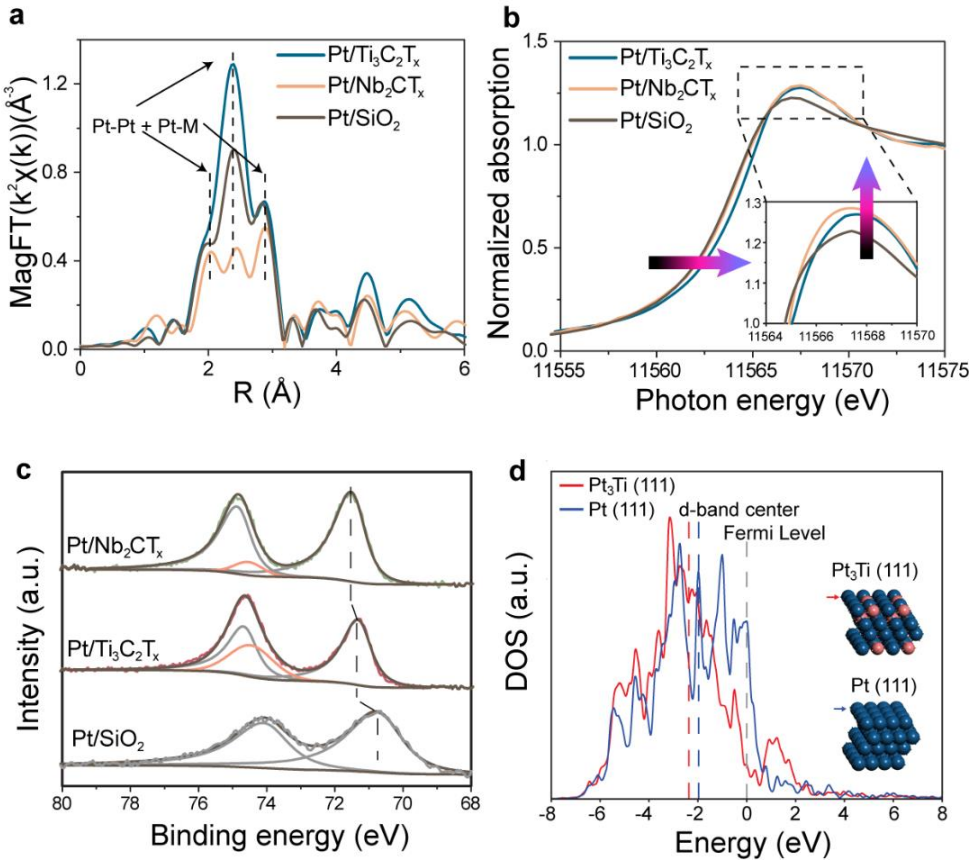

Figure 3.3 Spectroscopy characterization of Pt/MXenes catalysts. (a) Magnitude of the Fourier Transform of the k^2 weighted Pt L_{III} edge *in situ* EXAFS of the $Pt/Ti_3C_2T_x$ and Pt/Nb_2CT_x after reduction at 550°C in H_2 compared to Pt/SiO_2. (b) The Pt L_{III} edge *in situ* XANES spectra of the $Pt/Ti_3C_2T_x$ and Pt/Nb_2CT_x catalyst after reduction at 550°C in H_2 compared to Pt/SiO_2. (c) XPS spectra of $Pt/Ti_3C_2T_x$, Pt/Nb_2CT_x and Pt/SiO_2 reduced at 550°C by H_2 in a spectrometer side chamber and not exposed to air. (d) DFT calculated projected density of states (DOS) for the 5*d* orbitals of Pt in the top-layer Pt_3Ti (111) and Pt (111).

3.3.4 Catalytic Performance and Free Energy Calculations

According to d band chemisorption theory, shifts to lower energy of d band center will reduce the surface adsorption reactivity[33] and directly affect the chemistry of catalysts[34]. LADH reactions are sensitive to the energy level of d band electrons of the catalysts surface[21], thus were used as probes to evaluate effects of the *in situ* formation of Pt_3M intermetallic NPs on the catalytic performance. All the catalysts were pretreated and tested under the same conditions summarized in Methods. The product selectivity of different catalysts was compared between 0 and 20% light

alkane conversions. For both dehydrogenation of propane (Figure 3.4a) and isobutane (Figure S3.12), Pt/MXene catalysts are much more selective than Pt/SiO_2 at the same conversion. For example, when the conversion of propane is 15%, Pt/SiO_2 is 60% selective to propylene, while those of Pt/$Ti_3C_2T_x$ and Pt/Nb_2CT_x are ~ 95% and ~ 90%, respectively (Figure 3.4a). Though intermetallic catalysts have larger particle size compared to the reference monometallic Pt catalyst, the improvement in their catalytic performance can be attributed to the formation of intermetallic structure rather than a size effect since larger particles have been reported to give lower selectivity[35,36]. Similar improvements were also observed for isobutane dehydrogenation (Figure S3.12). For all the catalysts, the selectivity of dehydrogenation is lower at higher conversion due to the hydrogenolysis side reaction that requires hydrogen. The decrease in selectivity under increasing conversion is reduced on the Pt/$Ti_3C_2T_x$ and Pt/Nb_2CT_x catalysts, indicating that the effect of side reactions is less prominent on the intermetallic NPs. The TORs were calculated using the reaction rate per gram of Pt measured under differential conditions and catalyst dispersion estimated from the average particles sizes. For propane dehydrogenation (PDH), the TORs were 0.12 s^{-1}, 0.09 s^{-1} and 0.08 s^{-1} for Pt/SiO_2, Pt/Nb_2CT_x and Pt/$Ti_3C_2T_x$, respectively. The TORs for isobutane dehydrogenation followed a similar trend and were 0.09 s^{-1}, 0.06 s^{-1} and 0.06 s^{-1} for Pt/SiO_2, Pt/Nb_2CT_x and Pt/$Ti_3C_2T_x$. These values are similar to the TORs reported for typical LADH catalysts[21]. The evolution of performance with time on-stream for IMC catalysts are also consistent with the monometallic Pt catalyst (Figure S3.13) as well as previous literature, due to slow deposition of coke[21]. The used Pt/Nb_2CT_x and Pt/$Ti_3C_2T_x$ were further characterized by HAADF-STEM to check the stability of the IMCs. The structures of Pt_3Ti and Pt_3Nb are preserved in the spent catalysts (Figures S3.14, S3.15), indicating that the IMCs NPs were stable under the LADH reaction conditions.

To understand the high olefin selectivity of the intermetallic catalysts for PDH reaction, energy profiles of PDH reaction and possible side reactions were studied by DFT calculations. Snapshots of structures of reaction intermediates and transition states were illustrated in Figure 3.4b, with the free energies of the relevant reaction pathways on Pt(111) and Pt_3Ti(111) surfaces calculated and shown in Figure 3.4c. PDH follows a step-wise C-H bond breaking process[37], which starts with dissociative adsorption of propane forming surface alkyl species (intermediate 2), followed by the scission of a secondary C-H bond generating adsorbed olefins (intermediate 4). Our DFT results show that the free energy changes and barriers of the first two steps on the Pt_3Ti(111) are higher than those on pure Pt(111), indicating weakened surface adsorption activity of the intermetallic phase consistent with the shifts in the 5*d* DOS indicated by DFT, XANES and XPS. In the following steps, the adsorbed olefins may undergo desorption, further (deep) dehydrogenation (intermediate 7) or C-C breaking (intermediate 11) processes. The latter two steps are believed to generate the precursors leading to side reactions, i.e., coking and hydrogenolysis[38].

On Pt(111), the free energy barrier for dehydrogenation of C_3H_6* to C_3H_5* is 0.19 eV lower than that of propylene desorption, indicating that the deep dehydrogenation is more favorable on Pt(111) surface. In contrast, on Pt_3Ti(111) the C_3H_6* desorption is more favored by 0.1 eV in barrier than further dehydrogenation. For direct comparison, the barrier of C_3H_6* desorption on Pt_3Ti(111) (0.66 eV) is 0.25 eV lower than that on Pt(111) (0.91 eV). In addition, the free energy change of C_3H_6* desorption on Pt_3Ti(111) (-1.17 eV) is 0.54 eV more favorable than that on Pt(111) (-0.63 eV). Overall, the introduction of Ti lowers the desorption barrier of C_3H_6* to the gas phase (0.66 eV of Pt_3Ti(111) vs. 0.91 eV of Pt(111)) and increases the energy barrier for deep dehydrogenation. On both surfaces, C-C cracking of dehydrogenated reaction intermediates, e.g. C_3H_6*, C_3H_5*, and C_3H_4*, requires much higher activation energies and thus are less competitive.

Nevertheless, on $Pt_3Ti(111)$ the C-C cracking steps (intermediates 11, 13 and 15) are all endergonic and hence are hindered compared with Pt(111) where C_3H_5* and C_3H_4* cracking are exergonic and much more favorable. These results rationalize the observed higher selectivity toward propylene for PDH by Pt_3Ti intermetallic NPs compared to pure Pt.

Our experimental results and DFT calculations show that the Pt_3Ti intermetallic phase has a lower *d* band center compared with that of monometallic Pt, which results in weaker adsorption of light hydrocarbon species and changes of the relative free energy and barriers of the reaction steps during dehydrogenation and side reactions. Lowering of the olefin desorption barrier to below that of deep dehydrogenation and C-C breaking contributes to the high catalyst selectivity. The same type of calculations were not conducted for the Pt/Nb_2CT_x catalyst due to its relatively less well-defined structure. However, similar catalyst electronic structure compared to $Pt/Ti_3C_2T_x$ can be expected according to the *in-situ* X-ray spectroscopy results. The adsorption properties, and reaction energetics are, therefore, also expected to be similar. The fact that the Pt/Nb_2CT_x catalyst has a slightly lower selectivity compared to $Pt/Ti_3C_2T_x$ is likely due to the extent of the IMCs formation, i.e., full verses surface IMCs, and differences in electronic effects. These additional subtle catalytic differences demonstrate that the chemical properties of the catalysts are tunable using different MXene materials as the RMSI-active supports.

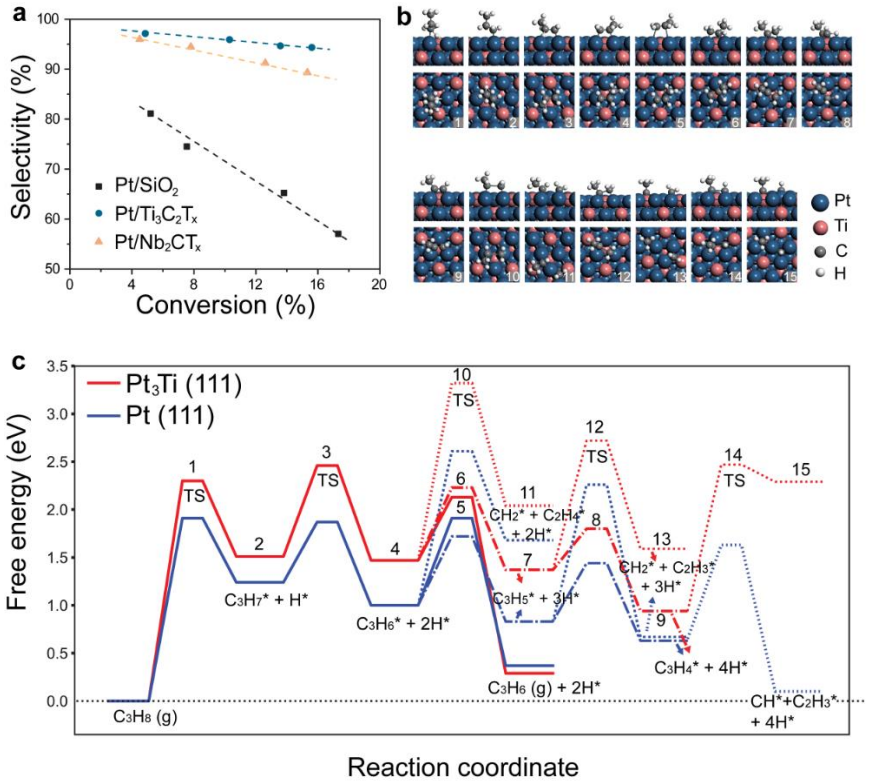

Figure 3.4 Catalytic performance and DFT calculation of Pt/MXene catalysts. (a) Plots of conversion *vs.* selectivity for propane dehydrogenation measured in 200 cm^3 min^{-1} of 2.5 % C_3H_8, 2.5 % H_2 balanced in N_2 at 1.5 atm and 550 °C for Pt/$Ti_3C_2T_x$, Pt/Nb_2CT_x and Pt/SiO_2 catalyst. (b) Snapshots of optimized structures as numbered in (c) from side and top view angles (H* is not shown). (c) DFT-calculated free energy diagram of relevant (side-)reaction steps in propane dehydrogenation on Pt_3Ti (111) and Pt (111) surfaces. The dotted lines denote the C-C cracking reactions of C_3H_6*, C_3H_5*, and C_3H_4*, generating CH_2* + C_2H_4*, CH_2* + C_2H_3*, and CH* + C_2H_3*, respectively. The dash-dot lines denote the further dehydrogenation of C_3H_6* to C_3H_5*, and C_3H_5* to C_3H_4*.

In summary, this work demonstrates two IMC catalysts selective for LADH achieved by RMSI between Pt NPs and $Ti_3C_2T_x$ and Nb_2CT_x MXenes. The intermetallic surface is imaged by atomic resolution HAADF-STEM and its high catalytic selectivity is rationalized by DFT calculations. With MXenes as catalyst supports and through their active interactions with metal NPs, there is an opportunity to explore many new compositions for heterogeneous catalysis in industrial gas-phase reactions as well as electrochemical conversion, with the possibility that the

chemical and electronic properties of the resulting catalysts can be tuned over a wider range than what is currently possible using conventional catalyst supports.

3.4 Methods

3.4.1 Synthesis of Ti_3AlC_2 and Nb_2AlC

The Ti_3AlC_2 powder was synthesized by spark plasma sintering (SPS) of TiH_2/Al/TiC. Commercial powders of titanium (II) hydride, aluminum and titanium (IV) carbide were mixed in a molar ratio of TiH_2/Al/TiC = 1:1:1.8 in a graphite die coated with boron nitride (BN). Excess Al and less than a full equivalent of TiC were added because a small portion of Al will be lost during high-temperature processing, and carbon deficiencies exist in most Al-containing MAX phases. Then, the material was loaded in a Fuji-211lx SPS system and sintered at 1350°C under 30 MPa for one hour. The resulting Ti_3AlC_2 was then pulverized and sieved through a 325-mesh screen.

The Nb_2AlC powder was synthesized by spark plasma sintering (SPS) of Nb/Al/graphite mixtures. Commercial powders of niobium, graphite and aluminum were mixed in a molar ratio of Nb:Al:C = 2:1.4:0.9 in a graphite die coated with boron nitride (BN). Then, the material was loaded in a Fuji-211lx SPS system and sintered at 1500°C under 30 MPa for one hour. The resulting Nb_2AlC was then pulverized and sieved through a 400-mesh screen.

3.4.2 Preparation of $Ti_3C_2T_x$ MXene and Nb_2CT_x MXene

Approximately 1 g of the prepared Ti_3AlC_2 powder was immersed in 10 mL of 50% aqueous hydrofluoric acid solution stirred with a magnetic bar for approximately 1 days at 35°C. The resulting MXene suspension was repeatedly washed with deionized water (DI) and centrifuged until the pH reached ~ 5. The final MXene was dried under vacuum at room temperature and stored in a glove box until usage.

Approximately 1 g of the prepared Nb_2AlC powder was immersed in 10 mL of 50% aqueous hydrofluoric acid (HF) solution stirred with a magnetic bar for approximately 3 days at

55°C. The resulting MXene suspension was repeatedly washed with deionized water (DI) and centrifuged until the pH reached ~ 5. The final MXene was dried under vacuum at room temperature and stored in a glove box until usage.

3.4.3 Catalyst Preparation.

A monometallic Pt catalyst (2 wt. % Pt supported on Davisil 636 silica gel from Sigma-Aldrich) was synthesized using the incipient wetness impregnation (IWI) method. 0.20 g of tetraammineplatinum nitrate was dissolved in 3 mL of H_2O. ~30% ammonium hydroxide solution (NH_4OH, 28% NH_3 in H_2O, ≥99.99%, Sigma-Aldrich) was then added to the solution until the pH reached 11. The obtained Pt precursor solution was added dropwise to 5 g of silica and stirred. After drying overnight under vacuum, the sample was calcined at 225 °C for 3 h and reduced at 550 °C in 5 % H_2/N_2 for 30 minutes.

Pt supported on $Ti_3C_2T_x$ and on Nb_2CT_x were prepared via a similar method. 0.20 g of tetraammineplatinum nitrate ($Pt(NH_3)_4(NO_3)_2$) were dissolved in 0.5 mL of deionized H_2O to prepare 1 mol L^{-1} Pt precursor solution. 0.05 mL of such solution was impregnated on fresh $Ti_3C_2T_x$ and Nb_2CT_x MXenes, respectively, prior to dying overnight under vacuum. The obtained catalysts were reduced at 550°C in 5% H_2/N_2 for at least 0.5 h before each catalytic test or characterization.

Pt loadings of the $Pt/Ti_3C_2T_x$ and Pt/Nb_2CT_x catalysts were determined by atomic absorption spectroscopy (AAS). Specifically, the catalyst was digested by aqua regia in a Nalgene® amber polyethylene bottle for 3 days and the solution was then diluted to desired concentration for the AAS measurement.

3.4.4 Light Alkane Dehydrogenation (LADH) Kinetics

Light alkane dehydrogenation kinetics measurements were carried out in a quartz fixed-bed reactor with 3/8-inch ID. Catalysts around 0.02-0.15 g were diluted using pure SiO_2 to achieve

a total weight of 1.00 g for testing the performance. Reaction temperature was measured using a thermocouple inserted in a stainless-steel thermocouple well locating at the bottom center of the catalyst bed. Agilent 7890A gas chromatograph system quipped with a flame ionization detector (FID) was employed for analyzing the products. Prior to each measurement, the fresh catalysts were reduced by 5% H_2/N_2 (50 cm^3 min^{-1}) for 30 minutes at 550 °C with the temperature ramping rate of 15 °C min^{-1}. Propane dehydrogenation was tested under a reaction atmosphere of 2.5% C_3H_8, 2.5% H_2 balanced with N_2. The total flow rate of the reactant mixture was 200 cm^3 min^{-1}. After 2 minutes on-stream, the catalyst selectivity was compared below 20% conversion at 550 °C and turnover rates (TORs, per surface Pt site) were measured under differential condition at conversion below 5%. For iso-butane dehydrogenation, a reaction atmosphere of 2.5 % C_3H_8, 2.5 % H_2 balanced in N_2 with a total flow rate of 100 cm^3 min^{-1} was used. Catalyst performance was measured at 450 °C.

3.5 References

1 Bell, A. T. The impact of nanoscience on heterogeneous catalysis. *Science* **299**, 1688-1691 (2003).

2 Shekhar, M. *et al.* Size and support effects for the water–gas shift catalysis over gold nanoparticles supported on model Al_2O_3 and TiO_2. *J. Am. Chem. Soc.* **134**, 4700-4708 (2012).

3 Huang, X. *et al.* High-performance transition metal-doped Pt_3Ni octahedra for oxygen reduction reaction. *Science* **348**, 1230-1234 (2015).

4 Matsubu, J. C. *et al.* Adsorbate-mediated strong metal-support interactions in oxide-supported Rh catalysts. *Nat. Chem.* **9**, 120 (2017).

5 Kattel, S., Liu, P. & Chen, J. G. Tuning Selectivity of CO_2 Hydrogenation Reactions at the Metal/Oxide Interface. *J. Am. Chem. Soc.* **139**, 9739-9754 (2017).

6 Zhao, Z.-J. *et al.* Importance of metal-oxide interfaces in heterogeneous catalysis: A combined DFT, microkinetic, and experimental study of water-gas shift on Au/MgO. *J. Catal.* **345**, 157-169 (2017).

7 Mehta, P., Greeley, J., Delgass, W. N. & Schneider, W. F. Adsorption Energy Correlations at the Metal-Support Boundary. *ACS Catal.* **7**, 4707-4715 (2017).

8 Li, W.-Z. *et al.* Stable platinum nanoparticles on specific $MgAl_2O_4$ spinel facets at high temperatures in oxidizing atmospheres. *Nat. Commun.* **4**, 2481 (2013).

9 Rao, R. G. *et al.* Interfacial charge distributions in carbon-supported palladium catalysts. *Nat. Commun.* **8**, 340 (2017).

10 Cargnello, M. et al. Control of Metal Nanocrystal Size Reveals Metal-Support Interface Role for Ceria Catalysts. Science **341**, 771–773 (2013).

11 Willinger, M. G. *et al.* A case of strong metal-support interactions: combining advanced microscopy and model systems to elucidate the atomic structure of interfaces. *Angew. Chem. Int. Ed.* **53**, 5998-6001 (2014).

12 Tauster, S., Fung, S. & Garten, R. L. Strong metal-support interactions. Group 8 noble metals supported on titanium dioxide. *J. Am. Chem. Soc.* **100**, 170-175 (1978).

13 Tauster, S., Fung, S., Baker, R. & Horsley, J. Strong interactions in supported-metal catalysts. *Science* **211**, 1121-1125 (1981).

14 Naguib, M. *et al.* Two-dimensional nanocrystals produced by exfoliation of Ti_3AlC_2. *Adv. Mater.* **23**, 4248-4253 (2011).

15 Naguib, M., Mochalin, V. N., Barsoum, M. W. & Gogotsi, Y. 25th anniversary article: MXenes: a new family of two-dimensional materials. *Adv. Mater.* **26**, 992-1005 (2014).

16 Li, Z. *et al.* Reactive metal-support interactions at moderate temperature in two-dimensional niobium-carbide-supported platinum catalysts. *Nat. Catal.*, **1**, 349-355 (2018).

17 Penner, S. & Armbrüster, M. Formation of intermetallic compounds by reactive metal–support interaction: a frequently encountered phenomenon in catalysis. *ChemCatChem* **7**, 374-392 (2015).

18 Bernal, S. *et al.* Nanostructural Evolution of a Pt/CeO_2 catalyst reduced at Increasing temperatures (473–1223 K): a HREM study. *J. Catal.* **169**, 510-515 (1997).

19 Beard, B. C. & Ross, P. N. Platinum-titanium alloy formation from high-temperature reduction of a titania-impregnated platinum catalyst: implications for strong metal-support interaction. *J. Phys. Chem.* **90**, 6811-6817 (1986).

20 Sabnis, K. D. *et al.* Water-gas shift catalysis over transition metals supported on molybdenum carbide. *J. Catal.* **331**, 162-171 (2015).

21 Sattler, J. J., Ruiz-Martinez, J., Santillan-Jimenez, E. & Weckhuysen, B. M. Catalytic dehydrogenation of light alkanes on metals and metal oxides. *Chem. Rev.* **114**, 10613-10653 (2014).

22 Cui, Z. *et al.* Synthesis of structurally ordered Pt_3Ti and Pt_3V nanoparticles as methanol oxidation catalysts. *J. Am. Chem. Soc.* **136**, 10206-10209 (2014).

23 Saravanan, G. *et al.* Pt_3Ti nanoparticles: fine dispersion on SiO_2 supports, enhanced catalytic CO oxidation, and chemical stability at elevated temperatures. *Langmuir* **26**, 11446-11451 (2010).

24 Naguib, M. *et al.* New two-dimensional niobium and vanadium carbides as promising materials for Li-ion batteries. *J. Am. Chem. Soc.* **135**, 15966-15969 (2013).

25 Mashtalir, O. *et al.* Intercalation and delamination of layered carbides and carbonitrides. *Nat. Commun.* **4**, 1716 (2013).

26 Lin, H., Gao, S., Dai, C., Chen, Y. & Shi, J. A Two-dimensional biodegradable niobium carbide (MXene) for photothermal tumor eradication in NIR-I and NIR-II biowindows. *J. Am. Chem. Soc.* **139**, 16235-16247 (2017).

27 Nawaz, Z. Light alkane dehydrogenation to light olefin technologies: A comprehensive review. *Rev. Chem. Eng.* **31**, 413-436 (2015).

28 Gallagher, J. R. *et al.* Structural evolution of an intermetallic Pd-Zn catalyst selective for propane dehydrogenation. *Phys.Chem. Chem. Phys.* **17**, 28144-28153 (2015).

29 Wu, Z. *et al.* Pd-In intermetallic alloy nanoparticles: highly selective ethane dehydrogenation catalysts. *Catal. Sci. & Technol.* **6**, 6965-6976 (2016).

30 Wegener, E. C. *et al.* Structure and reactivity of Pt-In intermetallic alloy nanoparticles: Highly selective catalysts for ethane dehydrogenation. *Catal.Today* **299**, 146-153 (2017).

31 Hammer, B., Morikawa, Y. & Nørskov, J. K. CO chemisorption at metal surfaces and overlayers. *Phys. Rev. Lett.* **76**, 2141 (1996).

32 Cybulskis, V. J. *et al.* Zinc Promotion of platinum for catalytic light alkane dehydrogenation: insights into geometric and electronic effects. *ACS Catal.* **7**, 4173-4181 (2017).

33 Hammer, B. & Nørskov, J. K. Theoretical surface science and catalysis-calculations and concepts. *Adv. Catal.* **45**, 71-129 (2000).

34 Yu, W., Porosoff, M. D. & Chen, J. G. Review of Pt-based bimetallic catalysis: from model surfaces to supported catalysts. *Chem. Rev.* **112**, 5780-5817 (2012).

35 Cortright, R. & Dumesic, J. Microcalorimetric, spectroscopic, and kinetic studies of silica supported Pt and Pt/Sn catalysts for isobutane dehydrogenation. *J. Catal.* **148**, 771-778 (1994).

36 Yang, C. *et al.* Promotion of Pd nanoparticles by Fe and formation of a Pd_3Fe intermetallic alloy for propane dehydrogenation. *Catal. Today*, **323**, 123-128 (2019).

37 Yang, M.-L., Zhu, Y.-A., Zhou, X.-G., Sui, Z.-J. & Chen, D. First-principles calculations of propane dehydrogenation over PtSn catalysts. *Acs Catal.* **2**, 1247-1258 (2012).

38 Yang, M.-L. *et al.* DFT study of propane dehydrogenation on Pt catalyst: effects of step sites. *Phys.Chem. Chem. Phys.* **13**, 3257-3267 (2011).

3.6 Acknowledgments

Y. W. appreciates the support from the Herbert L. Stiles Professorship and Iowa State University College of Engineering exploratory research projects. Z.W., and J.T.M., were supported in part by the National Science Foundation under Cooperative Agreement No. EEC-1647722, and W.N.D. by the Davidson School of Chemical Engineering at Purdue. The XPS data was obtained at the Surface Analysis Facility of the Birck Nanotechnology Center of Purdue University. Use of the Advanced Photon Source was supported by the U.S. Department of Energy, Office of Basic Energy Sciences, under contract no. DE-AC02-06CH11357. MRCAT operations, beamline 10-BM, are supported by the Department of Energy and the MRCAT member institutions. L.Y. and H.X. acknowledge financial support from the American Chemical Society Petroleum Research Fund (ACS PRF 55581-DNI5) and the NSF CBET Catalysis Program (CBET-1604984). The computational resource used in this work is provided by the advanced research computing at Virginia Polytechnic Institute and State University.

3.7 Author Contributions

Z.L. and Z.W. conceived the idea and designed the present work. H.X., L.Y., and J. L. conducted DFT calculations. Z.L., Z.W., Y.C., N.L., and Z.Q. synthesized the catalysts and performed the catalytic evaluation. C.M., Z.W., J.M., carried out the spectroscopic characterizations. L.Z., T.M., Z.L., B.X., and E.Shi. performed the detailed microscopic experiments. Y.W., J.M., H.X., and W.N.D. supervised the research.

3.8 Supporting Methods

3.8.1 Aberration-Corrected Scanning Transmission Electron Microscopy

Aberration-corrected imaging and EDS were conducted on a Titan Themis 300 probe corrected TEM equipped with a SuperX EDX detector at Sensitive Instrument Facility (SIF) of Ames Lab. Samples were ground to fine powders and dispersed in isopropyl alcohol. Three drops of the solution or supernatant were added onto an ultrathin carbon lacey film-Au (or Cu) TEM grid (TedPella) and dried naturally. STEM images were taken using the high angle annular dark field (HAADF) detector at 200 kV and particle size was counted using the Gatan Digital Micrograph. A minimum of 100 particles were counted to obtain the size distribution for each catalyst.

3.8.2 X-ray Photoelectron Spectroscopy (XPS)

XPS data was obtained using a Kratos Axis Ultra DLD spectrometer with monochromic Al Kα radiation (1486.6 eV) at pass energy of 20 and 160 eV for high-resolution and survey spectra, respectively. A commercial Kratos charge neutralizer was used to avoid non-homogeneous electric charging of non-conducting powders and to achieve better resolution. The resolution measured as full width at half maximum of the curve fitted C 1s peak was approximately 1 eV. Binding energy (BE) values refer to the Fermi edge and the energy scale was calibrated using Au $4f_{7/2}$ at 84.0 eV and Cu $2p_{3/2}$ at 932.67 eV. XPS data were analyzed with CasaXPS software version 2313 Dev64. Curve-fitting was performed following a linear or Shirley background subtraction using Gaussian/Lorentzian peak shapes (GL and LF). The atomic concentrations of the elements in the near-surface region were estimated considering the corresponding Scofield atomic sensitivity factors and inelastic mean free path (IMFP) of photoelectrons using standard procedures in the CasaXPS software. For XPS measurements, sample treatments were performed in a reaction cell (≈30 cm^3) connected to the XPS spectrometer and all samples were reduced in

5% H_2 for at least 30 minutes. Then the samples were moved between the reaction cell and the analysis chamber under ultrahigh vacuum (UHV) conditions without exposure to air.

3.8.3 In situ X-ray Absorption Spectroscopy (XAS)

X-ray absorption measurements were acquired at the Ti K edge (4.9664 keV), Nb K edge (18.9856 keV) and Pt L_{III} edge (11.5640 keV) on the insertion device beam line of the Materials Research Collaborative Access Team (MRCAT) at the Sector 10 in the Advanced Photon Source, Argonne National Laboratory. The ionization chambers were optimized for the maximum current with linear response with 10% absorption in the incident ion chamber and 70% absorption in the transmission detector. A third detector in series simultaneously collected a Ti, Nb or Pt metal foil reference spectrum with each measurement for energy calibration. Solid samples were pressed into a cylindrical sample holder consisting of six wells, forming a self-supporting wafer. The sample holder was placed in a quartz reactor tube sealed with Kapton windows by two Ultra-Torr fittings through which gas could be flowed.

$Ti_3C_2T_x$ and reference compounds TiO_2, Ti foil and TiC (Sigma-Aldrich) were scanned in air. Fresh Pt on $Ti_3C_2T_x$ and Nb_2CT_x catalysts were reduced in 3 % H_2/He with a flow rate of 50 cm^3/min at 550 ^oC for at least 30 min, then cooled to room temperature and flushed with He or air before they were scanned. The fits of the EXAFS were evaluated using Artemis software (Demeter 0.9.26). The EXAFS coordination parameters were obtained by a least-squares fit in R-space of the k^2-weighted Fourier transform data from 3.0 to 11.0 $Å^{-1}$ and the first shell fits of the magnitude and imaginary parts were performed between 1.0 and 2.2 Å.

3.8.4 Intercalation and Delaminated of $Ti_3C_2T_x$ and Nb_2CT_x

Around 0.1 g of the dried $Ti_3C_2T_x$ or Nb_2CT_x MXene powders was dispersed into ~5ml dimethyl sulfoxide and tetrapropylammonium hydroxide. The solutions were then stirred at ambient temperature for 24 hours. The resulting solutions were centrifuged @ 8900 rpm to

separate the precipitates from the solvents and deionized water was added to the powders in a weight ratio of MXene to water of 1:200. Then, the suspensions were sonicated in a bath for 0.5 hour and the supernatant was collected for further TEM characterizations. Finally, the MXene powders were washed twice using ethanol to completely remove the organic intercalants and collected by centrifugation and dried in vacuum at room temperature overnight.

3.8.5 Computational Methods

Density functional theory (DFT) calculations were performed using the plane-wave based PWSCF (Quantum-ESPRESSO) program and the Atomic Simulation Environment (ASE)[1]. The ultrasoft Vanderbilt pseudopotential method with Perdew-Burke-Ernzerhof (PBE) exchange-correlation functional was adopted[2-4]. A plane-wave cutoff energy of 500 eV was used. The (111) slabs were built with 4 atomic layers in hexagonal 4×4 supercells with the bottom two layers fixed during structural relaxation. The Monkhorst-Pack scheme was used for sampling the Brillouin zone and k-point grids of 2×2×1 were selected[5]. The vacuum thickness was set to 15 Å in all slab calculations and the dipole correction was applied to decouple the interaction between slabs. During structural optimizations, the residual force between atoms was converged to a value below 0.02 eV/Å. The free energies of reaction intermediates and transition states on the surface were calculated as $E_{total} + ZPE + H_{vib} - TS_{vib}$, where E_{total} is DFT calculated total energy, ZPE is the zero point energy, T is temperature, H_{vib} and S_{vib} are the enthalpy and entropy parts from non-imaginary vibrations derived in a harmonic approximation to the potential. The free energies of gas phase molecules were calculated as $E_{total} + ZPE + H - TS$, where H is the enthalpy and S is the entropy. Transition states were calculated using the Fixed Bond Length method as implemented in the ASE.

3.9 Supplementary Figures

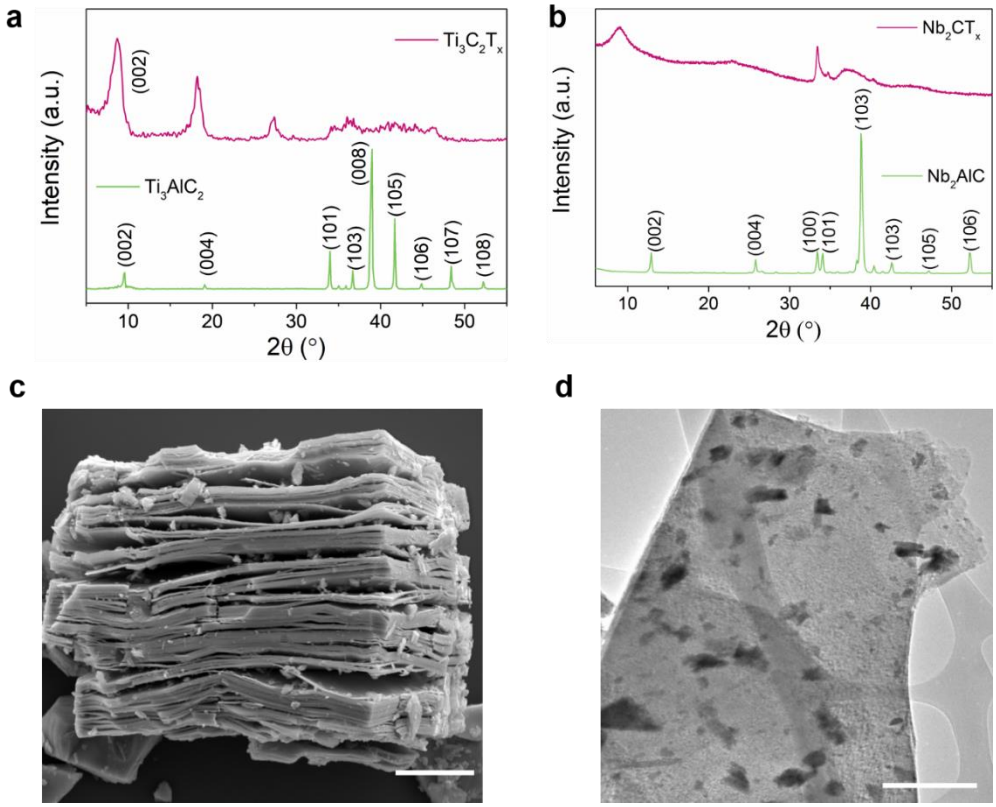

Figure S3.1 (a) and (b) XRD patterns of Ti_3AlC_2, $Ti_3C_2T_x$ MXene, Nb_2AlC and Nb_2CT_x MXene. The downshifts of (002) peaks to lower angles indicate that the MAX phases have converted to the corresponding MXenes. (c) SEM image of Nb_2CT_x MXenes. The MXene show the typical ‘‘accordion’’ morphology, confirming the exfoliation of individual grain along the basal planes. (d) Bright field TEM image of Nb_2CT_x MXene. Scale bars are 3μm.

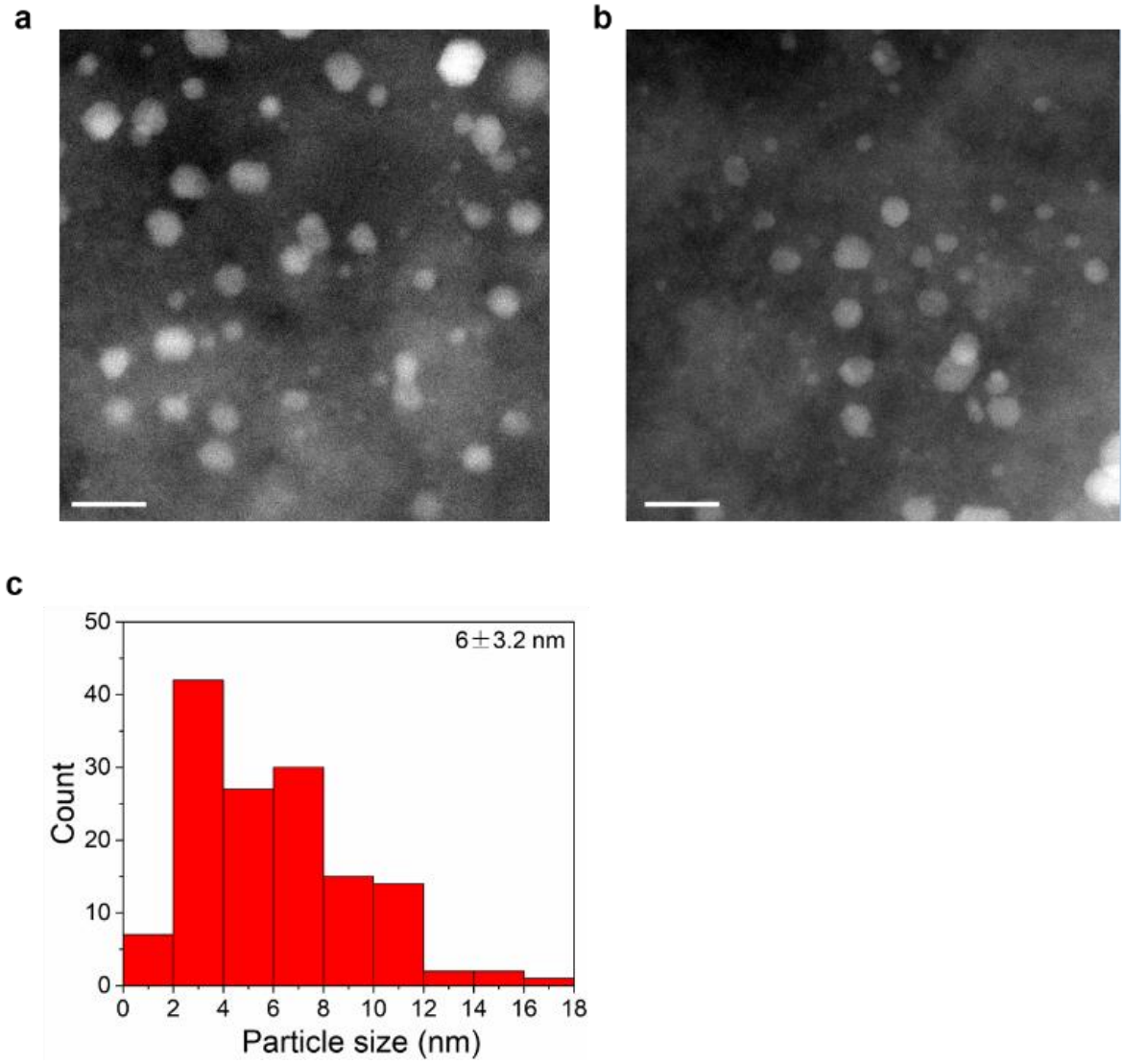

Figure S3.2 (a) and (b) Annular dark-field STEM overview image of $Pt/Ti_3C_2T_x$ reduced by 5% H_2/N_2 at 550 °C. Scale bars correspond to 20 nm. (c) Particle size distribution of more than 100 particles. The average particle size is 6 nm.

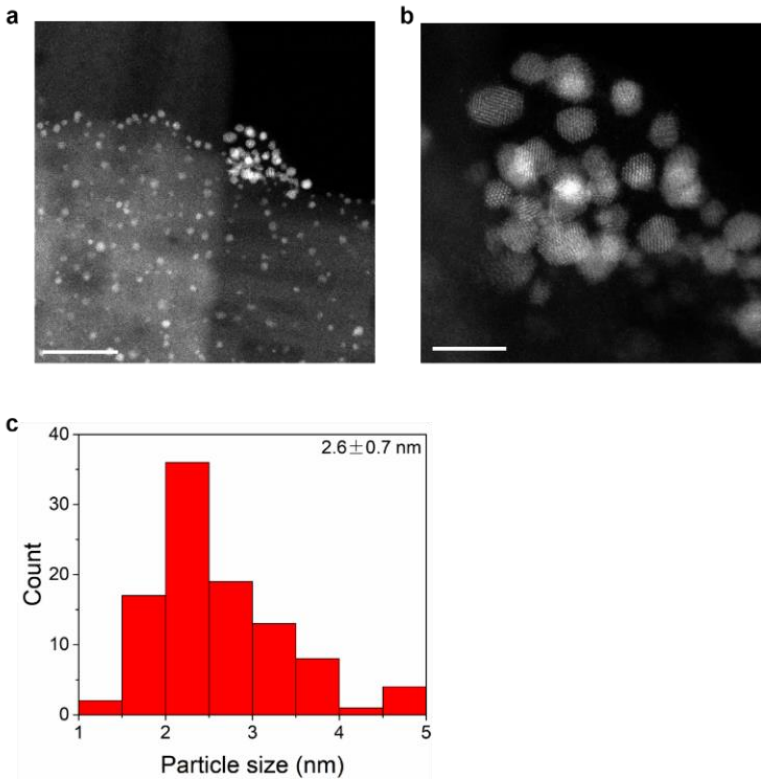

Figure S3.3 (a) and (b) Annular dark-field STEM overview image of Pt/Nb_2CT_x reduced by 5% H_2/N_2 at 550 °C. Scale bars correspond to 20 nm and 5 nm, respectively. **(c)** Particle size distribution of more than 100 particles. The average particle size is 2.6 nm.

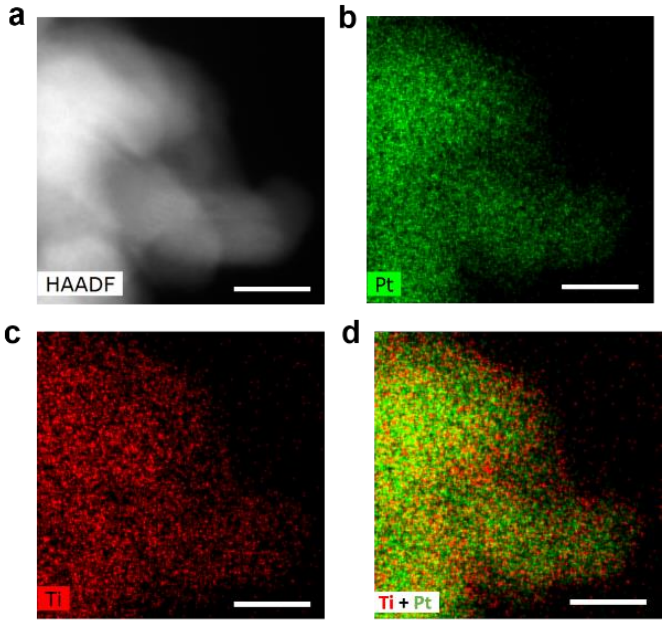

Figure S3.4 (a) HAADF-STEM image of $Pt/Ti_3C_2T_x$. (b-d) Elemental mappings of Pt (b), Ti (c), and Ti versus Pt (d). Scale bars are 4 nm.

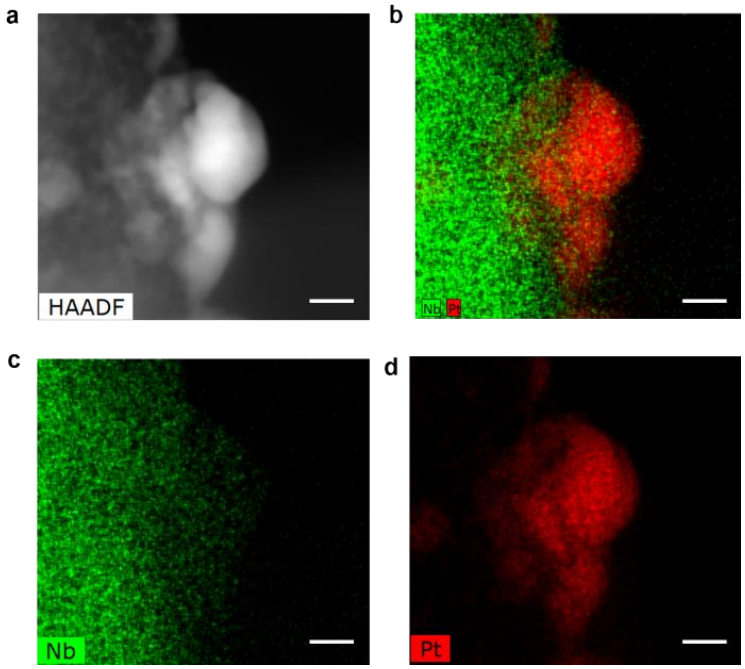

Figure S3.5 (a) HAADF-STEM image of Pt/Nb_2CT_x. (b-d) Elemental mappings of Nb versus Pt (b), Nb (c), and Pt (d). Scale bar, 5 nm.

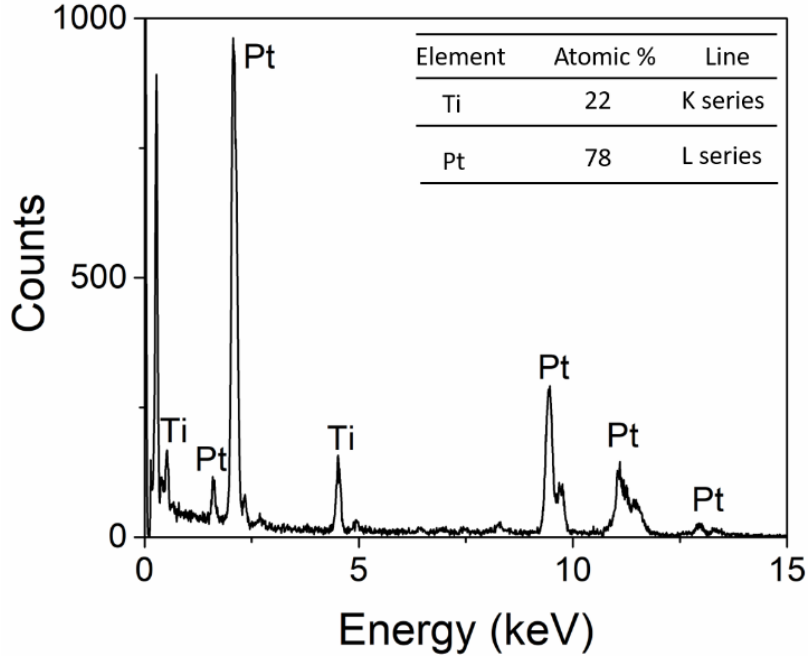

Figure S3.6 Energy dispersive X-ray spectroscopy (EDS) signal counts of Pt-Ti alloy shown in Figure S3.4. The inset shows the atomic percentage of Ti and Pt. The Pt:Ti molar ratio is 3.55.

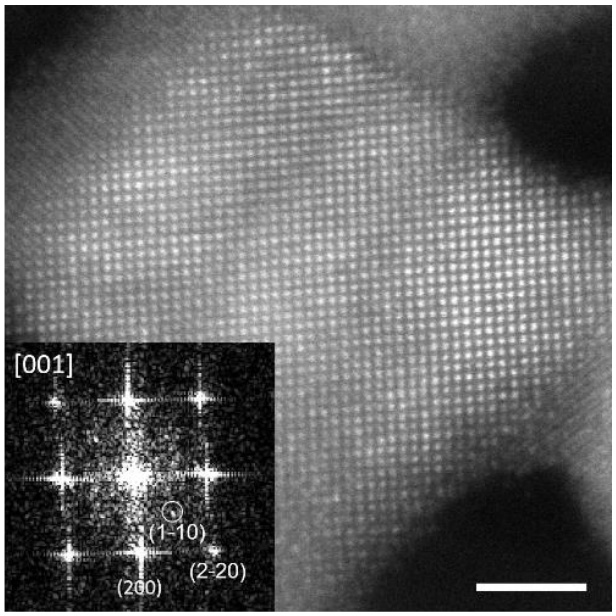

Figure S3.7 A Pt-Nb NP viewed along [001]. Inset is the FFT pattern of the NP, which shows the signals of the (1-10) superlattices. The scale bar corresponds to 2 nm.

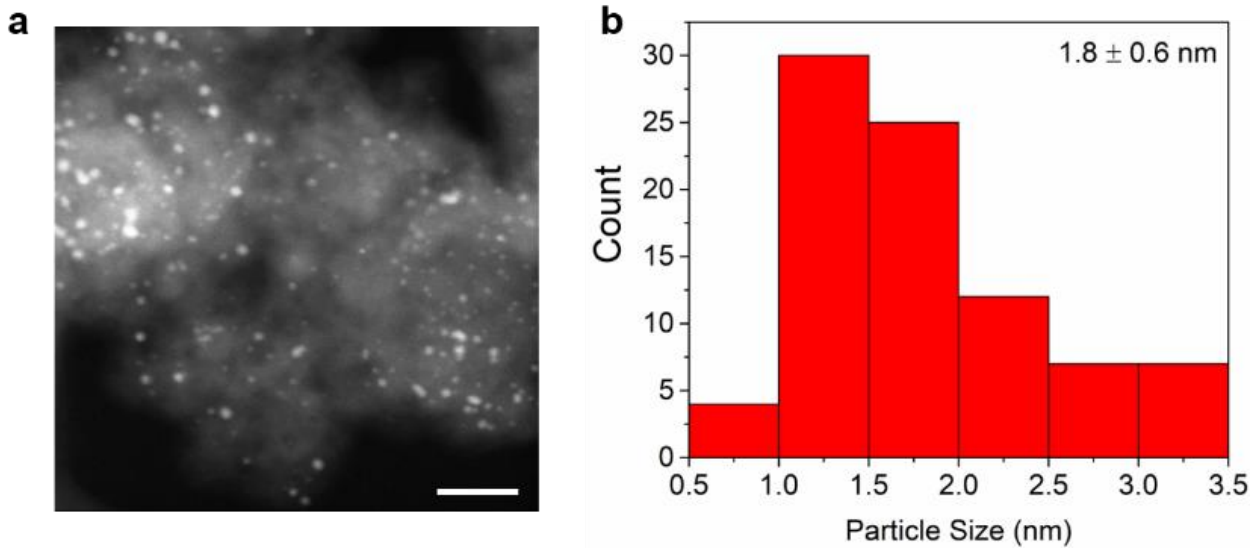

Figure S3.8 (a) STEM overview image of Pt/SiO_2 reduced by 5% H_2/N_2 at 550 °C. The scale bar corresponds to 20 nm. **(b)** Particle size distribution of Pt/SiO_2 (Average particle size: 1.8 nm).

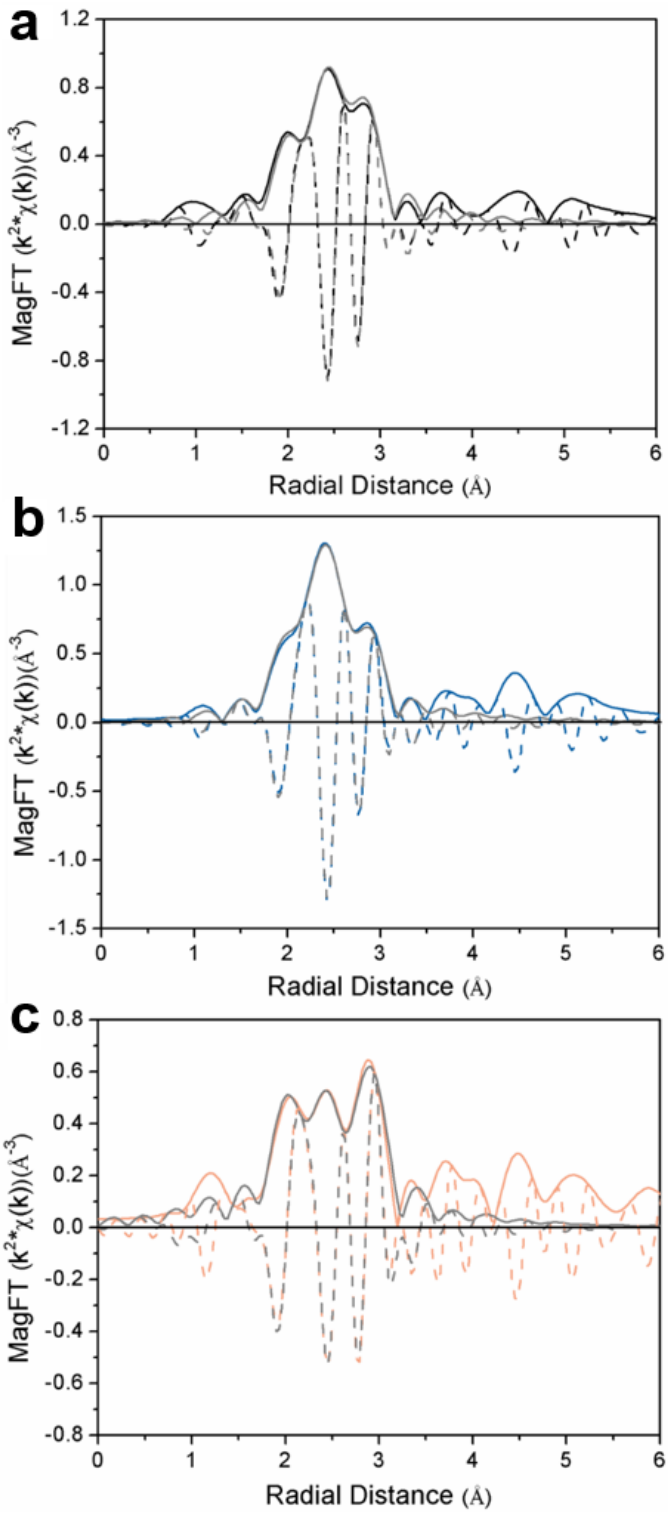

Figure S3.9 The magnitude (solid) and imaginary (dash) part of the Fourier transform of the k^2 weighted EXAFS and corresponding first shell fit (grey) for **(a)** Pt/SiO_2 (black), **(b)** $Pt/Ti_3C_2T_x$ (blue) and **(c)** Pt/Nb_2CT_x (orange). The fitting ranges are Δk = 3.0-12.2 $Å^{-1}$ and ΔR = 1.6-3.2 Å. Corresponding fitting results are listed in Table S3.1.

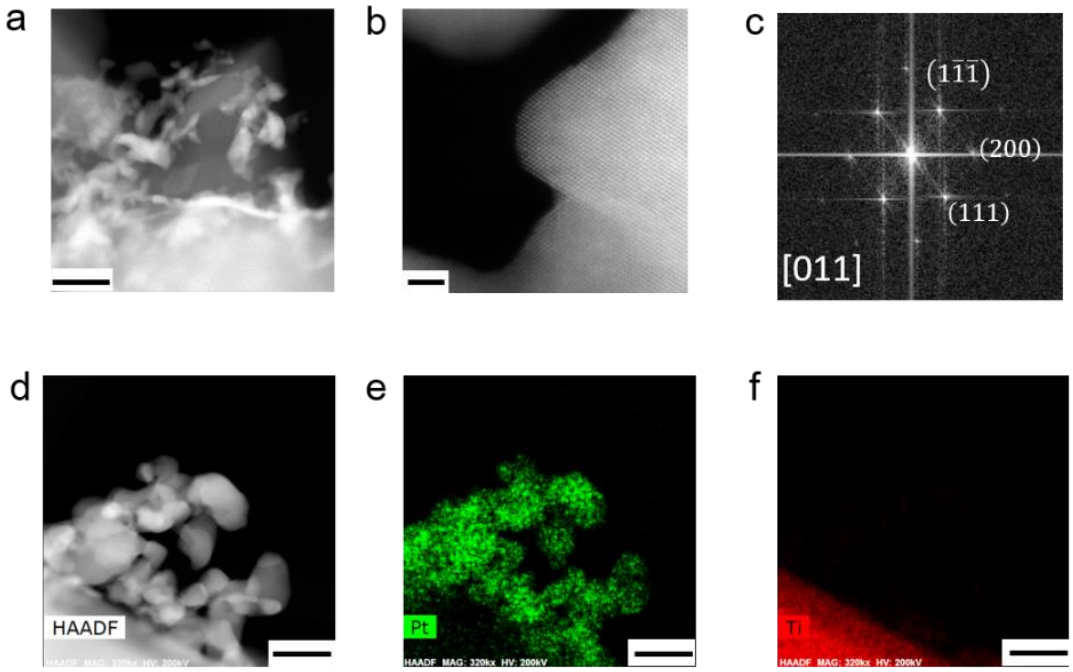

Figure S3.10 Pt/TiC (bulk carbide) sample reduced at 550°C by 4% H_2. (a) HAADF-STEM image of Pt/TiC. (b-c) atomic resolution HAADF-STEM image and corresponding FFT patterns of Pt/TiC. (d-f) EDS analysis of Pt/TiC. Sale bars: (a), (d), (e), (f) 50 nm, and (b) 2 nm.

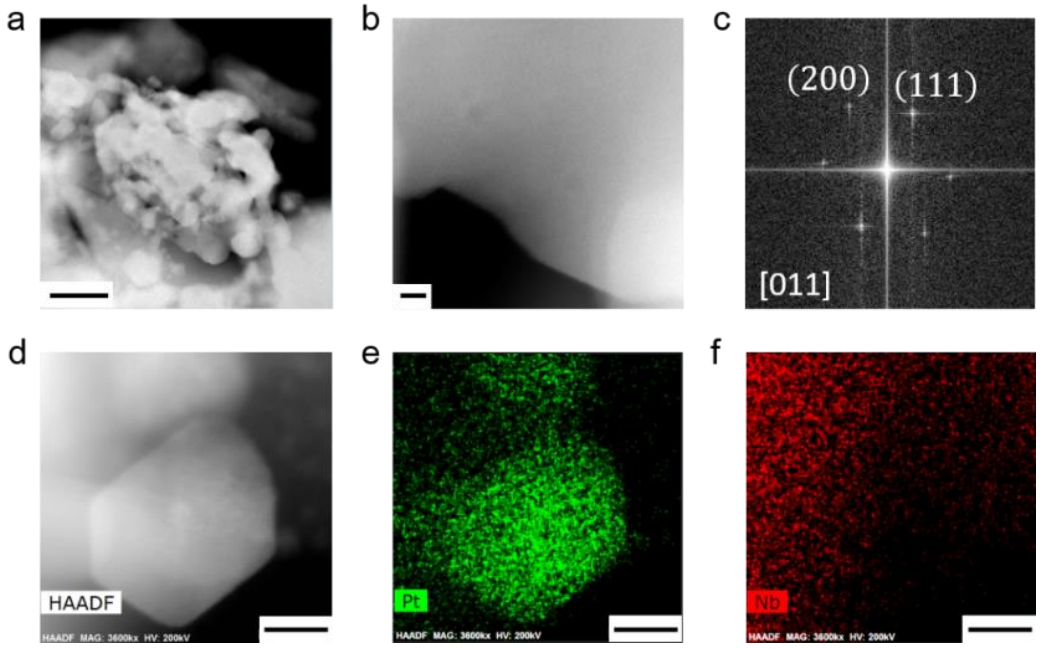

Figure S3.11 Pt/NbC (bulk carbide) sample reduced at 550°C by 4% H_2. (a) HAADF-STEM image of Pt/NbC, the scale bar corresponds to 100 nm. (b-c) atomic resolution HAADF-STEM image and corresponding FFT patterns of Pt/NbC, the scale bar in (b) is 2 nm. (d-f) EDS analysis of Pt/NbC, scale bars 5 nm.

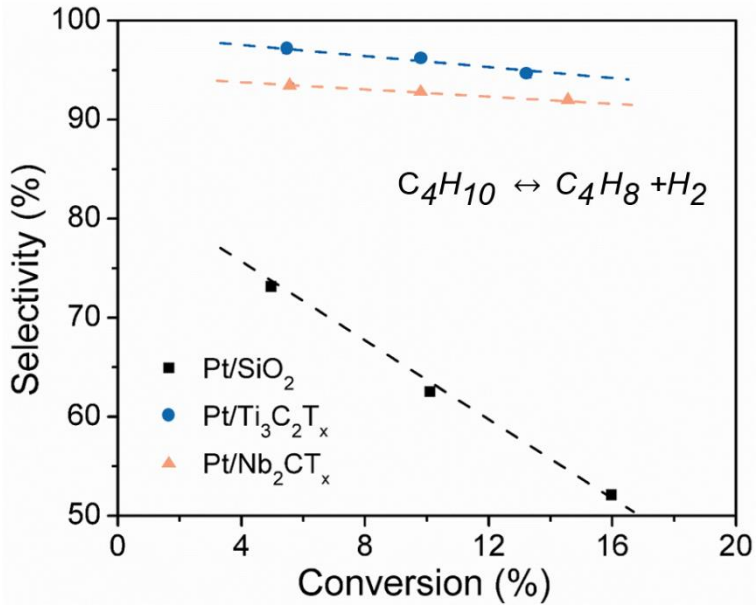

Figure S3.12 Plots of conversion *vs.* selectivity of iso-butane dehydrogenation measured in 100 cm^3/min of 2.5 % C_4H_{10}, 2.5 % H_2 balanced in N_2 at 1.5 atm and 450 °C for Pt/ $Ti_3C_2T_x$, Pt/Nb_2CT_x and Pt/SiO_2 catalysts.

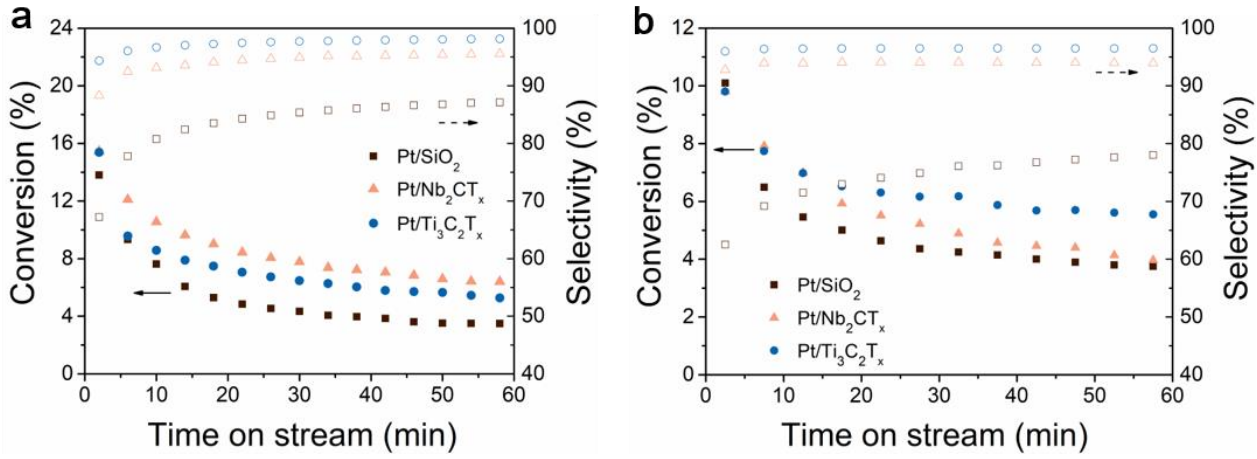

Figure S3.13 (a) Time on stream of propane dehydrogenation reaction over Pt/MXenes and Pt/SiO_2 catalysts. (b) Time on stream of isobutane dehydrogenation reaction over Pt/MXenes and Pt/SiO_2 catalysts.

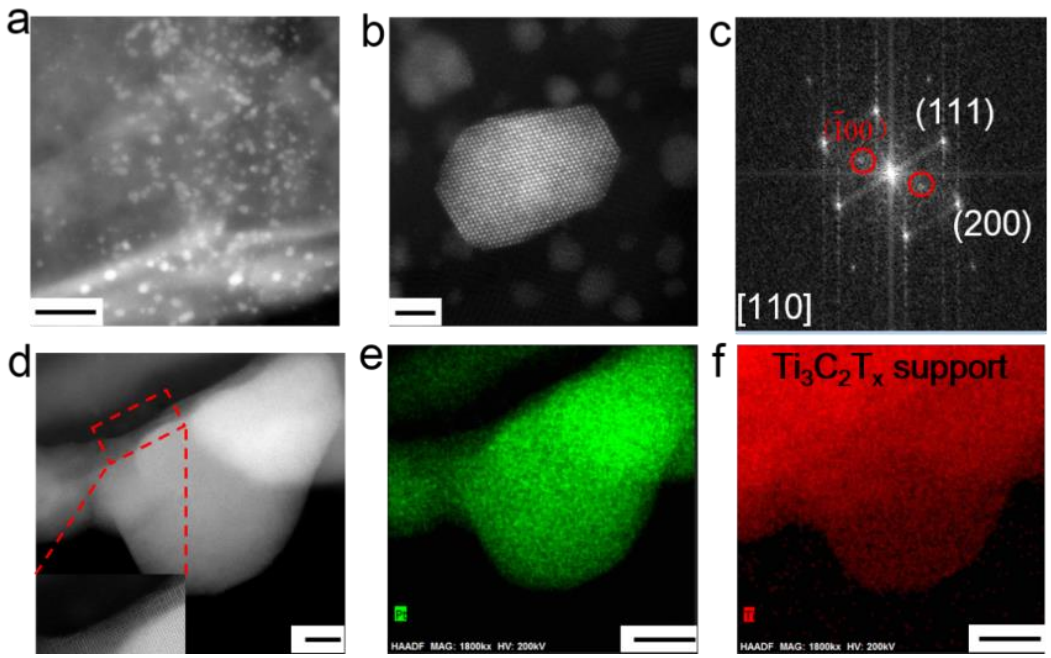

Figure S3.14 (a) HAADF-STEM image on post PDH Pt/$Ti_3C_2T_x$ catalyst, the scale bar corresponds to 50 nm. (b-c) Atomic resolution HAADF-STEM image and FFT pattern of Pt_3Ti NP, the scale bar in (b) is 2 nm. (d-f) EDS analysis of used Pt/$Ti_3C_2T_x$ catalyst, scale bars: (d) 5nm, (e) and (f) 9 nm.

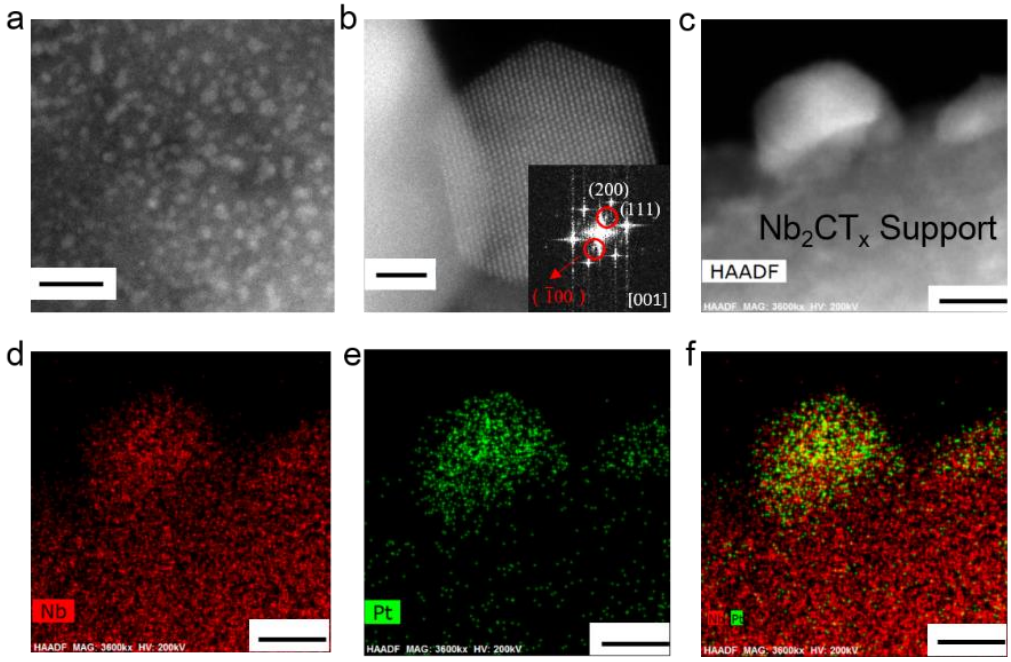

Figure S3.15 (a) HAADF-STEM image on post PDH Pt/Nb_2CT_x catalyst, scale bar 10 nm. **(b)** Atomic resolution HAADF-STEM image and FFT pattern of Pt_3Nb NP, scale bar 2 nm. (c-f) EDS analysis of used Pt/Nb_2CT_x catalyst, scale bars 5 nm.

Table S3.1 Quantitative information of the EXAFS fits (Figure S3.9)

Sample	Scattering Pair	S_0^2	CN #	r (Å) #	ΔE_0 (eV) #	σ^2 (Å ^{2}) #	R factor
Pt/SiO_2	Pt-Pt	0.77 *	8.6	2.74	7.1	0.006	0.004
$Pt/Ti_3C_2T_x$	Pt-Pt	0.77 *	6.6	2.75	6.2	0.006	0.003
	Pt-Ti		3.4	2.75		0.009	
Pt/Nb_2CT_x	Pt-Pt	0.77 *	6.7	2.77	5.5	0.006	0.011
	Pt-Nb		1.8	2.75		0.008	

* The S_0^2 is fixed at the value obtained by fitting a Pt foil reference.

The average error in CN (coordination number) is 1, in r (bond length) is 0.01 Å, in ΔE_0 (energy shift) is 1.0 eV and in σ^2 (Debye-Waller factor) is 0.001 Å^2.

3.10 Supplementary References

1 Paolo, G. *et al.* QUANTUM ESPRESSO: a modular and open-source software project for quantum simulations of materials. *J. Phys.: Condens. Matter* **21**, 395502 (2009).

2 Laasonen, K., Car, R., Lee, C. & Vanderbilt, D. Implementation of ultrasoft pseudopotentials in ab initio molecular dynamics. *Phys. Rev. B* **43**, 6796-6799 (1991).

3 Laasonen, K., Pasquarello, A., Car, R., Lee, C. & Vanderbilt, D. Car-Parrinello molecular dynamics with Vanderbilt ultrasoft pseudopotentials. *Phys. Rev. B* **47**, 10142-10153 (1993).

4 Perdew, J. P., Burke, K. & Ernzerhof, M. Generalized gradient approximation made simple. *Phys. Rev. Lett.* **77**, 3865-3868 (1996).

5 Monkhorst, H. J. & Pack, J. D. Special points for Brillouin-zone integrations. *Phys. Rev. B* **13**, 5188-5192 (1976).

CHAPTER 4. IN SITU FORMED PT_3TI NANOPARTICLES ON A TWO-DIMENSIONAL TRANSITION METAL CARBIDE (MXENE) USED AS EFFICIENT CATALYSTS FOR HYDROGEN EVOLUTION REACTIONS

Zhe Li,[†] Zhiyuan Qi,[‡] Siwen Wang,[§] Tao Ma,[‖] Lin Zhou,[‖] Zhenwei Wu,[⊥] Xuechen Luan,[‡] Fang-Yi Lin,[†] Minda Chen,[‡] Jeffrey T. Miller,[⊥] Hongliang Xin,[§] Wenyu Huang,[‡] and Yue Wu[†]

[†] Department of Chemical and Biological Engineering and [‡] Department of Chemistry, Iowa State University, Ames, Iowa 50011, United States|

[§]Department of Chemical Engineering, Virginia Polytechnic Institute and State University, Blacksburg, Virginia 24061, United States

[‖]Division of Materials Science and Engineering, Ames National Laboratory, Ames, Iowa 50011, United States

[⊥]Davison School of Chemical Engineering, Purdue University, West Lafayette, IN 47907, United States

Modified from a manuscript published by Nano Letters

4.1 Abstract

The design of efficient catalysts capable of delivering high currents at low overpotentials for hydrogen evolution reactions (HERs) is urgently needed to use catalysts in practical applications. Herein, we report platinum (Pt) alloyed with titanium (Ti) from the surface of $Ti_3C_2T_x$ MXenes to form Pt_3Ti intermetallic compound (IMC) nanoparticles (NPs) via in situ coreduction. In situ X-ray absorption spectroscopy (XAS) indicates that Pt undergoes a temperature-dependent transformation from single atoms to intermetallic compounds, and the catalyst reduced at 550 ºC exhibits superior HER performance in acidic media. The Pt/$Ti_3C_2T_x$-550 catalyst outperforms

commercial Pt/Vulcan and has a small overpotential of 32.7 mV at 10 mA cm^{-2} and a low Tafel slope of 32.3 mV dec^{-1}. The HER current was normalized by the mass and dispersion of Pt, and the mass activity and specific activity of Pt/$Ti_3C_2T_x$-550 are 4.4 and 13 times higher, respectively, than those of Pt/Vulcan at an overpotential of 70 mV. The density functional theory (DFT) calculations suggest that the (111)- and (100)-terminated Pt_3Ti nanoparticles exhibit *H binding comparable to Pt(111), while the (110) termination has an *H adsorption that is too exergonic, thus poisoned in the low overpotential region. This work demonstrates the potential of MXenes as platforms for the design of electrocatalysts and may spur future research for other MXene-supported metal catalysts that can be used for a wide range of electrocatalytic reactions.

4.2 Introduction

Hydrogen evolution reactions (HERs) are a critical link between renewable energy sources and energy conversion applications such as hydrogen fuel cells.[1] At present, the most efficient elemental metal electrocatalyst in acidic media is platinum (Pt).[2,3] However, Pt is scarce and expensive, necessitating the development of catalysts with a reduced precious metal content and enhanced activity.[4] To fulfill the cost-effective utilization of Pt, the number of active sites has been increased, for example, by reducing the particle size, and the activity of each active site has been boosted via tuning the local electronic structure.[5,6] Alloying Pt with nonnoble metals represents an effective route for simultaneously reducing the Pt amount and enhancing the intrinsic activity of electrocatalysts.[7,8] Moreover, Pt-alloyed nanoparticles (NPs) can be prepared with various compositions and tunable structures,[9] and their thermodynamic stability benefits catalyst regeneration in industrial applications.[10] As a result, Pt-based alloy NPs with controlled particle sizes are an attractive alternative strategy for promoting HER activity.[11] Well-dispersed bimetallic NPs have altered electronic structures with optimized binding to the reaction intermediate *H, and

their use is promising to realize the two main strategies[4] (i.e., increasing the number of active sites and enhancing the reactivity of each active site) employed for designing HER catalysts.

Platinum-based intermetallic compounds (IMCs) represent an important class of materials in electrocatalysis due to their well-defined structural and tunable electronic properties.[12] Among IMCs, Pt alloyed with early transition metals is well-known for its superior thermal and chemical stabilities owing to the presence of strong Lewis acid and base interactions.[13] For instance, Pt_3Ti has one of the largest formation enthalpies (-298 kJ/mol) found among Pt-based IMCs.[14] However, early transition metals (denoted as M) are more oxyphilic compared to late transition metals and main group metals[15], and thus, the standard reduction potentials of platinum and M salts are quite different (e.g., the standard reduction potentials of Ti^{2+} and $[PtCl_4]^{2-}$ are -1.63 V and +0.73 V, respectively), leading to barriers in their coreduction at a similar rate to form intermetallic NPs.[16] To reduce and incorporate M metals into the Pt lattice of a particle with a controlled size, strong reducing agents (e.g., potassium triethylborohydride) and organic capping ligands, such as oleylamine, are often employed, but these reagents require complicated experimental procedures and may form carbonaceous species that block the active sites.[17] Therefore, the synthesis of Pt-M IMCs through chemical coreduction remains a significant challenge, and a facile method to obtain Pt-M IMCs will benefit their study and application.

Recently, the family of two-dimensional (2D) early transition metal carbides (MXenes), especially $Ti_3C_2T_x$ (where T represents surface terminations such as -O and -OH), has garnered attention for electrocatalysis due to its high electronic conductivity and hydrophilic nature.[18] However, the electrocatalytic performance of these materials is impaired by the limited number of active sites on the surface of the carbides.[19] Therefore, MXene-based hybrid structures are often desired to enhance the electrochemical activity.[20-22] Herein, we report the in situ formation of Pt_3Ti

intermetallic nanoparticles (iNPs) on 2D titanium carbide ($Ti_3C_2T_x$) as an efficient electrocatalyst for HERs. The extent of IMC formation and the size of iNPs depend on the annealing temperature, and 550 ºC is the optimal reduction temperature for achieving the highest HER activity, due to the enhanced electrical conductivity and optimized H* adsorption strength of the catalyst. The catalyst demonstrates a superior HER performance, as it has a lower overpotential, smaller Tafel slope, greater stability, higher mass and better specific activity compared to commercial platinum/Vulcan (Pt/C) catalysts.

4.3 Results and Discussion

In general, the bulk Ti_3AlC_2 synthesized via spark plasma sintering was etched by HF to obtain the 2D $Ti_3C_2T_x$ MXene (Figure S4.1a).[23] A series of characterizations were conducted to confirm the two-dimensionality of the MXene support. The powder X-ray diffraction (XRD) pattern (Figure S4.1b) shows that the most intense peaks corresponding to the nonbasal plane of Ti_3AlC_2 ($2\theta \approx 39°$) disappear after the HF treatment, and the (002) peak of the $Ti_3C_2T_x$ MXene shifts to a lower angle, indicating that the lattice parameter has expanded along the [001] direction. The SEM image (Figure S4.1c) illustrates the exfoliation along the basal plane, where $Ti_3C_2T_x$ exhibits an accordion-like morphology that is typical of the MXene family.[18] After sonication (see the supporting information), $Ti_3C_2T_x$ nanosheets with curved edges can be obtained (Figure S4.2a), and the selected area electron diffraction (SAED) pattern indicates the hexagonal symmetry inherited from bulk Ti_3AlC_2 (inset of Figure S4.2b). Atomic force microscopy (AFM) was employed to study the thickness of the $Ti_3C_2T_x$ nanosheets (Figure S4.3). The AFM height profile, denoted by the solid line, shows that the $Ti_3C_2T_x$ flake has different thicknesses; the thinner part is approximately 4.5 nm-thick (trilayer),[24] and the height of the thicker part is 18 nm, which corresponds to multilayers of $Ti_3C_2T_x$.

Platinum precursors were then loaded onto the resulting $Ti_3C_2T_x$ MXene (denoted as $Pt/Ti_3C_2T_x$) by incipient wetness impregnation (IWI), which was followed by a subsequent reduction under a H_2 atmosphere at 550 ºC (see the supporting information for detailed procedures). High-angle annular dark-field scanning transmission electron microscopy (HAADF-STEM) shows that the NPs are well distributed on the MXene support with an average diameter of 6.6 ± 3.5 nm (Figure 4.1a and Figure S4.5). To study the composition of the NPs, an energy-dispersive X-ray spectroscopy (EDS) line scan was performed on an NP hanging over the vacuum (to avoid signals from the support). The spectra (Figures 4.1b, c) show that the Ti and Pt signals are evenly distributed throughout the NP; core-shell structures were not observed, and neither element segregated on the surface. The atomic resolution HAADF-STEM image (Figure 4.1d) shows the ordered intermetallic structures of a NP. The superlattice spots in the fast Fourier transform (FFT) pattern (Figure 4.1d inset) further confirm the formation of the Pt_3Ti IMC phase. The interplanar spacing measured for the {110} and {001} planes are 2.78 and 3.91 Å, respectively, which matches the expected interplanar spacings of a Cu_3Au type Pt_3Ti IMC. A NP was viewed along the [110] zone axis (Figure 4.1e); two alternating columns were observed, where the brighter columns consist of all Pt atoms, and the darker columns alternate between Pt (green spheres) and Ti atoms (pink spheres). The experimental STEM image agrees well with the simulated image obtained for L_{12} ordered Pt_3Ti nanoalloys (Figure 4.1f), indicating that Pt_3Ti is formed by the in situ coreduction of the Pt precursor and $Ti_3C_2T_x$ MXene.

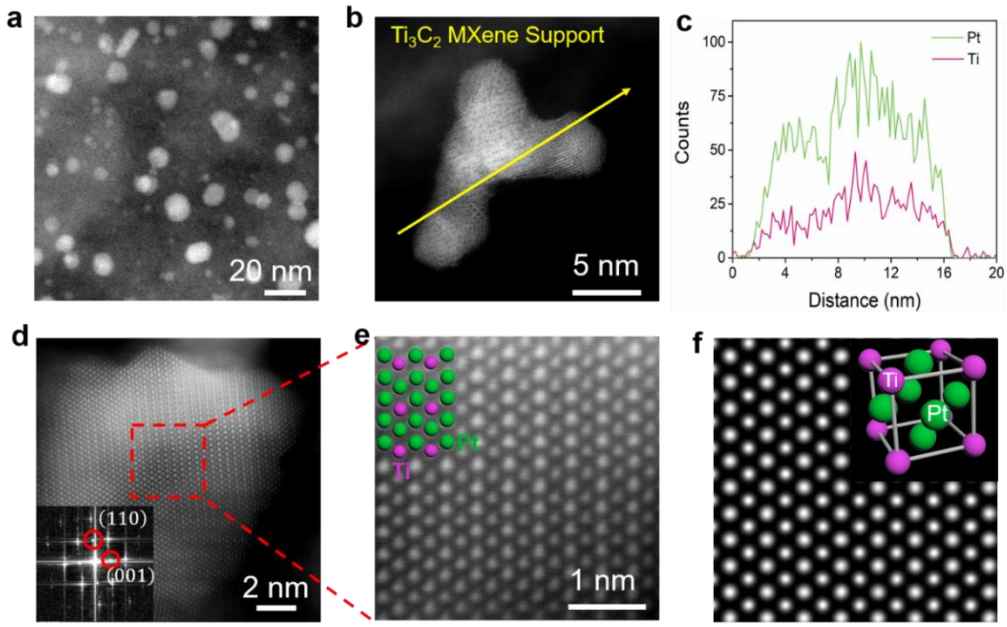

Figure 4.1 Aberration-corrected HAADF-STEM. (a) HAADF-STEM image of Pt_3Ti NPs on a $Ti_3C_2T_x$ MXene support reduced at 550 ºC. (b, c) EDS analysis of the Pt_3Ti NPs. (d, e) Atomic resolution HAADF-STEM image of Pt/$Ti_3C_2T_x$-550. Insets of d and e show the FFT pattern of a NP and sphere models of the Pt_3Ti (110) surface, respectively. (f) Simulated STEM image of Pt_3Ti along the [110] direction; inset shows the face centered cubic (fcc) structure of the Pt_3Ti IMC.

To investigate the influence of the reduction temperature on the chemical environment of the formed IMCs, in situ X-ray absorption spectroscopy (XAS) was conducted. Fresh Pt/$Ti_3C_2T_x$ samples were reduced at four different temperatures (200, 400, 550 and 700 ºC, designated as Pt/$Ti_3C_2T_x$-200, Pt/$Ti_3C_2T_x$-400, Pt/$Ti_3C_2T_x$-550, and Pt/$Ti_3C_2T_x$-700, respectively), and a Pt/SiO_2 sample reduced at 550 ºC was used as the reference. The particle sizes of the catalysts were first studied by STEM, and the Pt/$Ti_3C_2T_x$-400, Pt/$Ti_3C_2T_x$-550, and Pt/$Ti_3C_2T_x$-700 samples were shown to have particle sizes of 5.3 ± 2.1, 6.6 ± 3.5 and 9.0 ± 4.1 nm, respectively (Figures S4.4-S4.6). In contrast, bright spots are observed in the STEM image of Pt/$Ti_3C_2T_x$-200, implying that single Pt atoms formed on the MXene support (Figure S4.7). In the in situ X-ray absorption near edge structure (XANES) spectra obtained at the Pt L_{III} edge (Figure 4.2a), Pt/$Ti_3C_2T_x$-200 has a much higher intensity than the other Pt/$Ti_3C_2T_x$ catalysts, indicating that the Pt precursor is not

reduced at 200 ºC.[25] The white lines in the XANES spectra obtained for the Pt/$Ti_3C_2T_x$ catalysts reduced at other temperatures are slightly narrower and more intense compared to that of Pt/SiO_2, indicating a change in the energy of the unoccupied *d* states for samples reduced at different temperatures.[26] The XANES energies of Pt/$Ti_3C_2T_x$-200, Pt/$Ti_3C_2T_x$-550 and Pt/$Ti_3C_2T_x$-700 (11.5653, 11.5646 and 11.5648 keV) are higher than that of Pt/SiO_2 (11.5640 keV), while the energy of Pt/$Ti_3C_2T_x$-400 (11.5640 keV) is identical to that of Pt/SiO_2. The disparity in the XANES energies indicates that the density of the unoccupied 5*d* states of Pt is altered by reducing Pt/$Ti_3C_2T_x$ at various temperatures.

The magnitude of the Fourier transform of the extended X-ray absorption fine structure (EXAFS) spectra (Figure 4.2b) shows that the Pt/$Ti_3C_2T_x$ catalysts reduced at 400, 550 and 700 ºC have a central peak with higher intensity than that of Pt/SiO_2 due to the in-phase constructive interference between the scattering of Pt-Pt and Pt-Ti. In contrast, the results of EXAFS show that the Pt-Pt contribution at approximately 2.5 Å is absent in Pt/$Ti_3C_2T_x$-200, indicating the presence of atomic Pt species. Fitting the EXAFS spectra (Figure S4.8) reveals the coordination numbers (CNs) and bond distances of Pt, as summarized in Table S4.1. The fitting results of Pt/$Ti_3C_2T_x$-200 show 4.1 Pt-N(O) bonds at 2.06 Å, suggesting that the Pt precursor is not fully reduced at 200 ºC, and Pt remains as single atoms on the MXene support. This result is consistent with the STEM results. The EXAFS spectrum of Pt/$Ti_3C_2T_x$-400 is slightly different from that of the monometallic Pt supported on SiO_2; the fit gives 8.5 Pt-Pt bonds at 2.75 Å and, potentially, a very minor contribution from a second scattering path (0.3 Pt-Ti bonds at 2.74 Å), implying the formation of Pt NPs and a small amount of surface Pt-Ti alloy. Increasing the reduction temperature to 550 ºC leads to the fitting results showing 6.6 Pt-Pt bonds at 2.75 Å and 3.4 Pt-Ti bonds at 2.75 Å. The ratio of Pt-Pt CN to Pt-Ti is ~2, which is consistent with that of the ideal Pt_3Ti structure, which

features 8 Pt-Pt bonds and 4 Pt-Ti bonds for each Pt atom (where the total CN of Pt/$Ti_3C_2T_x$-550 is less than 12 due to the unsaturated bonds on the NP surfaces). The formation of Pt_3Ti IMC nanoparticles in Pt/$Ti_3C_2T_x$-700 is also confirmed by atomic resolution HAADF-STEM (Figure S4.9). Annealing the sample at 700 ºC results in larger CNs and, likely, further Ti enrichment in the NPs. The Pt-Pt and Pt-Ti CNs increase to 7.2 and 4.1, respectively, with minor changes in the bond distances (Table S4.1). Notably, the total CN increases with increasing annealing temperatures, indicating an increase in the average particle size, which is consistent with the results of STEM. The XRD patterns (Figure S4.10) show that the shoulder peak at ~40º can be attributed to the (111) planes of the supported metal in Pt/$Ti_3C_2T_x$ catalysts as it is absent in the XRD pattern obtained for the reduced $Ti_3C_2T_x$ sample. The shoulder peaks observed in the Pt/$Ti_3C_2T_x$-550 and Pt/$Ti_3C_2T_x$-700 XRD patterns deviate from the position of the Pt (111) planes and shift to higher values, implying the formation of IMCs. However, it is challenging to determine the position of the shoulder peaks, as they interfere with peaks of the MXene support, making in situ XAS essential for studying the structures of the supported metal on $Ti_3C_2T_x$ MXene.

Our results suggest that Pt undergoes a three-stage transformation on the surface of the $Ti_3C_2T_x$ MXene upon reduction at different temperatures. The temperature-dependent transformation of Pt also sheds light on the mechanism of the formation of Pt_3Ti. First, unlike conventional supports, such as SiO_2 and Al_2O_3, where Pt nanoparticles are formed by reducing an impregnated $Pt(NH_3)_4(NO_3)_2$ precursor with H_2 at 200 ºC,[27,28] Pt remains as single atoms on the $Ti_3C_2T_x$ MXene under the same treatment, implying that the precursor binds strongly on the surface of the MXene. Second, after increasing the reduction temperature to 400 ºC, Pt is reduced, as shown by the attenuated intensity in the XANES spectra (Figure 4.2a). The white line of Pt/$Ti_3C_2T_x$-400 is still slightly higher than that of Pt/SiO_2, while the edge energies are the same,

implying the formation of Pt nanoparticles with minor amounts of Pt-Ti alloy present on the NP surfaces. Third, Pt_3Ti IMCs are formed when the reduction temperature reaches 550 ºC, and intermetallic nanoparticles with larger particle sizes are retained at a higher temperature (700 ºC). The formation of the IMCs can be attributed to chemical reactions between platinum and the $Ti_3C_2T_x$ MXene support, which result in the incorporation of Ti into the Pt nanoparticles. The chemical reactions leading to the formation of IMCs in supported metal catalysts are often designated as reactive metal support interactions (RMSIs).[29]

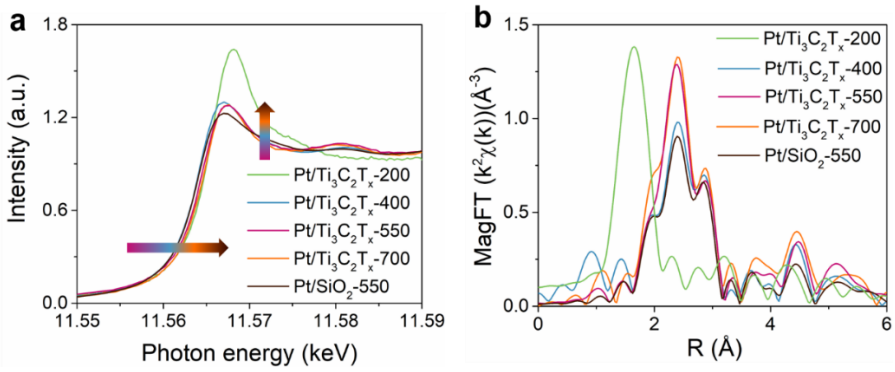

Figure 4.2 In situ X-ray absorption spectroscopy. (a) The Pt L_{III} edge in situ XANES spectra of the $Pt/Ti_3C_2T_x$ catalyst reduced at different temperatures compared to that of Pt/SiO_2. (b) The magnitude of the Fourier transform of the k^2 weighted Pt L_{III} edge in situ EXAFS of Pt/ $Ti_3C_2T_x$ reduced at different temperatures compared to that of Pt/SiO_2.

To evaluate the HER performance of the $Pt/Ti_3C_2T_x$ catalysts, a three-electrode system was used with a H-cell composed of two counterparts. The Pt counter electrode was separated in one counterpart to avoid Pt contamination, and all the potentials were automatically i-R corrected by the potentiostat. The metal loading (Pt) of the tested catalysts was confirmed by inductively coupled plasma mass spectrometry (ICP-MS), and a similar amount of Pt was used in each electrochemical measurement (Table S4.2). The different temperatures used to reduce the catalysts led to quite different electrocatalytic activities. As shown in Figures 4.3a,b, all the $Pt/Ti_3C_2T_x$ catalysts have HER activities that are higher than the bare $Ti_3C_2T_x$ support, which has a large

overpotential (576.8 mV) at 10 mA (η@10 mA). Note that the electrical double layer current of the $Ti_3C_2T_x$ support contributes to the negative current of the Pt/$Ti_3C_2T_x$ catalysts at zero potential, which is also observed in other MXene-based electrocatalysts.[25] Pt/$Ti_3C_2T_x$-550 has the smallest overpotential η at both 10 mA (32.7 mV) and 40 mA (60.8 mV), followed by Pt/$Ti_3C_2T_x$ reduced at 400, 700 and 200 ºC (Table S4.2). Remarkably, the η@10 mA of Pt/$Ti_3C_2T_x$-550 is 23 mV lower than that of a commercial Pt/Vulcan catalyst with the same amount of Pt. Moreover, to avoid the effect of the roughness factor (i.e., the ratio of the catalyst surface area to the geometric surface area) and to provide a fair comparison of the HER activity, the mass activity (i.e., the activity normalized by the mass of Pt) and specific activity (i.e., the activity normalized by the Pt dispersion) are used to reflect the intrinsic activity of the catalysts. The mass activity of Pt/$Ti_3C_2T_x$-550 at an overpotential of 50 mV is 1.3 mA μg^{-1}, which is 3.3 times greater than that of the commercial Pt/Vulcan catalyst (0.4 mA μg^{-1}), as shown in Figure 4.3c. The disparity in the catalytic activity for HERs of the two catalysts increases at the higher overpotential (70 mV), where the mass activity exhibited by Pt/$Ti_3C_2T_x$-550 (2.65 mA μg^{-1}) is 4.4 times higher than that of the Pt/Vulcan catalyst (0.6 mA μg^{-1}). To probe the intrinsic HER activity of Pt/$Ti_3C_2T_x$, H_2 chemisorption (see the supporting information for experimental details) at -60 ºC was employed to measure the Pt dispersion, as the electrochemical surface area (ECSA) could not be determined from the hydrogenation sorption peaks in the cyclic voltammetry measurements, and H_2 chemisorption at ambient temperature was also not successful. The Pt dispersions were determined to be 22.2%, 10.6%, 7.6% and 3.2% for Pt/Vulcan, Pt/$Ti_3C_2T_x$-400, Pt/$Ti_3C_2T_x$-550 and Pt/$Ti_3C_2T_x$-700, respectively (Table S4.3). The specific activity of Pt/$Ti_3C_2T_x$-550 at an overpotential of 50 mV was 17.2 mA (μg surface Pt)$^{-1}$, which is 10 times greater than that of commercial Pt/Vulcan (Figure 4.3d). At a higher overpotential (70 mV), Pt/$Ti_3C_2T_x$-550 delivered

an HER current (34.6 mA (μg surface Pt)$^{-1}$) that was 13 times larger than that delivered by Pt/Vulcan (2.7 mA (μg surface Pt)$^{-1}$). Moreover, Pt/$Ti_3C_2T_x$-550 has the lowest Tafel slope of 32.3 mV dec^{-1} in the range of ~1-10 mA, which suggests that Pt/$Ti_3C_2T_x$-550 has the best HER kinetics among all the tested catalysts (Figure 4.3e). This much lower Tafel slope indicates a more rapid increase in the HER current achieved at a lower overpotential. Furthermore, we doubled the amount of commercial Pt/Vulcan catalysts used for HERs (i.e., the amount of Pt is twice that in Pt/$Ti_3C_2T_x$-550), and a Tafel slope of 32.3 mV dec^{-1} was achieved (Figure S4.11), which is comparable to that of Pt/$Ti_3C_2T_x$-550. This observation further demonstrates that the mass activity of Pt/$Ti_3C_2T_x$-550 is superior to that of commercial Pt/Vulcan, as only half of the amount of platinum is needed to achieve a similar Tafel slope. We also compared the HER activity of our catalyst with the representative noble metal and heterostructure catalysts reported in the literature (Table S4.4), and Pt/$Ti_3C_2T_x$-550 almost exhibited the lowest overpotential and Tafel slope.

To understand the superior performance of Pt/$Ti_3C_2T_x$-550, we measured the double layer capacitance and impedance of all the catalysts. The double layer capacitance (C_{dl}) of the bare support reduced at different temperatures was calculated from the CV curves obtained at different scan speeds. Figure S4.12 shows that C_{dl} decreased with increasing reduction temperatures; the C_{dl} of $Ti_3C_2T_x$-400, $Ti_3C_2T_x$-550 and $Ti_3C_2T_x$-700 were 77.28, 53.41 and 35.38 mF/cm^2, respectively. Figure S4.13 shows a further decrease in the C_{dl} of the Pt/$Ti_3C_2T_x$-400, Pt/$Ti_3C_2T_x$-550, Pt/$Ti_3C_2T_x$-700 catalysts compared to that of their corresponding bare supports, due to the reaction between the MXene support and Pt precursors. The Pt/$Ti_3C_2T_x$-400 and Pt/$Ti_3C_2T_x$-550 catalysts have similar C_{dl} values, which are 50% higher than the C_{dl} of Pt/$Ti_3C_2T_x$-700; therefore, the Pt/$Ti_3C_2T_x$-700 possesses lower specific capacitance and hence smaller surface area than those of Pt/$Ti_3C_2T_x$-400 and Pt/$Ti_3C_2T_x$-550. Lowering the reduction temperature leads to less Ti being

incorporated from the surface of the MXene, and increasing the reduction temperature causes the particles to agglomerate, which reduces the number of the active sites for HERs. The Nyquist plot of Pt/$Ti_3C_2T_x$-550 measured at 0 V shows a much smaller semicircle compared to the Nyquist plots of Pt/$Ti_3C_2T_x$-400 and Pt/$Ti_3C_2T_x$-700 (Figure 4.3f), indicating that Pt/$Ti_3C_2T_x$-550 has the lowest charge transfer resistance (among the three catalysts) during the initial HER process. Note that the bare $Ti_3C_2T_x$ support reduced at 550 ºC exhibits a large resistance at 0 V (Figure S4.14), presumably due to the oxidation of the support after exposing the reduced samples to air, which is consistent with our previous work.[30] This result suggests that the increased charge transfer at the initial state in Pt/$Ti_3C_2T_x$-550 results from the formation of Pt_3Ti nanoparticles with controlled sizes. The formed Pt_3Ti IMCs modulate the adsorptive properties of the active sites that are well dispersed on the MXene support, leading to the fast Faradaic process and superior HER kinetics.

We also performed X-ray photoelectron spectroscopy (XPS) to investigate the change in the MXene support upon reduction (Figure S4.15). High-resolution XPS spectra in the Ti 2*p* region show that the peaks can be deconvoluted into components corresponding to Ti^{4+}, Ti^{3+}, Ti^{2+} and Ti-C. The XPS spectra show that the reduction of Pt/$Ti_3C_2T_x$ leads to the oxidation of the $Ti_3C_2T_x$ support, which is consistent with the results of XRD and the previous study.[30] The surface ratio of Ti-C/Ti determined by XPS is 54.80%, 16.40%, 27.43%, and 18.61% for $Ti_3C_2T_x$, Pt/$Ti_3C_2T_x$-400, Pt/$Ti_3C_2T_x$-550 and Pt/$Ti_3C_2T_x$-700, respectively. These XPS results indicate that Pt/$Ti_3C_2T_x$ reduced at 550 ºC preserves the most Ti-C structures, while the extent of the surface oxidation of Pt/$Ti_3C_2T_x$-400 and Pt/$Ti_3C_2T_x$-700 is higher. The surface oxidation leads to a higher charge transfer resistance, which impairs the HER activity of Pt/$Ti_3C_2T_x$-400 and Pt/$Ti_3C_2T_x$-700.

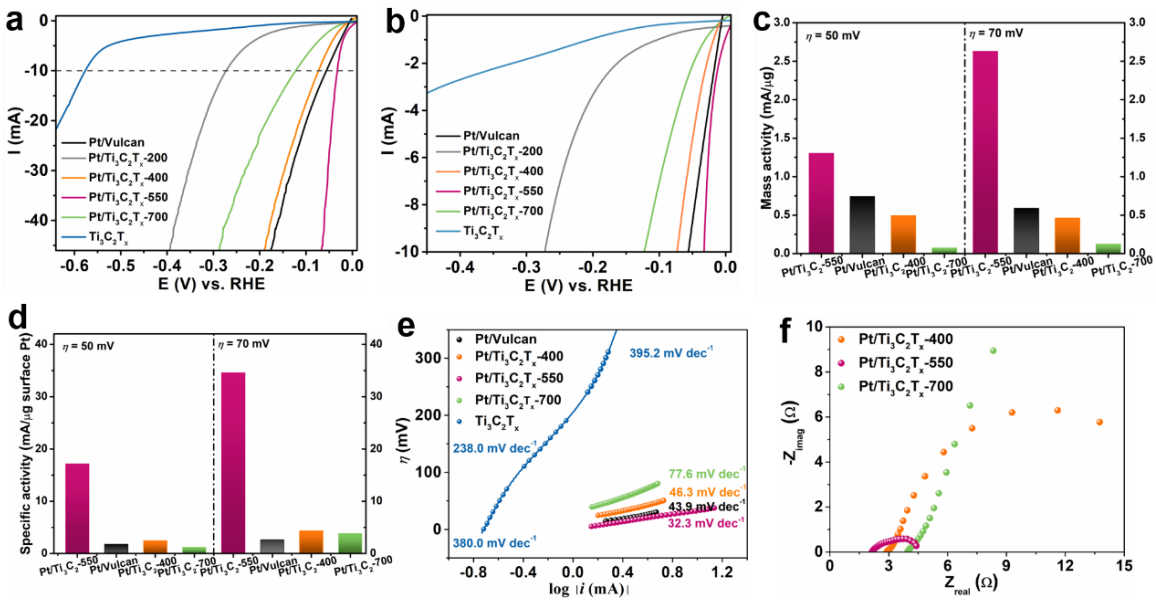

Figure 4.3. Electrochemical characterizations. (a) HER polarization curves at 2 mV s^{-1} in H_2 saturated 0.1 M $HClO_4$ and (b) a magnification of the 0~10 mA region. (c) Mass activity of the Pt/Vulcan and Pt/$Ti_3C_2T_x$ catalysts with different treatments and (d) specific activity of the Pt/Vulcan and Pt/$Ti_3C_2T_x$ catalysts, which is normalized by H_2 chemisorption at -60 ºC. (e) Tafel curves calculated by η = b log|i| + a; (f) Nyquist plots of Pt/$Ti_3C_2T_x$ reduced at different temperatures and measured at 0 V vs. RHE

The stability of Pt/$Ti_3C_2T_x$-550 was then tested via an accelerating stability test (AST) by sweeping the potential between -0.2 and 0.1 V. The HER activity after 1000 and 2000 cycles of the AST was compared with the original HER polarization curve (Figure 4.4a). Interestingly, after the 1000th cycle, the η@10 mA reduced by 2.3 mV, which can be attributed to the structural modification of the catalyst surface. Only an increase of 2.5 mV was observed in the 2000th cycle, indicating the excellent stability of Pt/$Ti_3C_2T_x$-550. The crystal structure of the used Pt/$Ti_3C_2T_x$-550 catalyst was also investigated by HAADF-STEM. Figure 4.4b shows that the {110} and {100} superlattice spots (marked by red circles) are still present in the FFT pattern (inset of Figure 4.4b), indicating that the structure of Pt_3Ti is stable during the HER. It should be noted that no obvious Pt or Ti surface segregation was observed in the spent HER catalyst, as indicated by the atomic resolution image (Figure 4.4b) and the EDS line scan (Figure S4.16).

Density functional theory (DFT) calculations were carried out to gain further insights into the excellent electrocatalytic performance of $Ti_3C_2T_x$-550 for HERs (Figure 4.4c). The formation energy of the Pt_3Ti NPs relative to bulk Pt and Ti, as calculated by DFT, is -0.88 eV, which suggests that Pt_3Ti is thermodynamically stable (see the supporting information for details). According to the Pourbaix diagram, Pt_3Ti is a stable Pt/Ti alloy phase under acidic conditions and applied reduction potentials (Figure S4.17). The HER pathway can be represented by a three-state diagram with an initial (H^+ + e-) state, an intermediate H* state, and a final ½H_2 product.[31] The differential free energy of hydrogen adsorption (ΔG_H*) is a key descriptor of the HER activity, and the optimum value of ΔG_H* should be close to zero to compromise for the energy barriers of the adsorption and desorption steps.[25] The steady-state hydrogen coverage of each surface is determined to be when the differential adsorption free energy is closest to zero. The ΔG_H* values of Pt_3Ti(111) and Pt_3Ti(100) surfaces are -0.01 and -0.05 eV, respectively, which are closer to zero or are comparable to the ΔG_H* values of Pt(111) (-0.03 eV) and Pt(100) (-0.19 eV). Besides, the Pt_3Ti (110) has a too exergonic ΔG_H* values (-0.28 eV), similar to that of Pt (110) (-0.24 eV). Thus, the (110)-type sites of Pt and the Pt_3Ti NPs are poisoned in the low overpotential region. We note that Pt-terminations were used at the (100) and (110) surfaces, because these surfaces have lower surface free energies in a vacuum than their Ti-terminated counterparts. Our calculations indicate that the adsorption of H* on the Pt_3Ti(111) and Pt_3Ti(100) surfaces is neither too strong nor too weak due to the tailored local electronic properties, which indicates that the HER performance of the $Ti_3C_2T_x$-550 catalyst is superior to that of pure Pt. Additionally, the STEM images (Figure 4.1a and Figure S4.18) show that the nanoparticles in Pt/$Ti_3C_2T_x$-550 and Pt/$Ti_3C_2T_x$-700 tend to form cuboctahedral morphologies that are mainly composed of {111} and {100} facets (Figure S4.9b), which endow the catalysts with increased HER activities. The

preference for cuboctahedral-shaped particles can result from the high temperature annealing and was also observed for Pt_3Ni nanoparticles.[32] Considering both the DFT results and electrochemical characterization, the reduction temperature plays a pivotal role in the nature of the active sites, which results in temperature-dependent HER activity. Pt_3Ti outperforms the Pt nanoparticles and unreduced Pt single atoms for HERs, as indicated by both the experimental results and DFT calculations. We note that, although Pt_3Ti can be retained in the Pt/$Ti_3C_2T_x$-700 catalyst, high-temperature reduction (700 ºC) leads to the agglomeration of IMCs and a greater oxidation of the MXene support (compared to Pt/$Ti_3C_2T_x$-550). The superior HER activity of Pt/$Ti_3C_2T_x$-550 results from the in situ formation of Pt_3Ti IMCs with optimized surface reactivities, which modulates hydrogen adsorption at the active sites, and the less oxidized MXene supports, which benefit charge transfer during the HER process.

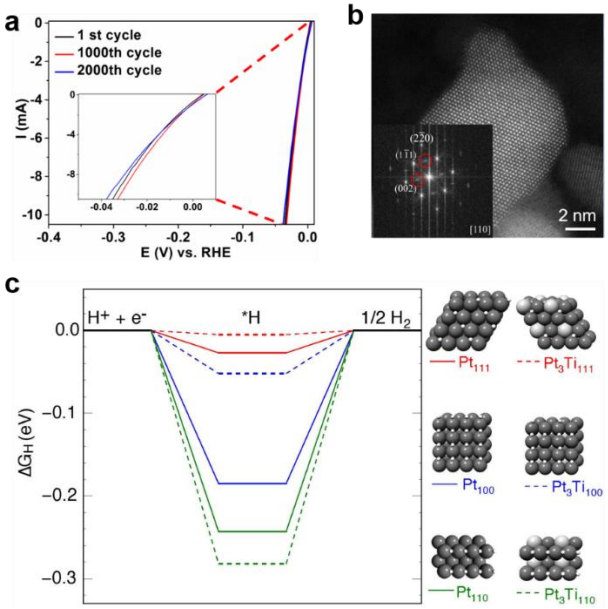

Figure 4.4 Stability test of the in situ formed Pt_3Ti nanoparticle catalysts and DFT calculations. (a) HER curves before and after the stability tests and (b) an HAADF-STEM image of the used Pt/$Ti_3C_2T_x$-550 catalyst (after 1000 cycles), where the inset shows the FFT pattern of a Pt_3Ti nanoparticle. (c) DFT-calculated free energy diagrams of the hydrogen evolution at the Pt(111), Pt_3Ti(111), Pt(100), Pt_3Ti(100), Pt(110) and Pt_3Ti(110) surfaces. The hydrogen coverage was determined to be when the differential adsorption free energy was closest to zero (the structures in the top view are shown).

4.4 Conclusion

In summary, we reported, for the first time, the synthesis of IMC NP electrocatalysts using $Ti_3C_2T_x$ MXenes as both the conductive support and the second metal precursor. The resulting Pt_3Ti nanoparticles were readily formed at 550 ºC, and the ordered Pt_3Ti structure was confirmed by both atomic resolution HADDF-STEM and EXAFS. Compared to the catalysts prepared at other temperatures (200, 400 and 700 ºC), Pt/$Ti_3C_2T_x$-550 had the best catalytic performance for HERs, the smallest overpotential of 32.7 mV (@ 10 mA), a Tafel slope of 32.3 mV dec^{-1}, and the lowest charge transfer resistance. Furthermore, the catalyst was stable in an acidic solution, and no significant activity loss or structure change (e.g., surface segregation) were observed after the HER cycles. The DFT calculations suggest that the (111) and (100) surfaces of Pt_3Ti show comparable *H binding to Pt(111), while the (110) termination has too exergonic *H adsorption, thus poisoned in the low overpotential region. We believe that this route used to synthesize Pt_3Ti/MXene catalysts opens a new avenue for designing a wide variety of MXene-supported metal catalysts for electrocatalytic applications.

4.5 References

1. Seh, Z. W.; Kibsgaard, J.; Dickens, C. F.; Chorkendorff, I.; Nørskov, J. K.; Jaramillo, T. F. *Science* **2017**, *355,* 146-157.

2. Yin, H.; Zhao, S.; Zhao, K.; Muqsit, A.; Tang, H.; Chang, L.; Zhao, H.; Gao, Y.; Tang, Z. *Nat. Commun.* **2015**, *6*, 6430.

3. Jiao, Y.; Zheng, Y.; Jaroniec, M.; Qiao, S. Z. *Chem. Soc. Rev.* **2015,** *44*, 2060-2086.

4. Chao, T.; Luo, X.; Chen, W.; Jiang, B.; Ge, J.; Lin, Y.; Wu, G.; Wang, X.; Hu, Y.; Zhuang, Z.; Wu, Y.; Hong, X.; Li, Y. *Angew. Chem. Int. Ed.* **2017**, *129*, 16263-16267.

5. Li, M.; Zhao, Z.; Cheng, T.; Fortunelli, A.; Chen, C. Y.; Yu, R.; Zhang, Q.; Gu, L.; Merinov, B. V.; Lin, Z.; Zhu, E.; Yu, T.; Jia, Q.; Guo, J.; Zhang, L.; Goddard, W. A.; Huang, Y.; Duan, X. *Science* **2016**, *354*, 1414-1419.

6. Qi, Z.; Xiao, C.; Liu, C.; Goh, T. W.; Zhou, L.; Maligal-Ganesh, R.; Pei, Y.; Li, X.; Curtiss, L. A.; Huang, W. *J. Am. Chem. Soc.* **2017**, *139*, 4762-4768.

7. Chen, C.; Kang, Y. J.; Huo, Z. Y.; Zhu, Z. W.; Huang, W. Y.; Xin, H. L. L.; Snyder, J. D.; Li, D. G.; Herron, J. A.; Mavrikakis, M.; Chi, M. F.; More, K. L.; Li, Y. D.; Markovic, N. M.; Somorjai, G. A.; Yang, P. D.; Stamenkovic, V. R. *Science* **2014**, *343,* 1339−1343

8. Li, Q.; Wu, L.; Wu, G.; Su, D.; Lv, H.; Zhang, S.; Zhu, W.; Casimir, A.; Zhu, H.; Mendoza-Garcia, A.; Sun, S. *Nano Lett.* **2015**, *15*, 2468-2473.

9. Wang, Y.-J.; Zhao, N.; Fang, B.; Li, H.; Bi, X. T.; Wang, H. *Chem. Rev.* **2015,** *115*, 3433-3467.

10. Peng, Z.; Yang, H. *Nano Today* **2009**, *4*, 143-164.

11. Zheng, Y.; Jiao, Y.; Jaroniec, M.; Qiao, S. Z. *Angew. Chem. Int. Ed.* **2015,** *54*, 52-65.

12. Huang, X.; Zhao, Z.; Cao, L.; Chen, Y.; Zhu, E.; Lin, Z.; Li, M.; Yan, A.; Zettl, A.; Wang, Y. M.; Duan, X.; Mueller, T.; Huang, Y. *Science* **2015**, *348*, 1230-1234.

13. Ding, E.; More, K. L.; He, T. *J. Power Sources* **2008**, *175*, 794-799.

14. Abe, H.; Matsumoto, F.; Alden, L. R.; Warren, S. C.; Abruña, H. D.; DiSalvo, F. J. *J. Am. Chem. Soc.* **2008**, *130*, 5452-5458.

15. Cui, Z. M.; Chen, H.; Zhao, M. T.; Marshall, D.; Yu, Y. C.; Abruña, H. D.; DiSalvo, F. J. *J. Am. Chem. Soc.* **2014**, *136*, 10206-10209.

16. Liu, Z.; Qi, J.; Liu, M.; Zhang, S.; Fan, Q.; Liu, H.; Liu, K.; Zheng, H.; Yin, Y.; Gao, C. *Angew. Chem. Int. Ed.* **2018**, *130*, 11852-11856.

17. Yu, W.; Porosoff, M. D.; Chen, J. G. *Chem. Rev.* **2012,** *112*, 5780-5817.

18. Naguib, M.; Mochalin, V. N.; Barsoum, M. W.; Gogotsi, Y. *Adv. Mater.* **2014**, *26*, 992-1005.

19. Yuan, W.; Cheng, L.; An, Y.; Wu, H.; Yao, N.; Fan, X.; Guo, X. *ACS Sustainable Chem. Eng.* **2018**, *6*, 8976-8982.

20. Wu, X.; Wang, Z.; Yu, M.; Xiu, L.; Qiu, J. *Adv. Mater.* **2017,** *29*, 1607017.

21. Ran, J.; Gao, G.; Li, F.-T.; Ma, T.-Y.; Du, A.; Qiao, S.-Z. *Nat. Commun.* **2017,** *8*, 13907.

22. Peng, J.; Chen, X.; Ong, W.-J.; Zhao, X.; Li, N. *Chem.* **2019***, 5,* 18-50.

23. Li, Z.; Yu, L.; Milligan, C.; Ma, T.; Zhou, L.; Cui, Y.; Qi, Z.; Libretto, N.; Xu, B.; Luo, J., Shi, E.; Wu, Z.; Xin, H.; Delgass, W. N.; Miller, J. T.; Wu, Y. *Nat. Commun.* **2018,** *9*, 5258.

24. Ding, L.; Wei, Y.; Li, L.; Zhang, T.; Wang, H.; Xue, J.; Ding, L.-X.; Wang, S.; Caro, J.; Gogotsi, Y. *Nat. Commun.* **2018,** *9*, 155.

25. Zhang, J.; Zhao, Y.; Guo, X.; Chen, C.; Dong, C.-L.; Liu, R.-S.; Han, C.-P.; Li, Y.; Gogotsi, Y.; Wang, G. *Nat. Catal.* **2018,** *1*, 985.

26. Sabnis, K. D.; Cui, Y.; Akatay, M. C.; Shekhar, M.; Lee, W.-S.; Miller, J. T.; Delgass, W. N.; Ribeiro, F. H. *J. Catal.* **2015**, *331*, 162-171.

27. Oudenhuijzen, M.; Kooyman, P.; Tappel, B.; van Bokhoven, J. A.; Koningsberger, D. *J. Catal.* **2002,** *205*, 135-146.

28. Munoz-Paez, A.; Koningsberger, D. *J. Phys. Chem.* **1995,** *99*, 4193-4204.

29. Penner, S.; Armbrüster, M. *ChemCatChem* **2015,** *7* (3), 374-392.

30. Li, Z.; Cui, Y.; Wu, Z.; Milligan, C.; Zhou, L.; Mitchell, G.; Xu, B.; Shi, E.; Miller, J. T.; Ribeiro, F. H.; Wu, Y. *Nat. Catal.* **2018**, *1*, 349-355.

31. Huang, Z.-F.; Song, J.; Li, K.; Tahir, M.; Wang, Y.-T.; Pan, L.; Wang, L.; Zhang, X.; Zou, J.-J. *J. Am. Chem. Soc.* **2016,** *138*, 1359-1365.

32. Kühl, S.; Gocyla, M.; Heyen, H.; Selve, S.; Heggen, M.; Dunin-Borkowski, R.; Strasser, P. *J. Mater. Chem. A* **2019**, *7*, 1149-1159.

4.6 Author Contributions

Z.L. and Z.Q. contributed equally to this work. Z. L. and Y. W. conceived the concept and designed the experiments. Z.Q., X.L., and W.H. conducted the electrochemical tests. L.Z. and T.M. performed the microscopy experiments. S.W. and H.X. carried out the DFT calculations. Z.W. and J.T. M. performed the XAS measurements. F.L and M.C helped XRD characterizations. Z.L., Z.Q., H.X., W.H., and Y.W. wrote the manuscript. All authors discussed the results and commented on the manuscript.

4.7 Acknowledgments

Y. W. appreciates the support from the Herbert L. Stiles Professorship and Iowa State University College of Engineering exploratory research projects. Z.W. and J.T.M. were supported in part by the National Science Foundation under Cooperative Agreement No. EEC-1647722. Use of the Advanced Photon Source was supported by the U.S. Department of Energy, Office of Basic Energy Sciences, under contract no. DE-AC02-06CH11357. MRCAT operations, beamline 10-BM, are supported by the Department of Energy and the MRCAT member institutions. All TEM work was performed at the Sensitive Instrument Facility in Ames Lab. Z.Q., X.L. M.C. and W.H.

acknowledge financial support from the American Chemical Society Petroleum Research Fund (ACS PRF 55170-DNI5). S.W. and H.X. acknowledge financial support from the American Chemical Society Petroleum Research Fund (ACS PRF 55581-DNI5) and the NSF CBET Catalysis Program (CBET-1604984, CBET-1845531). The computational resource used in this work is provided by the advanced research computing at Virginia Polytechnic Institute and State University.

4.8 Supporting Information

4.8.1 Synthesis of Ti_3AlC_2 and $Ti_3C_2T_x$ MXene

The synthesis of Ti_3AlC_2 was achieved by spark plasma sintering (SPS). In details, commercial powders of titanium (II) hydride (Alfa Aesar, 99%), aluminum (Alfa Aesar, 325 meshes, 99.5%) and titanium (IV) carbide (Sigma Aldrich, 325 meshes, 98%) were mixed in a molar ratio of TiH_2/Al/TiC = 1:1:1.8 in a graphite die coated with boron nitride (BN). Excess Al and less than a full equivalent of TiC were added because a small portion of Al will be lost during high-temperature processing, and carbon deficiencies exist in most Al-containing MAX phases. Then, the material was loaded in a Fuji-211lx SPS system and sintered at 1350 °C under 30 MPa for one hour. The resulting Ti_3AlC_2 was then pulverized and sieved through a 325-mesh screen.

The Ti_3AlC_2 powder was treated with 50% HF at 35 °C for 24 hours. The sample was then washed by deionized (DI) water until the pH reached ~5. The resulting powder was collected by centrifugation at 8900 rpm and then dried under vacuum. The $Ti_3C_2T_x$ was stored in a glove box filled with N_2 for future use.

4.8.2 Synthesis of Series of Pt/$Ti_3C_2T_x$

For a typical synthesis, 50 mg of as-synthesized $Ti_3C_2T_x$ MXene powder was immersed by 25 μL of $Pt(NH_3)_4(NO_3)_2$ aqueous solution (0.02 g Pt/mL). The mixture was vacuum dried and ground to ensure the homogeneity, labeled as 1 wt.% Pt/$Ti_3C_2T_x$. The powder was then transferred

into a tube furnace and reduced at different temperatures for at least 30 min under 3% H_2/Ar flow with a ramping rate of 5 ˚C/min to obtained Pt/$Ti_3C_2T_x$-*n* (*n* indicates the reduction temperatures).

4.8.3 Characterizations

The mass loading of Pt was determined by using a Thermo Fisher Scientific X Series 2 inductively coupled plasma mass spectroscopy (ICP-MS). All the Pt-containing samples were digested in the boiling aqua regia solution, and the clear top layers were used for further analysis. X-ray diffraction (XRD) patterns were recorded at room temperature by a Bruker diffractometer with Cu K_α radiation source (λ=1.5406 Å). Transmission electron microscopy (TEM) images were recorded using a TECNAI G2 F20 electron microscope operated at 200 kV. High-resolution, high-angle annular dark field (HAADF) scanning transmission electron microscopy (STEM) imaging was acquired on a Titan Themis 300 probe corrected TEM with a Super-X EDX detector in the Sensitive Instrument Facility of Ames Lab. Extended X-ray absorption fine structure (EXAFS) measurement were performed in Argonne National Lab.

4.8.4 Electrochemical Measurements

All the electrochemical measurements were carried out in a three-electrode system using an electrochemical station (VSP-300, Bio-Logic Science Instruments). Typically, 10 mg of catalysts were dispersed in 100 μL of the mixture solution (DI water: isopropanol: Nafion solution (5 wt%) = 45: 45: 10) by sonication for 30 min to obtain a homogeneous ink. 20 μL of the above catalyst ink was then transferred onto 1 cm^2 area on a carbon fiber electrode (Toray Paper 030) and dried at room temperature in air. HER was conducted in a home-made H-cell with two counterparts isolated by a Nafion-115 film, utilizing carbon fiber electrode with loaded catalysts as a working electrode, Ag/AgCl (saturated KCl) as a reference electrode, and a Pt gauze as the counter electrode. In a typical measurement, the Pt gauze counter electrode was placed in one

counterpart while the working electrode and reference electrode were placed in the other counterpart containing 0.1 M $HClO_4$ as the electrolyte saturated with H_2.

4.8.5 H_2 Chemisorption

H_2 chemisorption was performed in a Micromeritics ASAP 2020 unit. About 200 mg of fresh Pt/$Ti_3C_2T_x$ catalysts were loaded in the sample tube, then the catalysts were reduced at different temperatures (400˚C, 550˚C, and 700˚C) for 1 hour by 10% H_2/Ar (50 ml/min) with a ramping rate of 5 ˚C/min. Then, the gas flow was switched to pure Ar (50 ml/min), and the temperature was decreased and kept at 350˚C for flushing out the adsorbed H_2. Next, the temperature was decreased to the test temperature (-60 ˚C) in Ar (50 ml/min) with a stable baseline. Finally. 10% H_2/Ar was pulsed to the catalysts until no more H_2 absorbed. The Pt dispersion is determined by the total H_2 absorbed.

4.8.6 DFT Calculations

Spin-polarized density functional theory (DFT) calculations were performed using the Vienna Ab initio Simulation Package (VASP) with projector augmented wave pseudopotentials.[1] The revised Perdew-Burke-Ernzerhof (RPBE)[2] exchange-correlation functional within the generalized gradient approximation (GGA) is chosen in consideration of a balance between accuracy and computational cost.[3] The plane wave energy cutoff was 520 eV for bulks and 400 eV for surfaces. All the extended surfaces were modeled by periodic five-layer slabs separated by 30 Å vacuum space along the norm of the surface, with 2×2 supercell for (111) and (100) surfaces and 2×4 supercell for (110) surfaces. The Brillouin zone was sampled on a 6 ×6 × 1 Monkhorst-Pack k-point grid[4] for (111) and (100) surfaces and 6 ×3 × 1 for (110) surfaces. The Pt-terminated surfaces were used for modeling Pt_3Ti(110) and Pt_3Ti(100) because of their lower surface energies than those of Ti-termination. The top three layers of the slab and adsorbates were fully relaxed

until the maximum forces were converged to 0.05 eV/Å. The computational hydrogen electrode is used for relating the free energy of the ($H^+ + e^-$) pair at 0 vs. RHE to that of the gas phase H_2.[5] Zero-point energy and entropic contributions to the free energies were taken from ref.[5]

The formation energy of bulk Pt3Ti is calculated according to equation (1):

$$E = [E(Pt_3Ti)-3*E(Pt)-E(Ti)]/4. \quad (1)$$

where $E(Pt_3Ti)$ is the DFT calculated bulk energy of Pt_3Ti, E(Pt) is the DFT calculated bulk energy of Pt and E(Ti) is the DFT calculated bulk energy of Ti. Here we choose cubic structure for Pt_3Ti, Pt and Ti.

4.9 Supplementary Figures

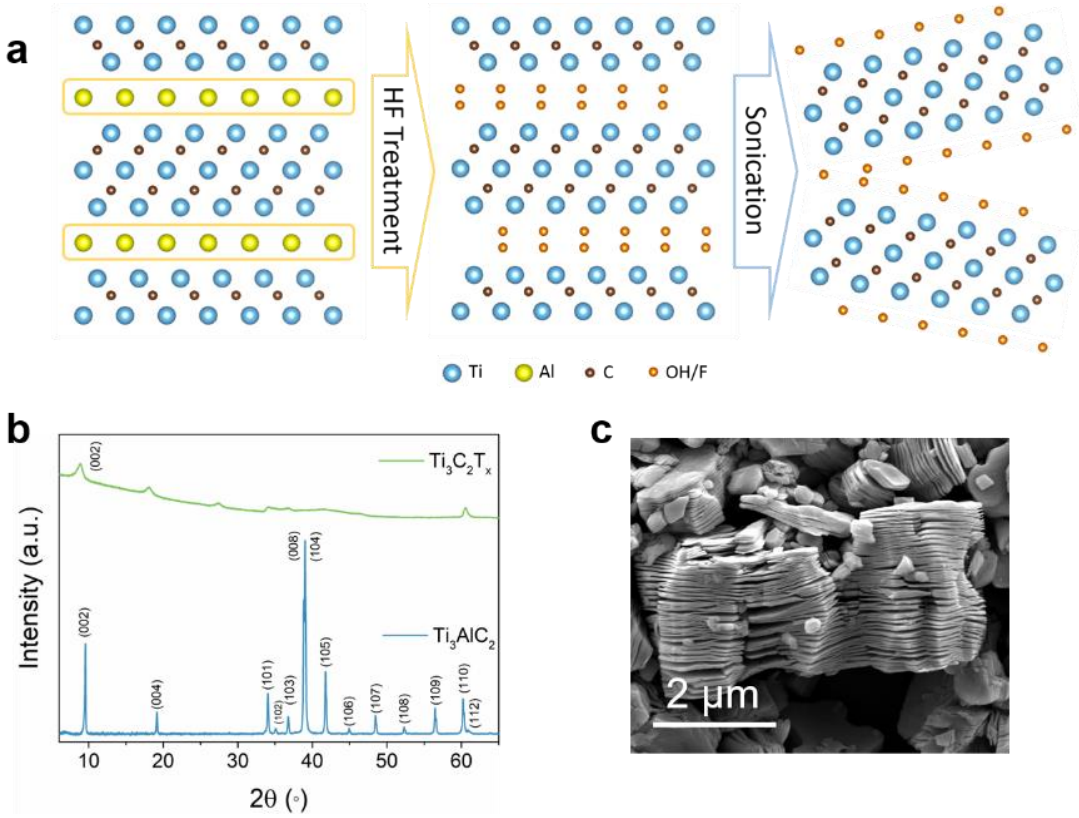

Figure S4.1 (a) schematic illustration of the synthesis of $Ti_3C_2T_x$ MXene. (b) XRD patterns of Ti_3AlC_2 MAX and $Ti_3C_2T_x$ MXene. (c) SEM of $Ti_3C_2T_x$ MXene.

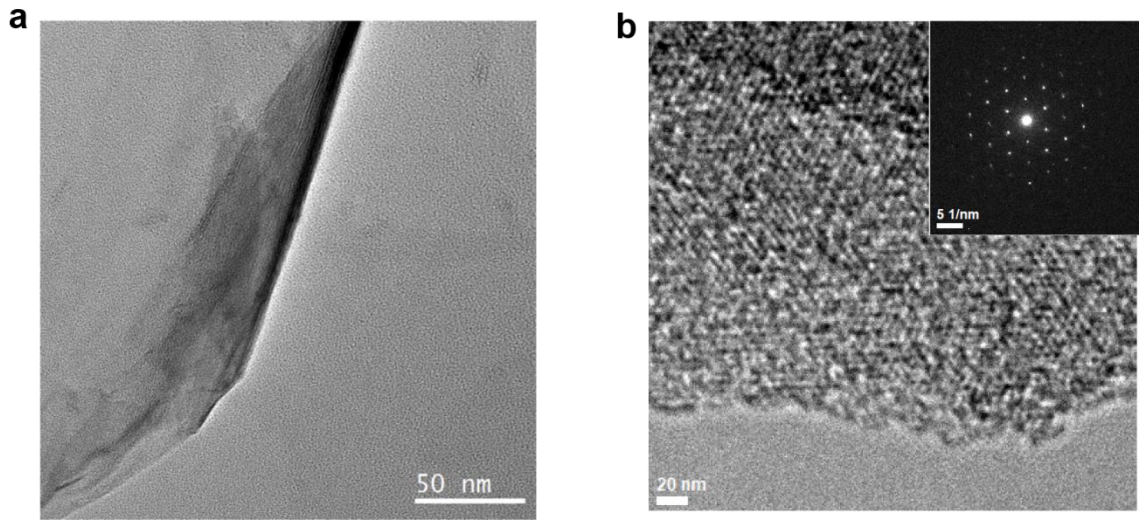

Figure S4.2 (a) and (b) High-resolution TEM image of $Ti_3C_2T_x$ MXene. Inset of (b) is selected area electron diffraction (SAED).

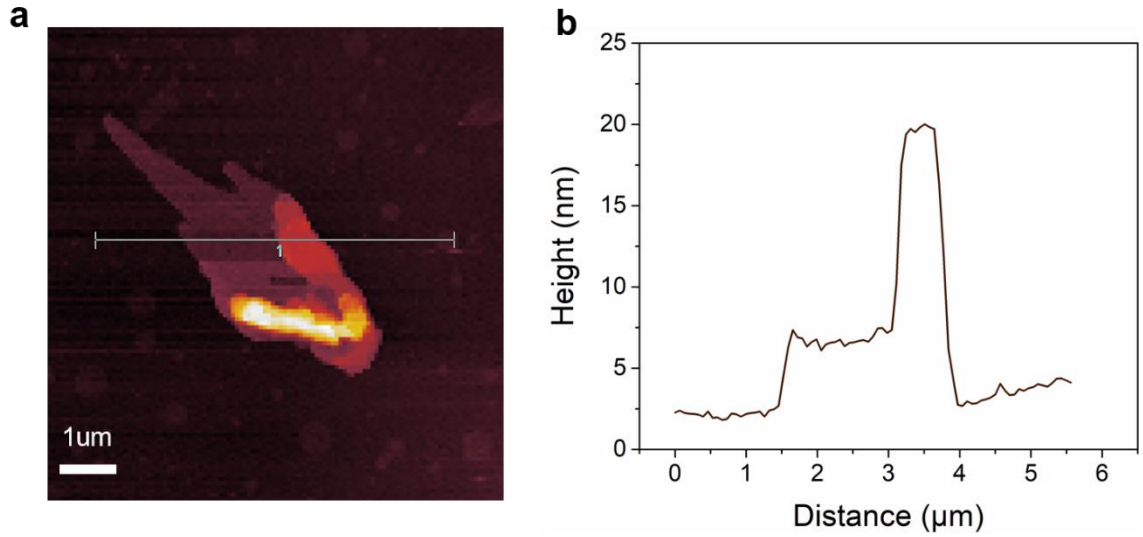

Figure S4.3 (a) The AFM image of exfoliated MXene and (b) the corresponding height measurement.

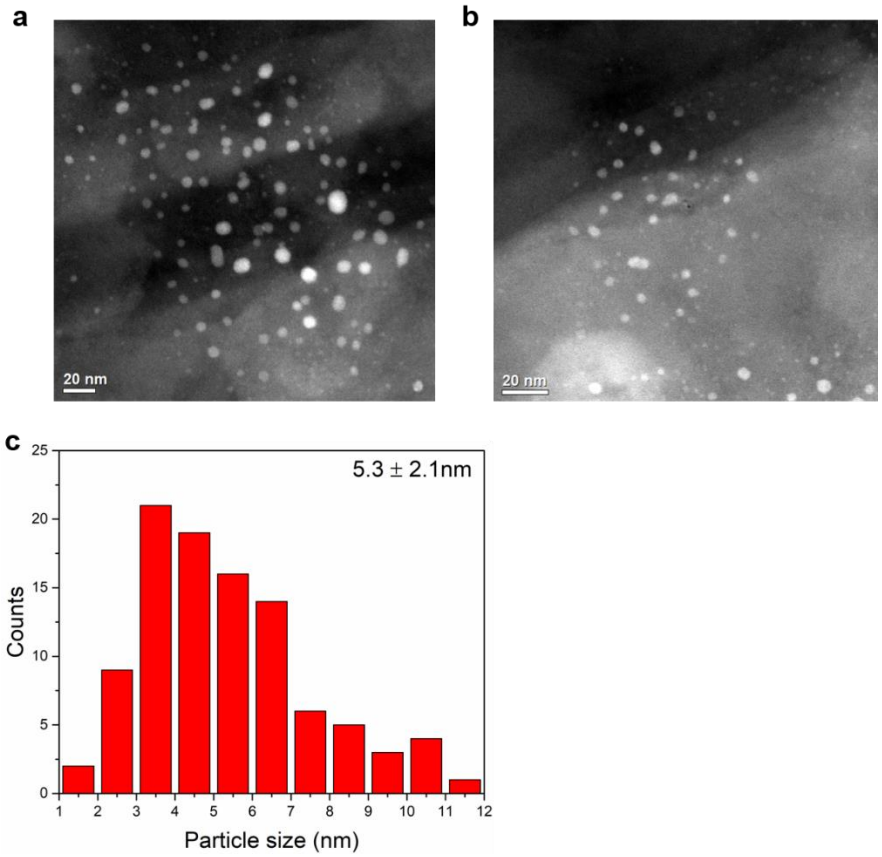

Figure S4.4 Particle size distribution of Pt/$Ti_3C_2T_x$ catalysts reduced at 400°C. The average particle size is 5.3 ± 2.1 nm.

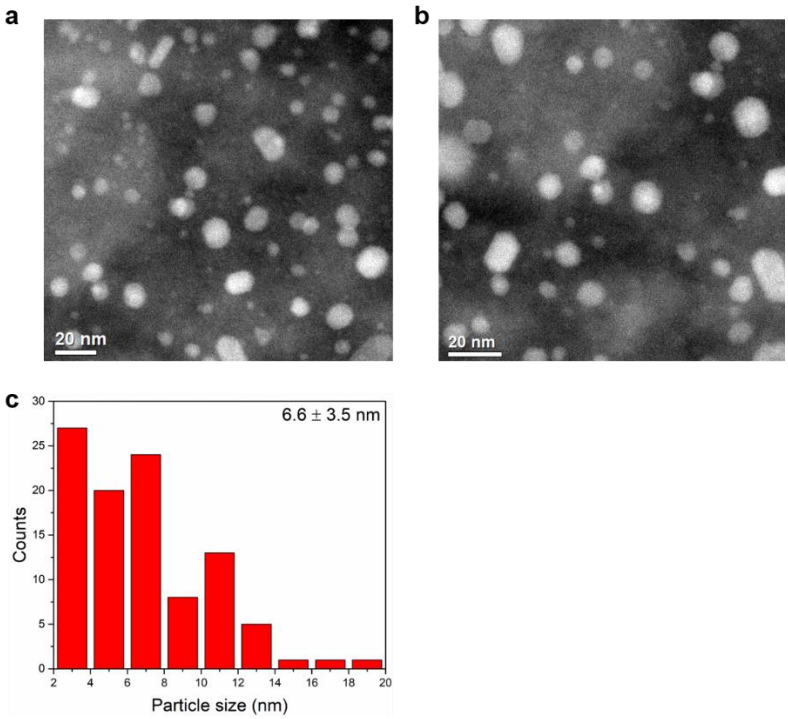

Figure S4.5 Particle size distribution of Pt/$Ti_3C_2T_x$ catalysts reduced at 550°C. The average particle size is 6.6 ± 3.5 nm.

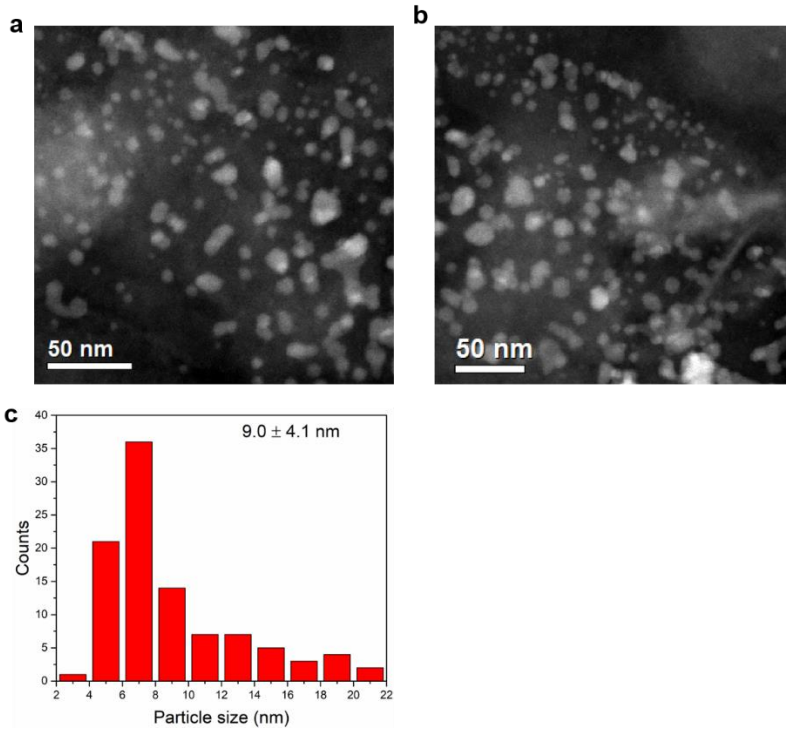

Figure S4.6 Particle size distribution of Pt/$Ti_3C_2T_x$ catalysts reduced at 700°C. The average particle size is 9.0 ± 4.1 nm.

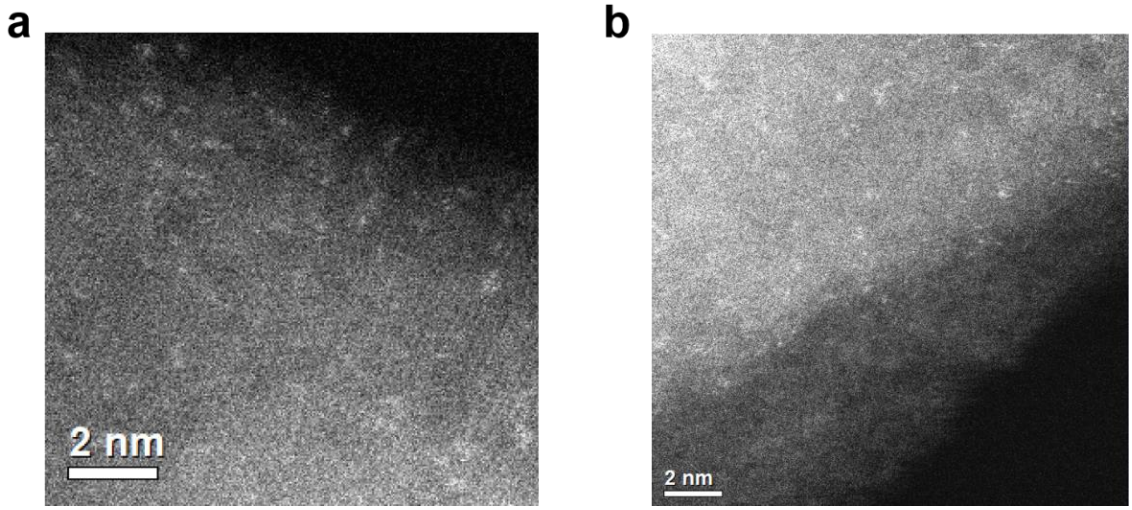

Figure S4.7 STEM image of Pt/$Ti_3C_2T_x$ catalysts reduced at 200°C showing single Pt atoms.

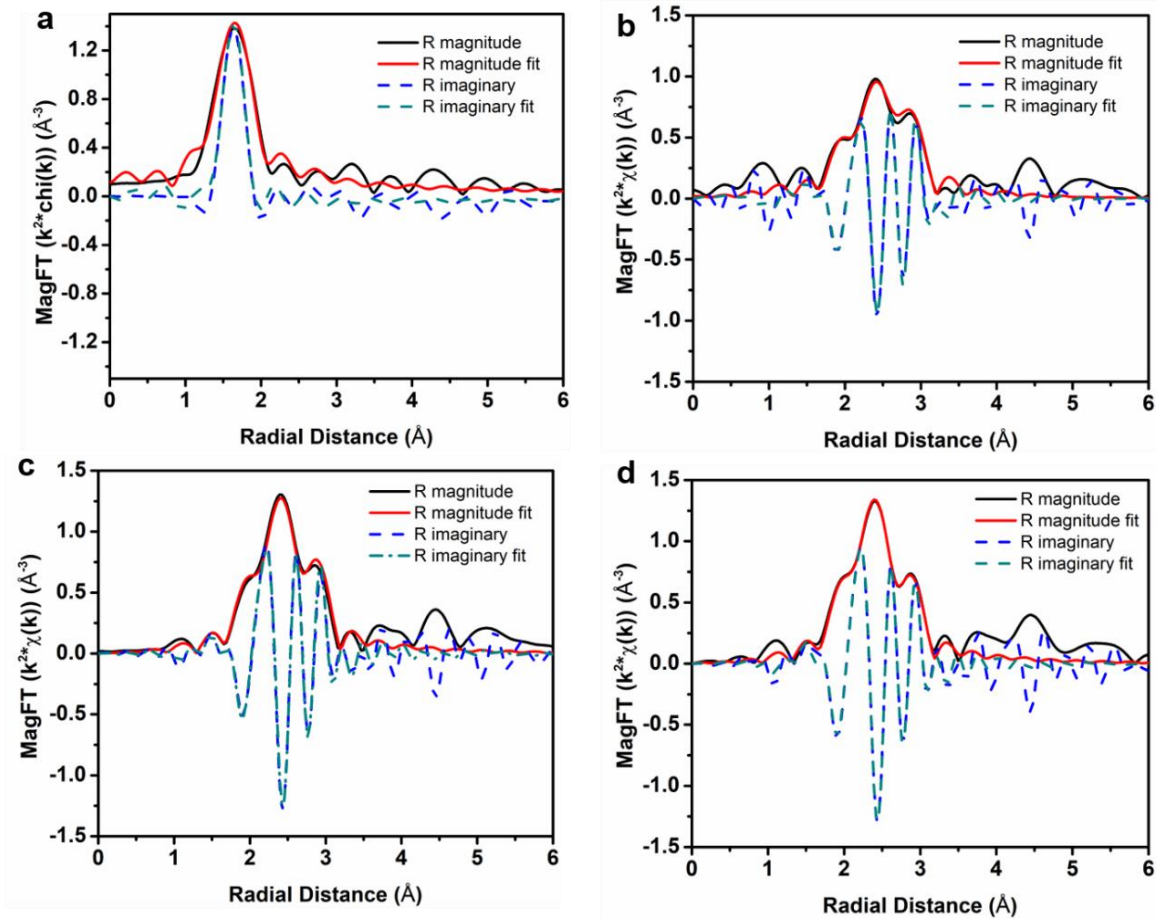

Figure S4.8 The magnitude (solid) and imaginary (dash) part of the Fourier transform of the k^2 weighted EXAFS and corresponding first shell fit for (a) Pt/$Ti_3C_2T_x$-200, (b) Pt/$Ti_3C_2T_x$-400, (c) Pt/$Ti_3C_2T_x$-550, and (d) Pt/$Ti_3C_2T_x$-700.

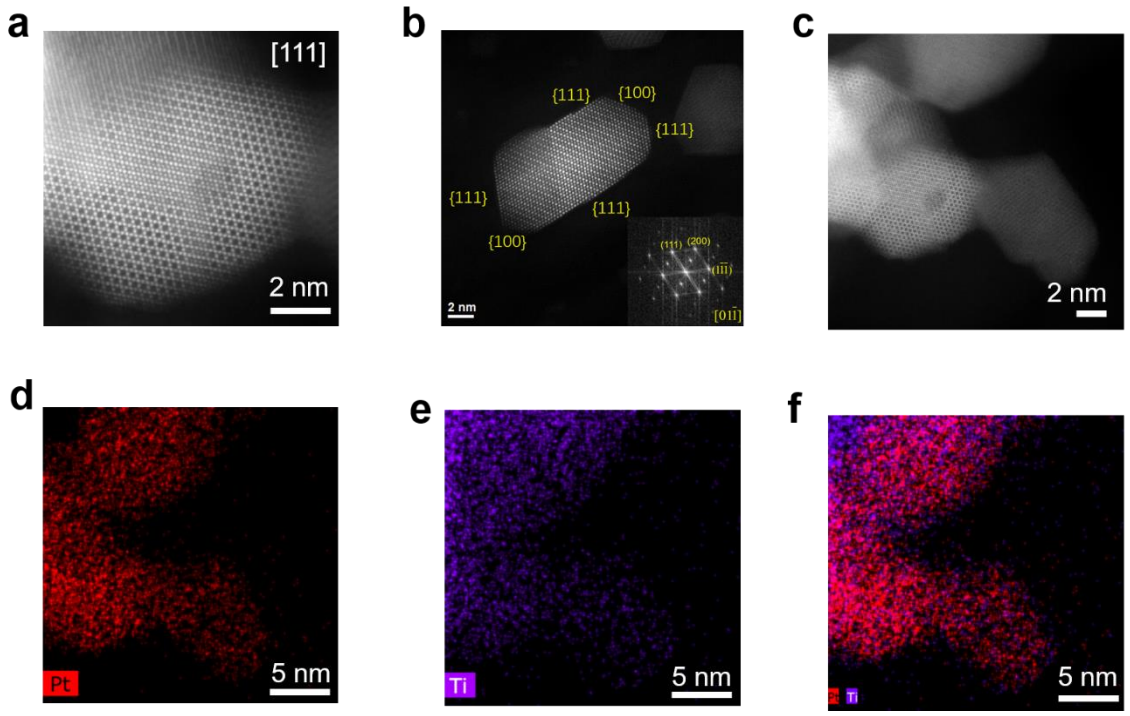

Figure S4.9 (a-c) HAADF image of Pt/$Ti_3C_2T_x$-700. (d-f) EDS elemental mapping of Pt, Ti, and Pt + Ti, respectively.

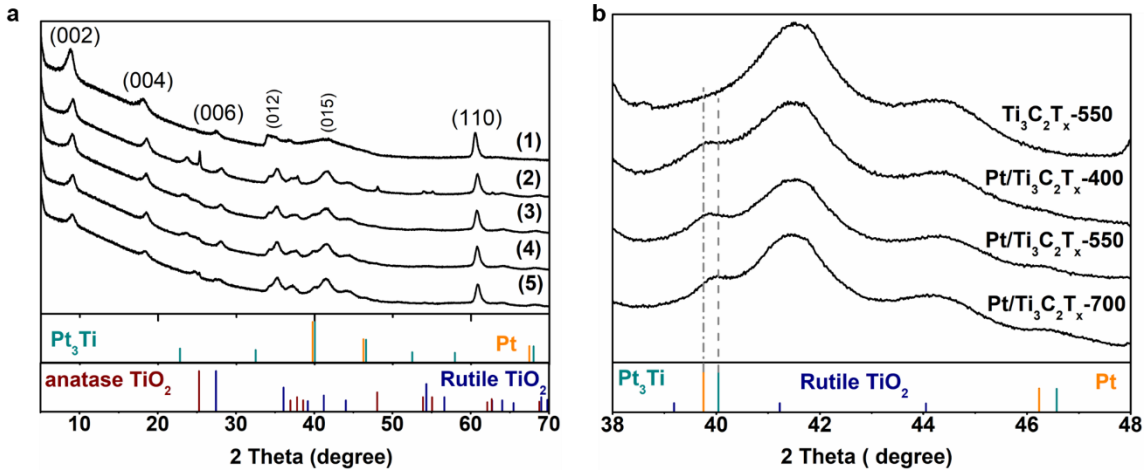

Figure S4.10 (a) XRDs of (1) $Ti_3C_2T_x$ MXene, (2) $Ti_3C_2T_x$ MXene reduced at 550°C, (3) Pt/$Ti_3C_2T_x$-400, (4) Pt/$Ti_3C_2T_x$-550 and (5) Pt/$Ti_3C_2T_x$-700. (b) XRDs in 38º to 48º region.

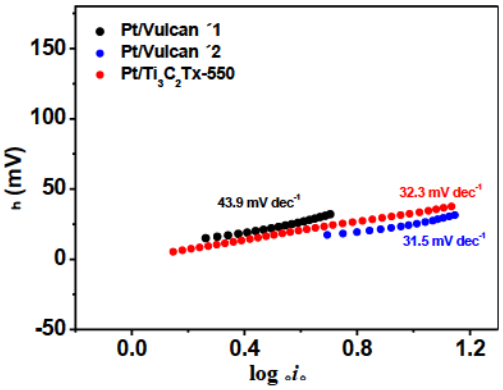

Figure S4.11 Tafel plot of Pt/Vulcan and Pt/$Ti_3C_2T_x$-500. Pt/Vulacan×1 and Pt/$Ti_3C_2T_x$-500 contain the same amount of Pt (21μg). Catalyst loading was doubled for Pt/Vulacan×2, i.e., Pt/Vulacan×2 contains 42 μg Pt.

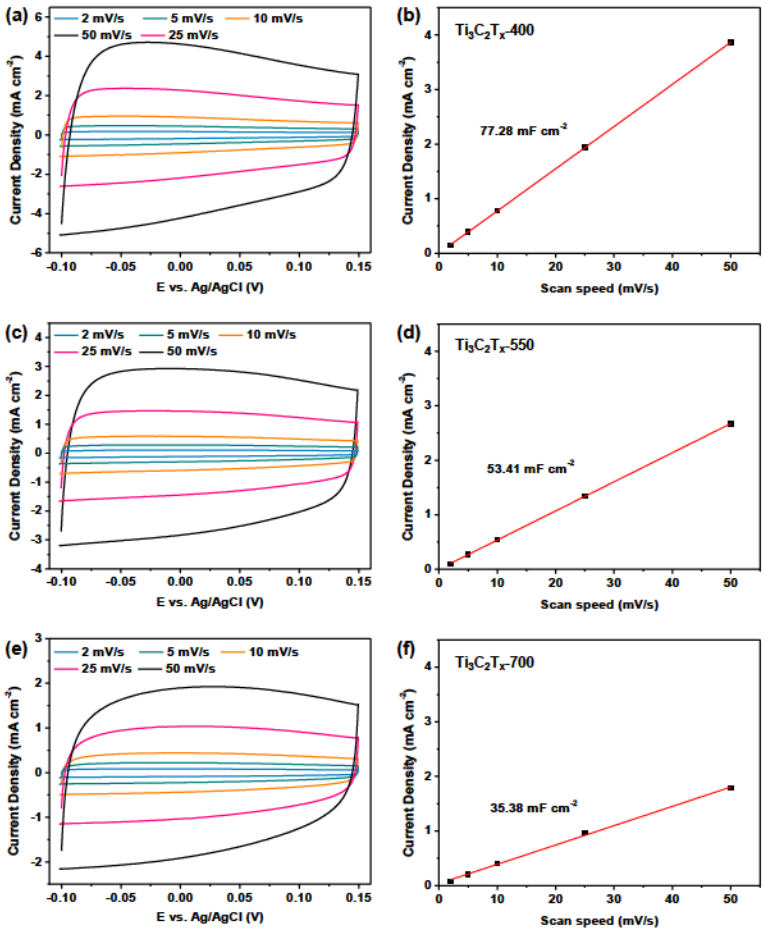

Figure S4.12 CV curves measured from -0.10 V to 0.15 V vs Ag/AgCl at different scan speed, and electrochemical double layer capacitance calculation of bare support (a, b) $Ti_3C_2T_x$-400, (c, d) $Ti_3C_2T_x$-550, and (e, f) $Ti_3C_2T_x$-700. The current density at 0.05 V vs. Ag/AgCl was used for the calculation.

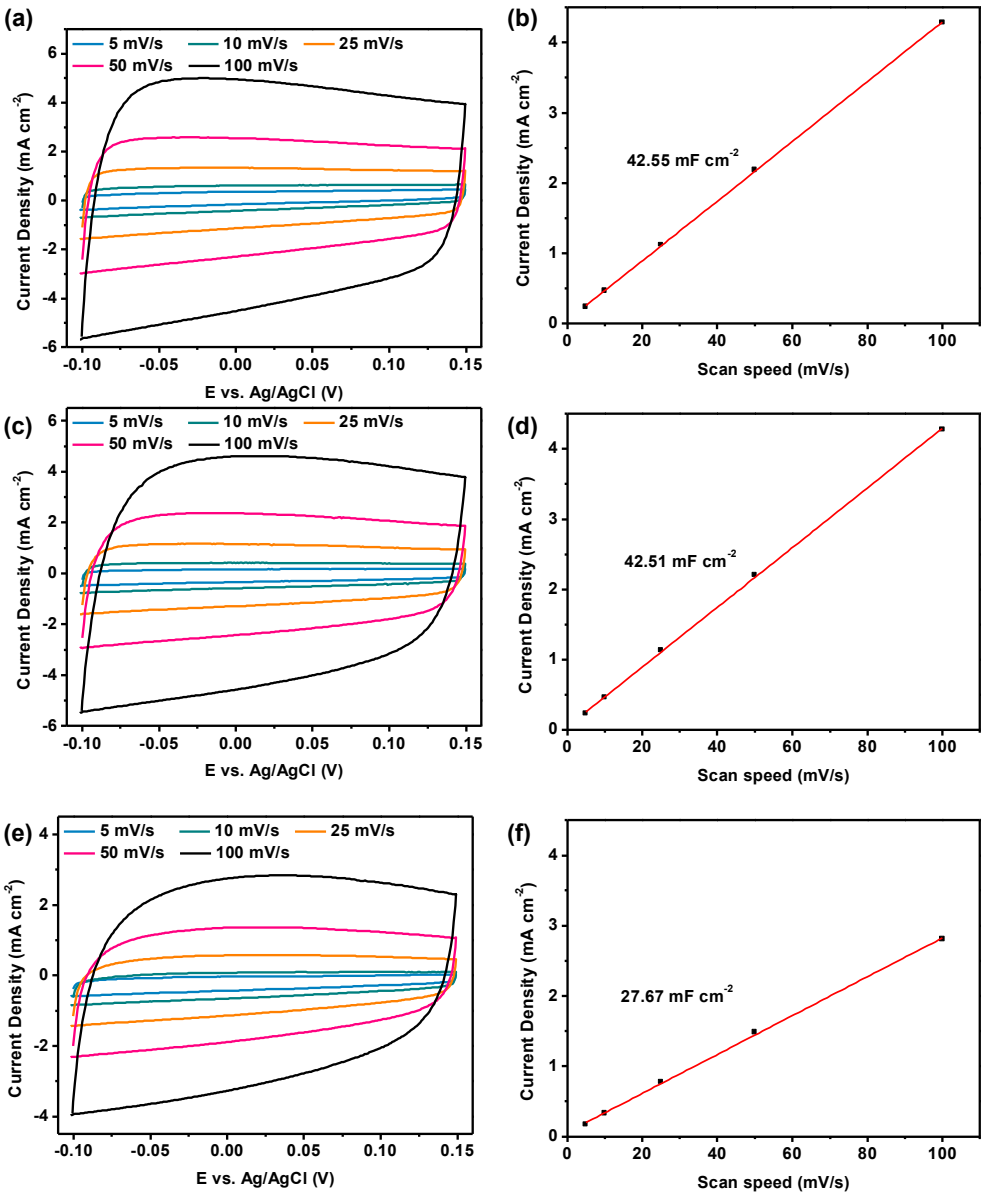

Figure S4.13 CV curves measured from -0.10 V to 0.15 V vs Ag/AgCl at different scan speed, and electrochemical double layer capacitance calculation of bare support (a, b) Pt/$Ti_3C_2T_x$-400, (c, d) Pt/$Ti_3C_2T_x$-550, and (e, f) Pt/$Ti_3C_2T_x$-700. The current density at 0.05 V vs. Ag/AgCl was used for the calculation.

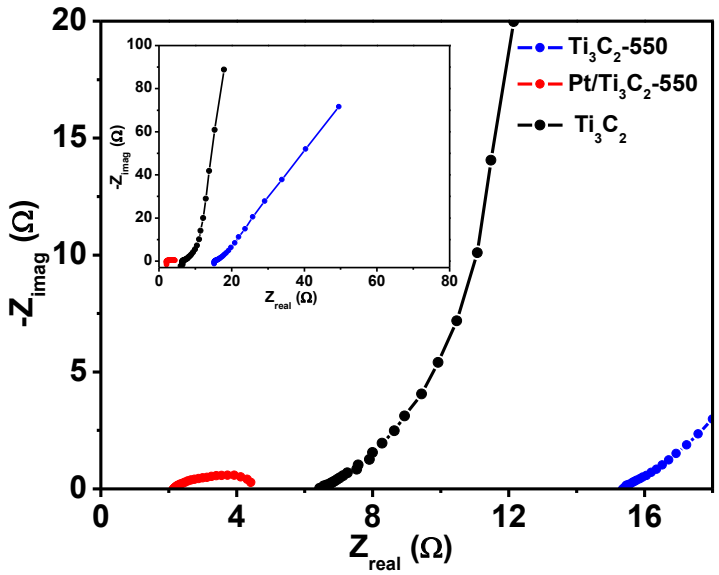

Figure S4.14 Nyquist plot of Pt/$Ti_3C_2T_x$-550, Ti_3C_2 and control samples Ti_3C_2-550 measured at 0 V vs. RHE.

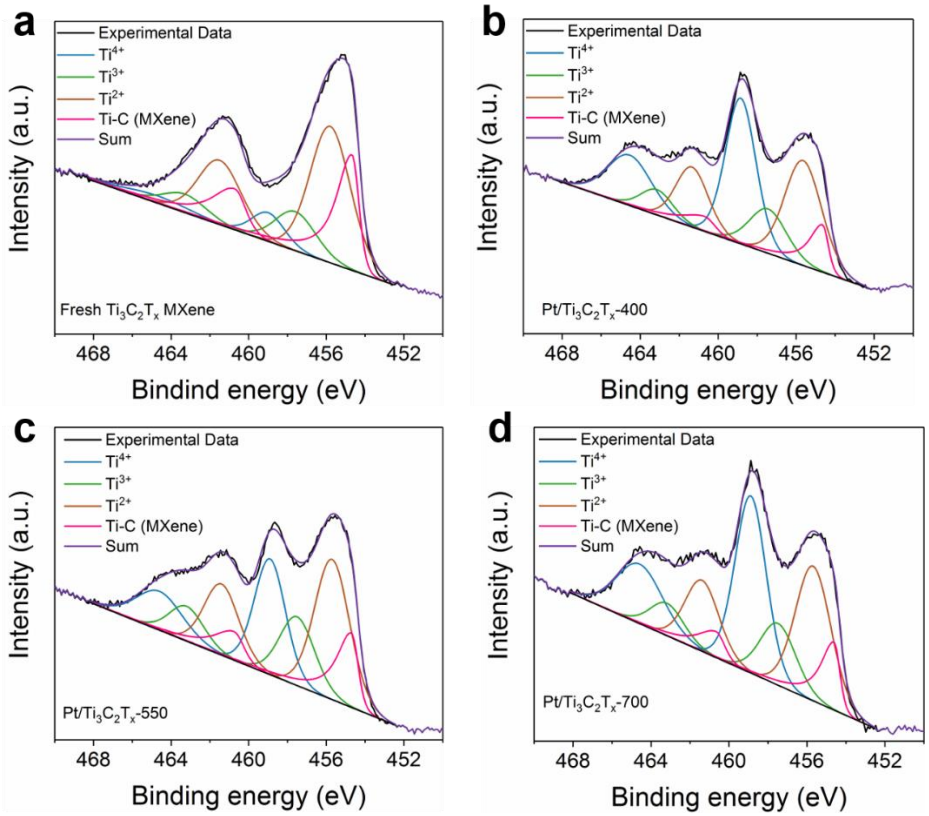

Figure S4.15 (a) High resolution Ti 2*p* XPS spectrum of $Ti_3C_2T_x$, (b) Pt/$Ti_3C_2T_x$-400, (c) Pt/$Ti_3C_2T_x$-550 and (d) Pt/$Ti_3C_2T_x$-700.

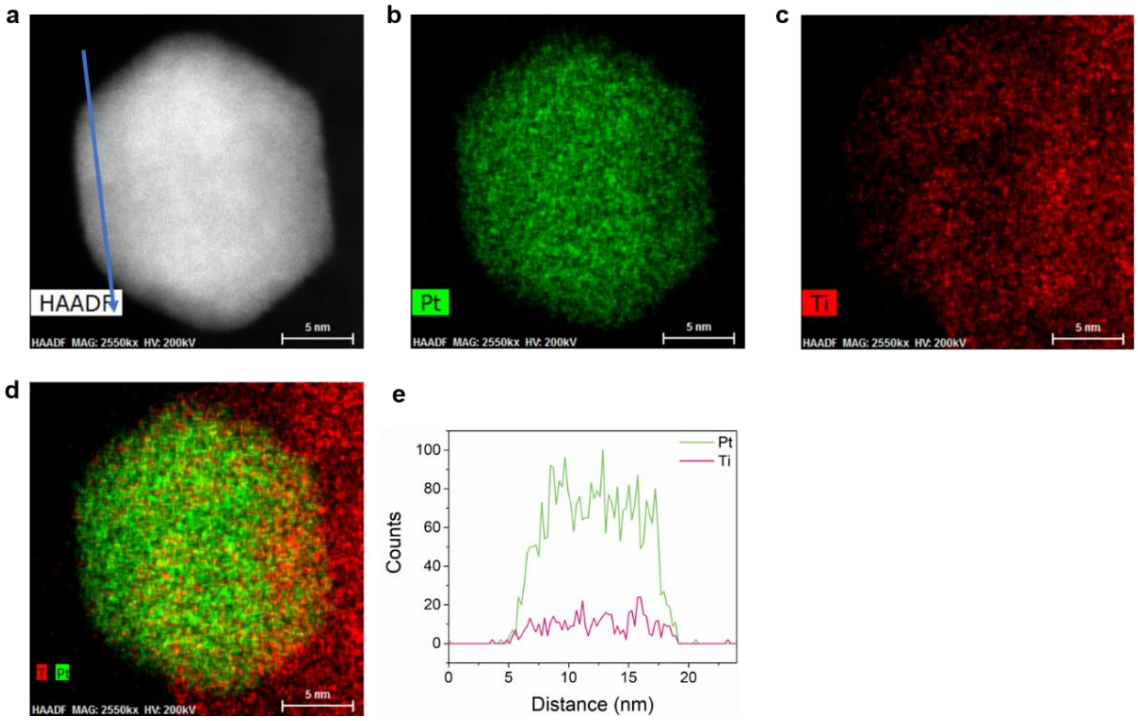

Figure S4.16 (a) HAADF image of used Pt/$Ti_3C_2T_x$ HER catalysts. (b-d) EDS elemental mappings of the used Pt/$Ti_3C_2T_x$ catalysts. (e) EDS line scans for the nanoparticle in (a).

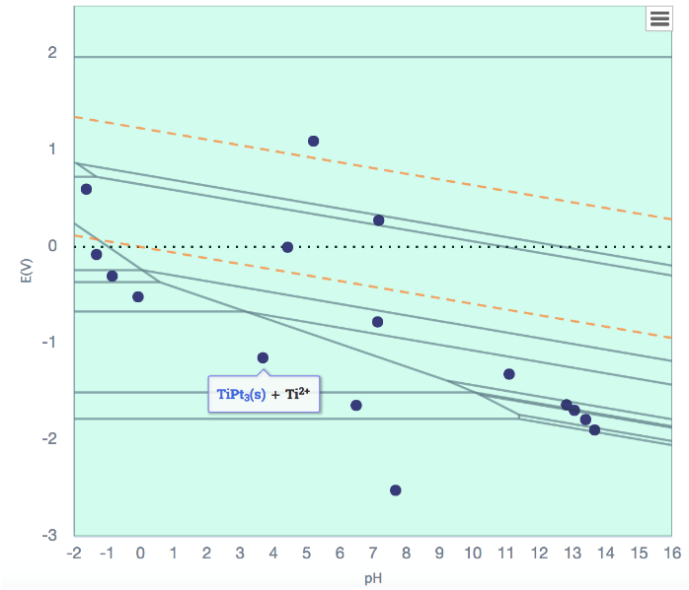

Figure S4.17 Pourbaix diagram of Ti+Pt system as calculated from materialsproject.org.

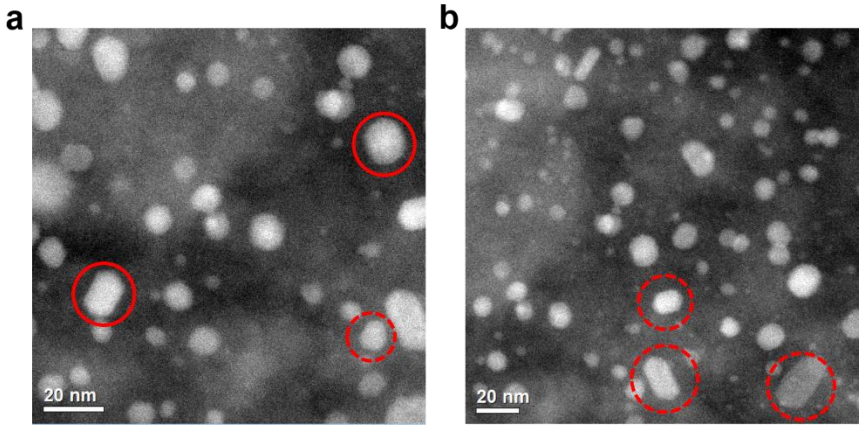

Figure S4.18 STEM images of Pt/$Ti_3C_2T_x$ reduced at 550 ºC showing nanoparticles with cuboctahedral morphology.

Table S4.1 Quantitative information of the XANES data and EXAFS fits

Samples	Edge Energy (KeV)	Scattering Pair	S_0^2[a]	CN[b]	r (Å)[b]	ΔE_0 (eV) [b]	σ^2 (Å^2) [b]
Pt Foil	11.5640	Pt-Pt	0.77	12	2.76	7.7	0.004
2% Pt/SiO_2 550 ºC	11.5640	Pt-Pt	0.77 *	8.6	2.74	7.1	0.006
Pt/$Ti_3C_2T_x$ 200 ºC	11.5653	Pt-N(O)	0.77 *	4.1	2.06	7.7	0.003
Pt/$Ti_3C_2T_x$ 400 ºC	11.5640	Pt-Pt Pt-Ti	0.77 *	8.5 0.3	2.75 2.74	4.6	0.006 0.015
Pt/$Ti_3C_2T_x$ 550 ºC	11.5646	Pt-Pt Pt-Ti	0.77 *	6.6 3.4	2.75 2.75	6.8	0.006 0.015
Pt/$Ti_3C_2T_x$ 700 ºC	11.5648	Pt-Pt Pt-Ti	0.77 *	7.2 4.1	2.75 2.74	5.9	0.006 0.015

[a] The S_0^2 (reduction factor) is fixed at the value obtained by fitting a Pt foil reference.

[b] The average error in CN (coordination number) is 0.5, in r (bond length) is 0.003 Å, in ΔE_0 (energy shift) is 0.5 eV and in σ^2 (Debye-Waller factor) is 0.001 Å^2.

Table S4.2 Summary of HER activity catalyzed by different Pt-Ti/MXene catalysts.

Samples	Pt wt%	Mass of Pt (μg)	η@10mA (mV)	η@40mA (mV)
Pt/Vulcan	20.0	22.0	55.8	159.1
Pt/$Ti_3C_2T_x$ -200	0.89	21.1	270.8	382.5
Pt/$Ti_3C_2T_x$ -550	1.0	21.9	32.7	60.8
Pt/$Ti_3C_2T_x$ -700	1.2	30.7	122.3	270.6
Pt/$Ti_3C_2T_x$ -400	1.0	20.4	73.0	175.8
Ti_3C_2	-	-	576.8	-

Table S4.3 Summary of HER mass activity and specific activity at 50 and 70 mV overpotential.

Samples	Total Pt mass (ug)	Pt dispersion (%) measured at -60 °C	50 mV current (mA)	50 mV Mass activity (mA/ug)	50 mV specific acitvity (mA/ug surface Pt)	70 mV current (mA)	70 mV Mass activity (mA/ug)	70 mV specific acitvity (mA/ug surface Pt)
Pt/$Ti_3C_2T_x$ -550	20.0	7.6	26.10	1.305	17.17	52.6	2.63	34.61
Pt/Vulcan	22.0	22.2	8.73	0.397	1.79	12.97	0.59	2.66
Pt/$Ti_3C_2T_x$ -400	20.4	10.6	5.36	0.263	2.48	9.46	0.46	4.37
Pt/$Ti_3C_2T_x$ -700	30.7	3.2	1.21	0.039	1.23	3.78	0.12	3.85

Table S4.4. Literature summary of HER activity in acidic condition

Catalysts	Overpotential@ 10 mA cm^{-2} (mV)	Real current @10 mA cm^{-2} (mA)	Tafel slope (mV dec^{-1})	Catalyst loading (mg cm^{-2})	Mass activity@ 50 mV (mA/μg)[a]	Reference
Pt/Ti_3C_2-550	32.7	10	32.3	20 μg Pt cm^{-2}	1.31	This work
Pt/DNA	30	0.71	26	15 μg Pt cm^{-2}	1.26	[6]
Pt/MoS_2	50	0.71	40	-	~0.37	[7]
Pt NWs/SL-Ni(OH)2	95 @5 mA cm^{-2}	1.96	-	16 μg Pt cm^{-2}	~0.27	[8]
Ru/GLC	35	0.71	46	400	~0.35	[9]
Ru@CN	22	0.71	30	0.285	~0.39	[10]
NiAu/Au	36	0.71	46	0.204	-	[11]
CoNi@NC	142	1.96	105	0.32	-	[12]
Ag_2S/Ag	199	0.71	102	1.06	0.026@250 mV	[13]
Fe_2P/C	115	-	56	0.72	-	[14]
Rh-MoS_2	50	0.17	24	0.31	~0.93	[15]

[a] Only the mass activity of catalysts containing noble metal was calculated at the fixed overpotential (50 mV vs. RHE). The mass activity was not given in most of the literature and was calculated by dividing the estimated current (or current density) by catalyst mass (or mass loading).

4.10 Supplementary References

[1] a) G. Kresse, J. Furthmüller, *Phys. Rev. B* **1996**, *54*, 11169; b) G. Kresse, J. Hafner, *J. Phys. Condens. Matter* **1994**, *6*, 8245; c) P. E. Blöchl, *Phys. Rev B.* **1994**, *50*, 17953.

[2] J. P. Perdew, K. Burke, M. Ernzerhof, *Phys. Rev. Lett.* **1996**, *77*, 3865.

[3] B. Hammer, L. B. Hansen, J. K. Nørskov, *Phys. Rev. B* **1999**, *59*, 7413.

[4] H. J. Monkhorst, J. D. Pack, *Phys. Rev. B* **1976**, *13*, 5188.

[5] J. K. Nørskov, J. Rossmeisl, A. Logadottir, L. Lindqvist, J. R. Kitchin, T. Bligaard, H. Jonsson, *J. Phys. Chem. B* **2004**, *108*, 17886-17892.

[6] S. Anantharaj, P. E. Karthik, B. Subramanian, S. Kundu, *ACS Catal.* **2016**, *6*, 4660-4672.

[7] X. Huang, Z. Zeng, S. Bao, M. Wang, X. Qi, Z. Fan, H. Zhang, *Nat. Commun.* **2013**, *4*, 1444.

[8] H. Yin, S. Zhao, K. Zhao, A. Muqsit, H. Tang, L. Chang, H. Zhao, Y. Gao, Z. Tang, *Nat. Commun.* **2015**, *6*, 6430.

[9] Z. Chen, J. Lu, Y. Ai, Y. Ji, T. Adschiri, L. Wan, *ACS Appl. Mater. Interfaces* **2016**, *8*, 35132-35137.

[10] J. Mahmood, F. Li, S.-M. Jung, M. S. Okyay, I. Ahmad, S.-J. Kim, N. Park, H. Y. Jeong, J.-B. Baek, *Nat Nanotechnol.* **2017**, *12*, 441.

[11] Y. Shi, J. Wang, C. Wang, T.-T. Zhai, W.-J. Bao, J.-J. Xu, X.-H. Xia, H.-Y. Chen, *J. Am. Chem. Soc* **2015**, *137*, 7365-7370.

[12] J. Deng, P. Ren, D. Deng, X. Bao, *Angew. Chem. Int. Ed.* **2015**, *54*, 2100-2104.

[13] M. Basu, R. Nazir, C. Mahala, P. Fageria, S. Chaudhary, S. Gangopadhyay, S. Pande, *Langmuir* **2017**, *33*, 3178-3186.

[14] X. Zhu, M. Liu, Y. Liu, R. Chen, Z. Nie, J. Li, S. Yao, *J. Mater. Chem. A* **2016**, *4*, 8974-8977.

[15] Y. Cheng, S. Lu, F. Liao, L. Liu, Y. Li, M. Shao, *Adv. Funct. Mater.* **2017**, *27*, 1700359.

CHAPTER 5. GENERAL CONCLUSION

This work studied reactive metal support interactions (RMSI) between Pt and 2D early transition metal carbides (MXenes). Although RMSI has been known in oxide-supported catalysts, supports other than oxides are generally disregarded as candidates for RMSI. This work was a prominent example that broke this discrimination. With the help of advanced characterizations such as in situ X-ray absorption spectroscopy (XAS) and photoelectron spectroscopy (XPS), the formation of Pt-Nb surface alloy formed in the Pt/Nb_2C catalyst at moderate temperature (350 °C) was confirmed. The water-gas shift (WGS) reaction was selected as a model reaction to understand effects of RMSI on adsorbates and metal-support interfaces. Kinetics reveal that the RMSI stabilizes the NPs and creates alloy-MXene interfaces with higher H_2O activation ability compared to a non-reducible support or a bulk niobium carbide. The RMSI found in 2D carbide supported catalysts allows the facile design of bimetallic structures

The following work focused on identifying the nature of active sites formed by the RMSIs effect. By utilizing aberration corrected scanning transmission electron microscopy (STEM) as well as in situ spectroscopies, ordered Pt_3Ti and surface Pt_3Nb intermetallic compound (IMC) NPs were identified in Pt supported by 2D titanium and niobium carbide catalysts, respectively. These catalysts showed superior selectivity (meet industrial standard) for light alkane dehydrogenation, a reaction in renewed interest due to shale gas boom. Experimental results and theoretical calculations revealed that the formation of well-defined IMCs offers electronic perturbation (change in the energy distribution of the 5d unoccupied states), making the catalysts selective for C-H bond activation. Moreover, the application of MXene supported catalysts was also extended to electrochemical hydrogen evolution reaction. Pt/$Ti_3C_2T_x$ outperformed the commercial Pt/Vulcan catalysts.

For the first time, by simply reducing the noble metal precursor with the 2D carbide supports, we are now able to prepare supported IMC NPs catalysts via MSIs. This technology is a promising candidate for rational design of industrial catalysts. The detailed significance of this work includes:

(i) Extended the concept of RMSIs to non-oxide supports. Currently, supports other than oxides are disregarded as candidates for RMSI. Our work shows some examples that RMSI can be achieved at lower temperature in the 2D carbides supported catalysts compared to NPs supported by traditional oxides such as TiO_2.

(ii) Demonstrated that MXenes are promising supports for heterogenous catalysis. Since the discovery of MXene in 2011, the materials have been intensively studied as energy storage devices such as batteries and supercapacitors. Chemistry intuition informs us that MXenes could be promising candidates for catalysis due to their rich surface chemistry as well as thermal stability. This research is pioneer work that exploits MXenes as supports for NP catalysts and demonstrates how the catalytic performance can be tuned through RMSIs.

(iii) Employed MXenes as platforms for preparing intermetallic NP catalysts. This research explores a general phenomenon between MXenes and a noble metal instead of being an interesting example or observation.

(iv) Developed a facile method for rational design of intermetallic NP catalyst. The common strategies for preparing bimetallic catalyst such as reductive deposition precipitation often require organic ligands as stabilizers and high temperature reductions (>600°C). The MXenes supported catalysts pave new avenues for facile synthesis of bimetallic catalysts without those limits.